COPPE
UFRJ

**Instituto Alberto Luiz Coimbra de
Pós-Graduação e Pesquisa de Engenharia**

NUMERICAL EVALUATION OF THE FREE SURFACE EFFECT ON THE HYDRODYNAMICS AND DYNAMICS OF UNDERWATER VEHICLES

Mojtaba Maali Amiri

Tese de Doutorado apresentada ao Programa de Pós-graduação em Engenharia Oceânica, COPPE, da Universidade Federal do Rio de Janeiro, como parte dos requisitos necessários à obtenção do título de Doutor em Engenharia Oceânica.

Orientadores: Sergio Hamilton Sphaier
Paulo de Tarso Themistocles Esperança
Marcelo de Araujo Vitola

Rio de Janeiro
Outubro de 2018

NUMERICAL EVALUATION OF THE FREE SURFACE EFFECT ON THE HYDRODYNAMICS AND DYNAMICS OF UNDERWATER VEHICLES

Mojtaba Maali Amiri

TESE SUBMETIDA AO CORPO DOCENTE DO INSTITUTO ALBERTO LUIZ COIMBRA DE PÓS-GRADUAÇÃO E PESQUISA DE ENGENHARIA (COPPE) DA UNIVERSIDADE FEDERAL DO RIO DE JANEIRO COMO PARTE DOS REQUISITOS NECESSÁRIOS PARA A OBTENÇÃO DO GRAU DE DOUTOR EM CIÊNCIAS EM ENGENHARIA OCEÂNICA.

Examinada por:

_____
Prof. Sergio Hamilton Sphaier, Dr.-Ing.

_____
Dr. Marcelo de Araujo Vitola, D.Sc.
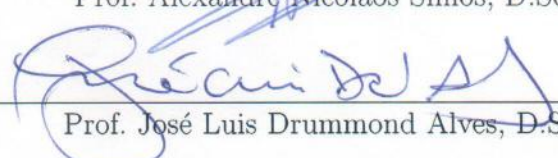
_____
Prof. Carlos Antônio Levi da Conceição, Ph.D.

_____
Prof. Claudio Alexis Rodríguez Castillo, D.Sc.

_____
Prof. Su Jian, D.Sc.

_____
Prof. Alexandre Nicolaos Simos, D.Sc.

_____
Prof. José Luis Drummond Alves, D.Sc.

RIO DE JANEIRO, RJ – BRASIL
OUTUBRO DE 2018

To my family

Acknowledgement

AVALIAÇÃO NUMÉRICA DO EFEITO DA SUPERFÍCIE LIVRE NA HIDRODINÂMICA E DINÂMICA DE VEÍCULOS SUBMARINOS

Mojtaba Maali Amiri

Outubro/2018

Orientadores: Sergio Hamilton Sphaier
                 Paulo de Tarso Themistocles Esperança
                 Marcelo de Araujo Vitola

Programa: Engenharia Oceânica

A presente tese tem como objetivo avaliar o efeito da superfície livre na hidrodinâmica e dinâmica de um veículo submarino (UV) genérico no plano horizontal. Portanto, os testes cativos, incluindo os testes de reboque e de braço rotativo, são realizados num modelo UV usando as simulações numéricas baseadas nas equações de URANS com um modelo de turbulência de Reynolds implementados no código comercial STARCCM+. Estes testes são realizados nas várias profundidades de submersão e faixas apropriadas das velocidades. Para fins de avaliação de manobrabilidade, as forças e os momentos obtidos a partir das simulações dos testes cativos são implementados nas equações de movimento nas várias profundidades. Adicionalmente, as equações analíticas são usadas para calcular as forças e os momentos que surgem das acelerações, impulso e leme, os quais são assumidos constantes em relação à profundidade. Os resultados obtidos mostram que, geralmente, uma diminuição na profundidade provoca um aumento em todas as forças geradas pelas velocidades. Os resultados ainda mostram que aproximar a superfície livre tem um efeito insignificante na força lateral e no momento de yaw ambos gerados pelas regiões de proa e popa. Além disso, observa-se que, com a diminuição da profundidade, a região entre o meio do UV e o ombro de ré é o principal responsável pelo aumento ou diminuição da força lateral e do momento de yaw atuantes sobre o casco do UV. Observa-se também que, com um decréscimo na profundidade, devido a um aumento nas características de amortecimento do UV, a estabilidade dinâmica aumenta consideravelmente, o que leva a uma diminuição da manobrabilidade do UV.

NUMERICAL EVALUATION OF THE FREE SURFACE EFFECT ON THE
HYDRODYNAMICS AND DYNAMICS OF UNDERWATER VEHICLES

Mojtaba Maali Amiri

October/2018

Advisors: Sergio Hamilton Sphaier
          Paulo de Tarso Themistocles Esperança
          Marcelo de Araujo Vitola

Department: Ocean Engineering

The present thesis seeks to evaluate the free surface effect on the hydrodynamics and dynamics of a generic underwater vehicle (UV) in the horizontal plane. Accordingly, the captive tests, including the straight-ahead resistance, drift and rotating arm tests, are performed on the bare hull of a UV model by using numerical simulations based on URANS equations with a Reynolds stress turbulence model implemented in the commercial code STARCCM+. These tests are carried out for various submergence depths and proper ranges of UV velocity components. For the purpose of maneuverability assessment, the forces and moments arising from the velocity components obtained from the simulations of the captive tests are implemented in the equations of motion for various submergence depths. Additionally, analytical equations are used to calculate the forces and moments arising from the UV accelerations, thrust and rudder, which all are assumed to remain constant with respect to submergence depth. The obtained results show that, generally, a decrease in submergence depth causes an increase in all the forces arising from the velocity components. The results further show that approaching the free surface has a negligible effect on the lateral force and yaw moment generated by the bow and stern regions. Moreover, it is seen that with a decrease in submergence depth, the region between the UV midlength and the aft shoulder is mainly responsible for the increase or decrease in the lateral force and yaw moment acting on the UV hull. It is also observed that, with a decrease in submergence depth, due to an increase in the UV damping characteristics, the dynamic stability increases remarkably, which leads to a decrease in the UV maneuverability.

Contents

List of Figures

List of Tables

Nomenclature

Symbol	Dimensionless form	Definition
AR	-	Aspect ratio of the isolated rudder
AR_e	-	Effective aspect ratio of the rudder in the presence of the UV
b_v	-	Rudder span (m)
BS	-	A reference value used in the grid generation process (m)
C_L	-	Lift coefficient of the rudder
C_p	-	Dynamic pressure coefficient
C_u	-	Local Courant number
C_{uL}, C_{uU}	-	User-adjustable parameters
C_θ	-	Angle factor
D	-	UV maximum diameter (m)
D_p	-	Propeller diameter (m)
E	-	Deformation tensor $(\frac{1}{s})$
F_n	$F_n = \frac{U}{\sqrt{gL}}$	Froude number
g	-	Gravity acceleration, $(9.81\frac{m}{s^2})$
h	$h' = \frac{h}{D}$	Submergence depth (m)
H_{max}	$H'_{max} = \frac{H_{max}}{D}$	Maximum wave height (m)
I_z	$I'_z = \frac{I_z}{\frac{1}{2}\rho L^5}$	UV moment of inertia about z_0 axis $(kg.m^2)$
J	$J = \frac{u_A}{nD_p}$	Advance velocity ratio
k	-	Turbulent kinetic energy $(\frac{m^2}{s^2})$
k	-	Von Karman constant
L	$L' = \frac{L}{L}$	UV overall length (m)
l_v	-	$\frac{N'_v}{Y'_v}$ (m)
l_r	-	$\frac{N'_r - m'x'_G}{Y'_r - m'}$ (m)
m	$m' = \frac{m}{\frac{1}{2}\rho L^3}$	UV mass (kg)

Symbol	Non-dimensional form	Description
n	-	Propeller rotation rate $\left(\frac{1}{s}\right)$
N_r	$N'_r = \frac{N_r}{\frac{1}{2}\rho L^4 U}$	First order coefficient utilized in expressing N in terms of r $\left(\frac{kg.m^2}{s}\right)$
$N_{r\|r\|}$	$N'_{r\|r\|} = \frac{N_{r\|r\|}}{\frac{1}{2}\rho L^5}$	Second order coefficient utilized in expressing N in terms of r $(kg.m^2)$
$N_{\dot{r}}$	$N'_{\dot{r}} = \frac{N_{\dot{r}}}{\frac{1}{2}\rho L^5}$	Coefficient utilized in expressing N in terms of $\dot{r}$ $(kg.m^2)$
N_v	$N'_v = \frac{N_v}{\frac{1}{2}\rho L^3 U}$	First order coefficient utilized in expressing N in terms of v $\left(\frac{kg.m}{s}\right)$
$N_{v\|v\|}$	$N'_{v\|v\|} = \frac{N_{v\|v\|}}{\frac{1}{2}\rho L^3}$	Second order coefficient utilized in expressing N in terms of v (kg)
$N_{\dot{v}}$	$N'_{\dot{v}} = \frac{N_{\dot{v}}}{\frac{1}{2}\rho L^4}$	Coefficient utilized in expressing N in terms of $\dot{v}$ $(kg.m)$
$N_{\delta r}$	$N'_{\delta r} = \frac{N_{\delta r}}{\frac{1}{2}\rho L^3}$	First order coefficient utilized in expressing N in terms of δ_r (kg)
$oxyz$	-	Earth-fixed reference frame
P_G	-	Observed order of discretization
R_G	-	Grid convergence ratio
$sx_0 y_0 z_0$	-	Body-fixed reference frame
S_{rud}	-	Rudder surface area (m^2)
t	-	Thrust deduction factor
T	$T' = \frac{T}{\frac{1}{2}\rho L^2 U^2}$	Propeller thrust force (N)
U	-	UV overall speed, $\sqrt{u^2 + v^2}$ $\left(\frac{m}{s}\right)$
u_A	-	Mean flow velocity at the propeller plane $\left(\frac{m}{s}\right)$
U_E	-	Experimental uncertainty
U_G	-	Grid uncertainty
U_{val}	-	Validation uncertainty
u^*	-	Reference velocity $\left(\frac{m}{s}\right)$
u^+	-	Reference velocity coefficient
v_p	-	Velocity component parallel to the wall $\left(\frac{m}{s}\right)$
$v_1 = [u, v, w]$	$v'_1 = \left[u' = \frac{u}{U}, v' = \frac{v}{U}, w' = \frac{w}{U}\right]$	Linear velocity vector in the body-fixed reference frame $\left(\frac{m}{s}\right)$

$v_2 = [p, q, r]$	$v'_2 = \left[p' = \frac{p.L}{U}, q' = \frac{q.L}{U}, r' = \frac{r.L}{U}\right]$	Angular velocity vector in the body-fixed reference frame $\left(\frac{1}{s}\right)$
$\dot{v}_1 = [\dot{u}, \dot{v}, \dot{w}]$	$\dot{v}'_1 = \left[\dot{u}' = \frac{\dot{u}.L}{U^2}, \dot{v}' = \frac{\dot{v}.L}{U^2}, \dot{w}' = \frac{\dot{w}.L}{U^2}\right]$	Linear acceleration vector in the body-fixed reference frame $\left(\frac{m}{s^2}\right)$
$\dot{v}_2 = [\dot{p}, \dot{q}, \dot{r}]$	$\dot{v}'_2 = \left[\dot{p}' = \frac{\dot{p}.L^2}{U^2}, \dot{q}' = \frac{\dot{q}.L^2}{U^2}, \dot{r}' = \frac{\dot{r}.L^2}{U^2}\right]$	Angular acceleration vector in the body-fixed reference frame $\left(\frac{1}{s^2}\right)$
$[X, Y, Z, K, M, N]$	$\left[X' = \frac{X}{\frac{1}{2}\rho U^2 L^2}, Y' = \frac{Y}{\frac{1}{2}\rho U^2 L^2}, Z' = \frac{Z}{\frac{1}{2}\rho U^2 L^2}, K' = \frac{K}{\frac{1}{2}\rho U^2 L^3}, M' = \frac{M}{\frac{1}{2}\rho U^2 L^3}, N' = \frac{N}{\frac{1}{2}\rho U^2 L^3}\right]$	Vector of external forces and moments in the body-fixed reference frame $(N, N.m)$
w	-	Wake fraction
W	-	Tensor of rotation $\left(\frac{1}{s}\right)$
x_B	$x'_B = \frac{x_B}{L}$	x_0 coordinate of the center of buoyancy (m)
x_G	$x'_G = \frac{x_G}{L}$	x_0 coordinate of the center of mass (m)
x_r	$x'_r = \frac{x_r}{L}$	Distance between the rudder's location and the center of the local coordinate system (m)
X_{rr}	$X'_{rr} = \frac{X_{rr}}{\frac{1}{2}\rho L^4}$	Second order coefficient utilized in expressing X in terms of r $(kg.m)$
$X_{\dot{u}}$	$X'_{\dot{u}} = \frac{X_{\dot{u}}}{\frac{1}{2}\rho L^3}$	Coefficient utilized in expressing X in terms of $\dot{u}$ (kg)
$X_{u|u|}$	$X'_{u|u|} = \frac{X_{u|u|}}{\frac{1}{2}\rho L^2}$	Second order coefficient utilized in expressing X in terms of u $\left(\frac{kg}{m}\right)$
X_{vv}	$X'_{vv} = \frac{X_{vv}}{\frac{1}{2}\rho L^2}$	Second order coefficient utilized in expressing X in terms of v $\left(\frac{kg}{m}\right)$
$X_{\delta r \delta r}$	$X'_{\delta r \delta r} = \frac{X_{\delta r \delta r}}{\frac{1}{2}\rho L^2}$	Second order coefficient utilized in expressing X in terms of δ_r $\left(\frac{kg}{m}\right)$
Y^+	-	Dimensionless distance from the wall to the cell centroid

y_G	$y'_G = \frac{y_G}{L}$	y_0 coordinate of the center of mass (m)
Y_r	$Y'_r = \frac{Y_r}{\frac{1}{2}\rho L^3 U}$	First order coefficient utilized in expressing Y in terms of r $(\frac{kg.m}{s})$
$Y_{r\|r\|}$	$Y'_{r\|r\|} = \frac{Y_{r\|r\|}}{\frac{1}{2}\rho L^4}$	Second order coefficient utilized in expressing Y in terms of r $(kg.m)$
$Y_{\dot{r}}$	$Y'_{\dot{r}} = \frac{Y_{\dot{r}}}{\frac{1}{2}\rho L^4}$	Coefficient utilized in expressing Y in terms of $\dot{r}$ $(kg.m)$
Y_v	$Y'_v = \frac{Y_v}{\frac{1}{2}\rho L^2 U}$	First order coefficient utilized in expressing Y in terms of v $(\frac{kg}{s})$
$Y_{v\|v\|}$	$Y'_{v\|v\|} = \frac{Y_{v\|v\|}}{\frac{1}{2}\rho L^2}$	Second order coefficient utilized in expressing Y in terms of v $(\frac{kg}{m})$
$Y_{\dot{v}}$	$Y'_{\dot{v}} = \frac{Y_{\dot{v}}}{\frac{1}{2}\rho L^3}$	Coefficient utilized in expressing Y in terms of $\dot{v}$ (kg)
$Y_{\delta r}$	$Y'_{\delta r} = \frac{Y_{\delta r}}{\frac{1}{2}\rho L^2}$	First order coefficient utilized in expressing Y in terms of δ_r $(\frac{kg}{m})$
z_G	$z'_G = \frac{z_G}{L}$	z_0 coordinate of the center of mass (m)
α	-	Angle of attack
α_i	-	Volume fraction
θ	-	Angle of trim
Θ	-	Angle between the UV's direction of travel and the vector normal to the crest of the wave
β	-	Angle of drift
γ_p	-	Sweep angle at one-fourth of the rudder chord length
γ_τ	-	Turbulent shear stress angle
γ_g	-	Flow gradient angle
δ_r	-	Effective rudder deflection
δ_{r0}	-	User-defined rudder deflection
δ'_r	-	Rudder deflection formed due to r and v
λ	$\lambda' = \frac{\lambda}{L}$	Wavelength (m)
ρ	-	Fluid density $(\frac{kg}{m^3})$
Ω	-	Control volume

S	-	Control surface
τ_w	-	Wall shear stress $(\frac{N}{m^2})$
$\overline{\tau_V}$	-	Tensor of average viscous shear stress $(\frac{N}{m^2})$
$\overline{\tau_R}$	-	Reynolds stress tensor $(\frac{N}{m^2})$
μ	-	Dynamic viscosity $(\frac{kg}{m.s})$
μ_t	-	Isotropic turbulent eddy viscosity $(\frac{kg}{m.s})$
ϑ	-	Kinematic viscosity $(\frac{m^2}{s})$
$\eta_1 = [x, y, z]$	-	Position vector in the earth-fixed reference frame (m)
$\eta_2 = [\phi, \theta, \psi]$	-	Orientation vector in the earth-fixed reference frame
ε	-	Turbulent dissipation rate $(\frac{m^2}{s^3})$
ζ_C	-	Normalized volume fraction in cell center
ζ_f	-	Normalized volume fraction in cell face
Γ	-	diffusivity
ϕ	-	Scalar quantity

Abbreviation	Definition
AMG	Algebraic multigrid
AUV	Autonomous underwater vehicle
HRIC	High resolution interface capturing
RST	Reynolds stress turbulence
SC	Stability criterion
SIMPLE	Semi-implicit method for pressure linked equations
URANS	Unsteady Reynolds-averaged Navier-Stokes
UV	Underwater vehicle
VOF	Volume of fluid

Chapter 1

Introduction

1.1 General problem of operations of underwater vehicles in littoral and near surface environments

Menuvering simulations of underwater vehicles (UVs) in six degrees of freedom are usually performed by using the standard equations of motion proposed by GERTLER e HAGEN [1]. In this mathematical model, which is considered as the first official dynamic model to perform the maneuverability tests of the UVs, the hydrodynamic forces and moments acting on the UV hull constitute the heart of the model. These forces and moments are classified into two general categories: forces and moments arising from the UV velocities and forces and moments generated by the UV accelerations [1]. In this regard, relevant hydrodynamic captive tests are performed to obtain these hydrodynamic forces and moments in terms of the UV velocity and acceleration components [1–3]. Additionally, this mathematical model is primarily developed under the key assumption that the UVs operate in an infinite domain far from the free surface and the seabed.

To improve the maneuverability predictions of the UVs, the model proposed by GERTLER e HAGEN [1] has been followed by a series of modifications to account for several effects, such as the effect of the interaction between the sail trailing vortex and the hull [4], the effect of the slipstream of propeller on the control surfaces [5] and recently the effect of the presence of the calm water free surface [6], which all are neglected in the original model.

In this respect, due to a significant increase in the strategic requirement for UVs to operate in the littoral and near surface environments, the evaluation of the free surface effect on the hydrodynamics and dynamics of the shallowly submerged UVs has stimulated extensive studies in hydrodynamics [6–19]. The need to operate in

the littoral and near surface environments increases even more for autonomous underwater vehicles (AUVs) as they have increasingly found many ocean applications such as ocean surveillance and measurements, exploration and exploitation of sea minerals, environmental monitoring and protection and sea exploration of hydrocarbons [10, 13].

An immediate consequence of a UV traversing close to the calm water free surface is the creation of surface gravity waves that are stationary with respect to the body. The generation of this gravity wave system is attributed to the interaction between the dynamic pressure distribution around the UV hull and the nearby non-rigid free surface. This wave system is composed of several wave systems created at points along the body and is a function of several factors, such as the UV overall length, body form and advance velocity [20]. In this regard, Figure 1.1 shows the wave system generated by a generic axisymmetric UV hull traveling along a straight path with a constant advance velocity corresponding to a Froude number equal to $F_n = 0.512$ at a submergence depth of $h = 1.1D$ (D: UV maximum diameter) in a deep-water scenario. As can be seen in this figure, for a UV traveling along a straight path with a constant advance velocity beneath the free surface in a deep-water scenario the generated wave system has a form similar to the classical Kelvin wave pattern.
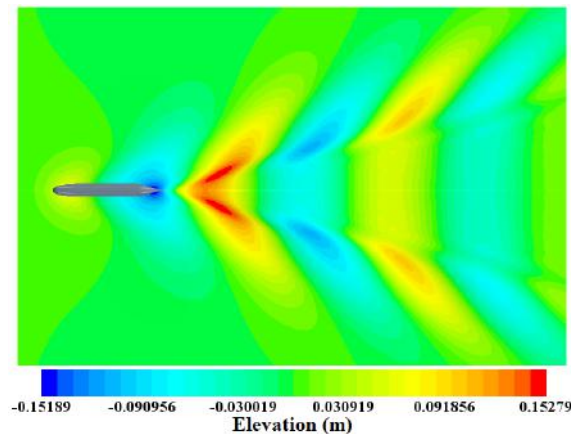
Figure 1.1: Wave system generated by a generic axisymmetric UV hull traveling along a straight path with a constant advance velocity corresponding to a Froude number equal to $F_n = 0.512$ at a submergence depth of $h = 1.1D$ (D: UV maximum diameter) in a deep-water scenario (This figure was generated from the simulations conducted in this work)

As is well known from NEWMAN [21], the energy required for the creation of this surface wave system leads to an increase in the hydrodynamic forces generated by the velocity components on a shallowly submerged UV. Likewise, as shown by MAALI AMIRI *et al.* [19], the increase in the forces arising from the velocity components with a decrease in submergence depth can also be explained through the

effect of the free surface deformations on the dynamic pressure distribution along the length of the UV hull. In this regard, as demonstrated by MAALI AMIRI *et al.* [19], the crests and troughs of the self-induced wave system of a shallowly submerged UV modify the dynamic pressure distribution around the UV hull by creating local regions of high and low dynamic pressure, respectively, along the body length. In this regard, Figure 1.2 shows the dynamic pressure distribution around a generic ax-isymmetric UV hull traveling along a straight path with a constant advance velocity corresponding to a Froude number equal to $F_n = 0.294$ over two different submer-gence depths $h = 1.1D$ (shallowly submerged) and $h = \infty$ (totally submerged) (D: UV maximum diameter). As can be inferred from this figure, the crests and troughs of the generated wave system through creating local regions of high and low dy-namic pressure along the length of the UV introduce modification into the dynamic pressure distribution around the UV hull.

(a) $h = \infty$ (totally submerged)

(b) $h = 1.1D$ (shallowly submerged)
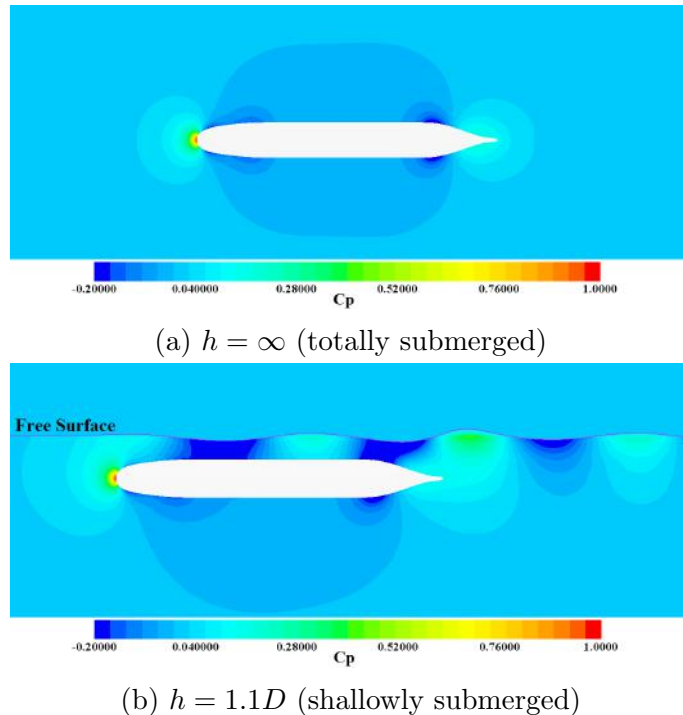
Figure 1.2: Dynamic pressure distribution around a generic axisymmetric UV hull traveling along a straight path with a constant advance velocity corresponding to a Froude number equal to $F_n = 0.294$ over two different submergence depths $h = 1.1D$ (shallowly submerged) and $h = \infty$ (totally submerged) (D: UV maximum diameter) (This figure was generated from the simulations conducted in this work)

Therefore, it can be inferred that a crucial effect of the wave system generated by a shallowly submerged UV is the modification that it introduces into the dynamic pressure distribution around the submerged body. The degree of modification intro-duced into the dynamic pressure distribution around the UV hull by the free surface deformations depends on submergence depth. The less the submergence depth the

more will be the free surface deformations, which consequently increases the free surface effect on the dynamic pressure distribution, MAALI AMIRI *et al.* [19].

Thus, from a theoretical point of view, all of the external forces and moments acting on a UV traveling beneath the free surface are subject to change as a result of approaching the free surface. Furthermore, as shown in Figure 1.2, the modification of the dynamic pressure distribution across the depth of the UV hull gives rise to the generation of the forces and moments in the vertical plane [6, 7, 10–19].

1.1.1 Scope of the present thesis

As can be inferred from the previous section, the calm water free surface effect on a shallowly submerged UV hydrodynamics, maneuverability and operations can be significant. Consequently, a well-founded understanding of the hydrodynamics and dynamics of a shallowly submerged UV traveling in a close proximity to the free surface is required to enable the prediction of the UV maneuverability with the presence of the free surface. A good knowledge of the free surface effect on the maneuverability is extremely useful especially in case of the AUVs in which this knowledge can be effectively employed to fine-tune the motion controllers before missions in littoral and near surface environments.

In the previous studies, the evaluation of the free surface effect on the dynamics and hydrodynamics of a UV traveling close to the free surface has been restricted mainly to the interaction between a UV traveling along a straight path with a constant advance velocity and the free surface with little attention paid to the hydrodynamics and dynamics of a shallowly submerged UV in other degrees of freedom, especially in the horizontal plane [6–19]. Additionally, very little attempt has been made toward the maneuverability evaluation of the UVs with the presence of the free surface.

Accordingly, the present thesis seeks to evaluate the free surface effect on the hydrodynamics and dynamics of a shallowly submerged generic UV traveling close to the free surface in the horizontal plane. In other words, this study investigates the horizontal planar motion of a shallowly submerged UV traveling in a close proximity to the free surface.

However, for the sake of simplicity, in the present thesis, the free surface effect is merely investigated on the hydrodynamic forces and moments produced by the UV velocity components. Accordingly, the hydrodynamic captive tests, including the straight-ahead resistance tests, drift tests and rotating arm tests, are performed over various submergence depths and proper ranges of axial, lateral and angular yaw velocity components.

The hydrodynamic captive tests are usually performed by model experiments in a

towing tank. Nevertheless, a towing carriage equipped with the essential mechanism to conduct such experiments along with proper transducers to measure the global variables can be prohibitively expensive. Aside from the expenses, the main difficulty is encountered in case of a UV traveling close to the free surface. In this respect, the utilization of the support to suspend the model to the towing carriage during the experiments, besides from affecting the pressure distribution around the body, causes the generation of a wave system that interferes with the UV wave system and may introduce additional modifications into the local and global variables acting on the UV hull [22]. Furthermore, to investigate more closely the true role of the free surface in the hydrodynamics and dynamics of a shallowly submerged UV, the measurement of the local variables such as the local dynamic pressure and skin friction along with the fluid flow characteristics are necessary, which requires a new series of experiments to be conducted in wind tunnels or water tunnels, using hot-film sensors, PIV, smoke flow visualizations and pressure tabs [23–25].

Hence, in the present research to avoid high costs of model experiment and the intrusive nature of experimental measurements, a numerical method based on unsteady Reynolds-averaged Navier-Stokes (URANS) equations coupled with a turbulence model is used to perform the captive tests over various submergence depths and proper ranges of UV axial, lateral and angular yaw velocity components. Regarding the detailed information of the local and global variables that the numerical simulations provide, which indeed is difficult to obtain from experiment, the usual CPU time requirement in numerical simulations appears reasonable. For instance, in this study, a desktop PC, which has a 64 bit Intel Processor i7-3770@ 3.40 GHz with 16 GB of RAM, is used and each simulation takes a maximum physical time about 70 h to complete.

1.1.2   Literature review

The literature review of the works performed to evaluate the hydrodynamics and dynamics of the shallowly submerged UVs traveling close to the free surface presented in this section is divided into three main categories: studies conducted to evaluate the free surface effect on the hydrodynamics of axisymmetric UVs moving with a constant advance velocity beneath the free surface at zero incidence with respect to the incoming flow, studies conducted to evaluate the free surface effect on the hydrodynamics of UVs moving with a constant advance velocity beneath the free surface at nonzero incidence and studies conducted to evaluate the maneuverability of the shallowly submerged UVs with the presence of the free surface.

Studies on the shallowly submerged UVs at zero incidence

The free surface effect on the hydrodynamics of the shallowly submerged UVs moving with a constant advance velocity at zero incidence beneath the free suface has long been the subject of numerous studies. The earlier studies on this subject have been conducted by using the solvers based on potential flow theories, such as the ones conducted by HAVELOCK [26], HAVELOCK [27], HAVELOCK [28], WIGLEY [29], DOCTORS e BECK [30] and CROOK [31]. In this regard, Havelock calculates the resistance component due to the generated-wave system (wave-making resistance component) of a shallowly submerged sphere [26], oblate and prolate spheroid [27] and ellipsoid [28] and demonstrates that this component has an oscillatory behavior with respect to Froude number and reduces exponentially with an increase in submergence depth. In this regard, based on NEWMAN [21], the advent of the wave-making resistance component can be attributed to the energy required for the generation of the surface wave system as the submerged body approaches the free surface. Additionally, it is further shown by WIGLEY [29], DOCTORS e BECK [30] and CROOK [31] that a slender axisymmetric body traveling along a straight path with a constant advance velocity at zero incidence close to the free surface, besides the wave-making resistance component, experiences a vertical lift force and pitch moment, which all vary in an oscillatory manner with respect to Froude number.

The potential solvers have also been used recently in several studies, such as BELIBASSAKIS *et al.* [32], GOURLAY e DAWSON [33] and ARZHANNIKOV e KOTELNIKOV [34] to evaluate the free surface effect on the hydrodynamics of the shallowly submerged axisymmetric UVs traveling with a constant advance velocity at zero incidence along a straight path beneath the free surface. The obtained results from these studies show the same trends for the wave-making resistance component, lift force and pitch moment as those obtained by HAVELOCK [26], HAVELOCK [27], HAVELOCK [28], WIGLEY [29], DOCTORS e BECK [30] and CROOK [31].

Additionally, DAWSON [10] conducted an experimental investigation and numerical examination (based on potential flow) into the influence of submergence depth, Froude number and length-to-diameter ratio on the interaction between an axisymmetric generic UV and the free surface. The results show that the resistance force, lift force and pitch moment all vary periodically with respect to Froude number and are directly influenced by the wavelength of the free surface wave field generated by the submerged body. It is further demonstrated that the free surface effect is negligible beyond the depth to diameter ratio of three and completely disappears at depth to diameter ratios larger than five.

Recently, the rapid advance in the computers enables the utilization of more sophisticated solvers that account for the viscosity effects in the evaluation of the

free surface effect on the hydrodynamics of a shallowly submerged axisymmetric body traveling at a constant advance velocity at zero incidence close to the free surface. For instance, WILSON-HAFFENDEN *et al.* [35] MANSOORZADEH e JAVANMARD [12], NEMATOLLAHI *et al.* [13], SALARI e RAVA [14], SHARIATI e MOUSAVIZADEGAN [18] and MAALI AMIRI *et al.* [19] evaluate the free surface effect on the hydrodynamics of shallowly submerged UVs over various submergence depths and Froude numbers by using a solver based on URANS equations coupled with a turbulence model.

In this regard, WILSON-HAFFENDEN *et al.* [35] uses numerical simulations based on URANS equations with $k - \omega$ SST turbulence model together with experimental methods to evaluate the free surface effect on the behavior of the resistance force exerted on a generic axisymmetric UV hull over various submergence depths and Froude numbers. It is shown that the URANS solvers coupled with turbulence models are able to predict the hydrodynamic behavior of a shallowly submerged UV to an acceptable level. It is further demonstrated that at small Froude numbers, the free surface effect on the resistance force is negligible beyond the depth to diameter ratio of two.

Additionally, MANSOORZADEH e JAVANMARD [12] by using URANS equations coupled with $k - \varepsilon$ turbulence model along with experimental approaches show that both the drag and lift coefficients of a shallowly submerged UV are functions of both Froude number and submergence depth. Also, NEMATOLLAHI *et al.* [13] by using the same method as that used by MANSOORZADEH e JAVANMARD [12] demonstrate that the reduction in submergence depth of an axisymmetric UV results in an increase in drag coefficient, and additionally the influence of the free surface at each submergence depth is intensified with respect to Reynolds number. Furthermore, SALARI e RAVA [14] by using URANS equations with $k - \omega$ SST turbulence model, the same as the other researchers, demonstrate that a UV close to the free surface experiences a larger drag force along with a lift force and a pitch moment.

Moreover, SHARIATI e MOUSAVIZADEGAN [18] investigate the effect of different appendages on the hydrodynamics of a shallowly submerged generic UV traveling close to the free surface. This investigation is carried out by performing numerical simulations based on URANS equations coupled with $k - \varepsilon$ turbulence model over various submergence depths and Froude numbers. SHARIATI e MOUSAVIZADE-GAN [18] show that the presence of the appendages has negligible effect on the UV-generated wave system and consequently contributes slightly to the wave-making resistance component. It is further demonstrated that the presence of appendages causes an average increase of about 16% in the total resistance force, which is attributed to the viscosity effects and the hull-appendages interaction.

Finally, MAALI AMIRI *et al.* [19] employ a solver based on URANS equations coupled with a Reynolds stress turbulence model to determine that, in case of the shallowly submerged axisymmetric UVs, whether the interaction between the bow and aft shoulder waves or the interaction between the bow and stern waves has the dominant effect on the hydrodynamic behavior of a shallowly submerged UV. The analysis of the obtained results demonstrates that the interaction between the bow and aft shoulder waves has a dominant effect on the behavior of the resistance force, lift force and pitch moment. This is due mainly to the closer proximity of the aft shoulder to the free surface, which consequently contributes more to the UV-generated wave system, compared to the stern.

Studies on the shallowly submerged UVs at nonzero incidence

As can be expected, because of the limitations of the potential solvers, they are likely unable to evaluate accurately the interaction between the free surface and a yawed/trimmed UV, due to the vortical structure formed on the leeward side of the body at incidence. Therefore, their use to evaluate the hydrodynamics of shallowly submerged UVs moving with a constant advance velocity at nonzero incidence beneath the free suface is limited to only one study, which is carried out by GRIFFIN [7]. In this study, a hybrid method (a combination of URANS coupled with the isotropic two-equation turbulence model $k - \omega$ and potential flow solver) is used to predict the hydrodynamics of two generic axisymmetric UV geometries operating near the free surface. The URANS code calculates the flow field immediately surrounding the bodies and the potential solver calculates the fluid flow in the far field, including the free surface. In this research, the forces and moment in the vertical plane are calculated at trim angles in a range of $-2° \leqslant \theta \leqslant 2°$ over various submergence depths and Froude numbers. It is shown that the forces and moments vary in a nonlinear fashion with a change in submergence depth and Froude number.

Moreover, BROGLIA *et al.* [15] use URANS equations coupled with the one-equation turbulence model of Spalart and Allmaras to investigate the interaction between the free surface and a fully-appended generic UV. The simulations are performed at one nominal Froude number for drift and trim angles in a range of $0° \leqslant \beta \leqslant 4°$ and $-5° \leqslant \theta \leqslant 5°$, respectively, over various submergence depths. The obtained results show that although the presence of the free surface causes a significant increase in the forces and moment in the vertical plane, its presence appears to have a negligible influence on the lateral force and moment in the horizontal plane.

Finally, JAGADEESH e MURALI [11] investigate the free surface effect on the drag, lift and pitch moment coefficients of an axisymmetric UV at different Froude numbers for trim angles in a range of $-15° \leqslant \theta \leqslant 15°$, using numerical simulations based on URANS equations coupled with various isotropic two-equation based tur-

bulence models. It is shown that a reduction in submergence depth results in an increase in the wave-making resistance and thus increases the total drag, lift and pitch moment coefficients. It is further demonstrated that the free surface effect is negligible beyond the depth to diameter ratio of two.

Based on the studies presented above, it can be concluded that, contrary to the UVs at zero incidence, few investigations have been carried out to evaluate the free surface effect on the hydrodynamics of a shallowly submerged UV at nonzero incidence, especially in the horizontal plane. Additionally, there is little research in the literature that addresses the free surface effect on the hydrodynamics of a shallowly submerged UV undergoing a rotational motion close to the free surface. Accordingly, all these topics are covered in the present thesis.

Studies on the maneuverability of the shallowly submerged UVs

Very little attempt has been made toward the maneuverability evaluation of the UVs with the presence of the free surface.

In this regard, the study conducted by SAOUT e ANANTHAKRISHNAN [8] is among the few works to evaluate the dynamic stability of a UV traveling in the horizontal plane both at infinite depth and close to the free surface at a submergence depth equal to $h = 1.5D$ (D: UV maximum diameter). In this study, the sway and yaw hydrodynamic coefficients arising from the velocity and acceleration components are calculated by conducting the corresponding planar motion mechanism (PMM) tests using a potential solver. Thus, the viscosity effects are neglected. The results indicate that the presence of the free surface increases the dynamic stability of UVs in the horizontal plane due to an increase in the forces and moments generated by the velocity components.

Moreover, CARRICA et al. [16] perform the free running self-propulsion experiments and simulations of a generic UV operating over various submergence depths. The simulations are carried out by using URANS equations coupled with $k - \varepsilon$ and $k - \omega$ turbulence models. The obtained results show that CFD is generally able to predict the behavior of a UV traversing beneath the free surface. Additionally, the numerical and experimental results of the free running self-propulsion tests near the free surface demonstrate the presence of a strong upward lift force acting on the UV aft part, which produces a bow-down moment over the hull.

Additionally, DUBBIOSO et al. [17] perform the free-running turning maneuvers of a generic UV in the horizontal plane by using URANS equations with one-equation turbulence model of Spalart and Allmaras both at infinite depth and close to the free surface. The simulations are performed at one nominal Froude number and submergence depths of $h = \infty, 1.75D$ (D:UV maximum diameter) for various rudder deflections. The obtained results demonstrate that, for the depths considered, the

presence of the free surface has negligible effect on the turning maneuver of a UV.

Finally, POLIS *et al.* [6] make an initial attempt to add some new terms to the equations of motion of UVs in the vertical plane to account for the free surface effects during the maneuvering simulations. In this regard, after calculation of the resistance force, lift force, and pitch moment acting on a generic UV at zero incidence over various submergence depths and Froude numbers by using numerical simulations based on URANS with $k - \omega$ SST turbulence model, POLIS *et al.* [6] propose a nonlinear function to represent these forces and moment in the maneuvering equations. This nonlinear function, which is defined over small ranges of Froude numbers, uses a cubic polynomial fit to capture the variations with respect to Froude number together with an exponential fit to capture the variations with respect to submergence depth.

However, POLIS *et al.* [6] present no results related to the maneuvering simulations using this new approach. Additionally, as the resistance force, lift force, and pitch moment acting on a shallowly submerged UV at zero incidence have an oscillatory behavior with respect to Froude number (as opposed to the resistance force acting on the totally submerged UV at zero incidence, which has a quadratic behavior with respect to Froude number,) and undergo an exponential reduction with an increase in submergence depth, the method proposed by POLIS *et al.* [6] is not practical. Moreover, using this approach increases notably the regression problem with considerable identification effort, which increases even the possibility of occurrence of error in the parameter identification process. Indeed, the forces and moments arising from the axial velocity acting on a shallowly submerged UV can be suitably stored in a tabular form over various submergence depths, and then a proper interpolation method can be used to express these terms in the maneuvering equations, SUTULO e GUEDES SOARES [36].

It is clear from the literature presented above that very little attempt has been made toward the dynamic stability and maneuverability evaluation of the UVs with the presence of the free surface. However, a good knowledge of the free surface effect on the maneuverability is extremely useful especially in case of the AUVs in which this knowledge can be effectively employed to fine-tune the motion controllers before mission. Thus, this topic constitutes the main focus of the present thesis.

1.2 Objectives of the present thesis

The main objective of the present thesis is to evaluate the free surface effect on the hydrodynamics and dynamics of a shallowly submerged generic UV traveling close to the free surface in the horizontal plane.

Accordingly, the hydrodynamic captive tests, including the straight-ahead resis-

tance tests, drift tests and rotating arm tests, are performed on the bare hull of a generic UV model by using numerical simulations based on URANS equations with a Reynolds stress turbulence model. These tests are carried out over various submergence depths and proper ranges of UV surge, sway and yaw velocity components. The numerical simulations are conducted in the commercial code STARCCM+ [37], which solves the integral forms of the URANS and continuity equations over unstructured grids by using the finite volume method [38]. Additionally, for the purpose of free surface modeling the VOF method [37, 39] is used.

Herein, in order for dynamic stability evaluation of the UV in the horizontal plane over various submergence depths, the forces and moments obtained from the simulations of the drift and rotating arm tests are used to calculate the linear hydrodynamic coefficients over various submergence depths by using the linear least squares method.

Furthermore, the maneuverability evaluation for various submergence depths is performed by using the standard equations of motion proposed by GERTLER e HAGEN [1]. For this purpose, the forces and moments obtained from the simulations of the straight-ahead resistance, drift and rotating arm tests over various submergence depths are implemented in this model. In this regard, as the hydrodynamic axial force acting on a shallowly submerged UV close to the free surface obtained from the straight-ahead resistance tests has an oscillatory behavior with respect to the axial velocity component (as opposed to the axial force acting on the totally submerged one, which has a quadratic behavior), this force component is stored in a one-dimensional tabular form over various submergence depths, and a cubic interpolation is used to express this component in the maneuvering equations. Apart from the axial force arising from the axial velocity component, the rest of the hydrodynamic forces and moments obtained from the captive tests are implemented in the maneuvering equations by fitting them to odd/even quadratic polynomial functions in terms of the UV velocity components. Additionally, analytical equations are used to calculate the forces and moments due to the UV accelerations, thrust and rudder, which all are assumed to remain constant with respect to submergence depth.

In this work, a 1/1-scale of the bare hull axisymmetric SUBOFF geometry with principal dimensions presented by GROVES et al. [40] is used as the generic UV to fulfill the main objective of this thesis. This UV model was developed by David Taylor Research Center (DTRC) to compare the numerical prediction of hydrodynamics of an axisymmetric hull with experimental data. Various experiments were planned and conducted for the model, such as ETEBARI et al. [41], WILSON-HAFFENDEN et al. [35], LIU e HUANG [42], RODDY [43] and HUANG e LIU [44]. The data obtained from these experiments are used for the purpose of validation of the numerical hydrodynamic captive tests performed in the present study.

11

1.2.1   Thesis organization

The present thesis is divided into the following chapters:

- Chapter 2 presents a brief description of the equations of motion of UVs for various submergence depths and the methodology to obtain the external forces and moments acting on the UVs. Furthermore, the procedure to solve the equations of motion together with a brief description of the standard maneuvers are presented. This chapter also presents the numerical methodology, including the numerical model, geometry, computational conditions, computational domains, boundary conditions and grid structures, used in this thesis.

- Chapter 3 deals with the verification and validation of the numerical model used in this thesis to perform the hydrodynamic tests. In this chapter, the verification process encompasses a grid convergence study together with the evaluation of the support effect used in the experiments conducted by WILSON-HAFFENDEN *et al.* [35] on the forces and moments exerted on the SUBOFF UV. Furthermore, the validation includes the comparison of the calculated forces and moments against the measured ones provided by ETEBARI *et al.* [41], WILSON-HAFFENDEN *et al.* [35], LIU e HUANG [42], RODDY [43] and HUANG e LIU [44].

- Chapter 4 presents the results regarding the hydrodynamic forces and moments generated by the velocity components on the UV obtained from the numerical simulations, together with the hydrodynamic coefficients over various submergence depths. Additionally, this chapter provides a detailed analysis of the free surface effect on the hydrodynamics of the SUBOFF axisymmetric UV undergoing steady motions in the horizontal plane. This chapter further presents the results of the dynamic stability of the SUBOFF UV in the horizontal plane along with the maneuvering simulations of the UV for various submergence depths.

- Finally, Chapter 5 summarizes the main conclusions, findings and suggestions for future works and a list of accepted/submitted publications derived from the current thesis is presented in Appendix D.

Chapter 2

Methodology

This chapter presents a brief description of the equations of motion of UVs for various submergence depths and the methodology to obtain the external forces and moments acting on the UVs in the horizontal plane. Furthermore, the procedure to solve the equations of motion together with a brief description of the standard maneuvers are presented. This chapter also presents the numerical methodology, including the numerical model, geometry, computational conditions, computational domains, boundary conditions and grid structures, used in this thesis.

2.1   Dynamics of underwater vehicles

The body-fixed $sx_0y_0z_0$ and earth-fixed $oxyz$ coordinate systems that are used in this study to analyze the dynamics of the UVs are shown in Figure 2.1. Origin o of the earth-fixed coordinate system coincides with the calm water free surface level and positive z-axis points downward. Additionally, origin s of the body-fixed frame is located at the axial location of $0.462L$ from the nose with positive x_0-axis points toward the bow and y_0-axis points positively toward the starboard. Herein, L denotes the UV overall length.
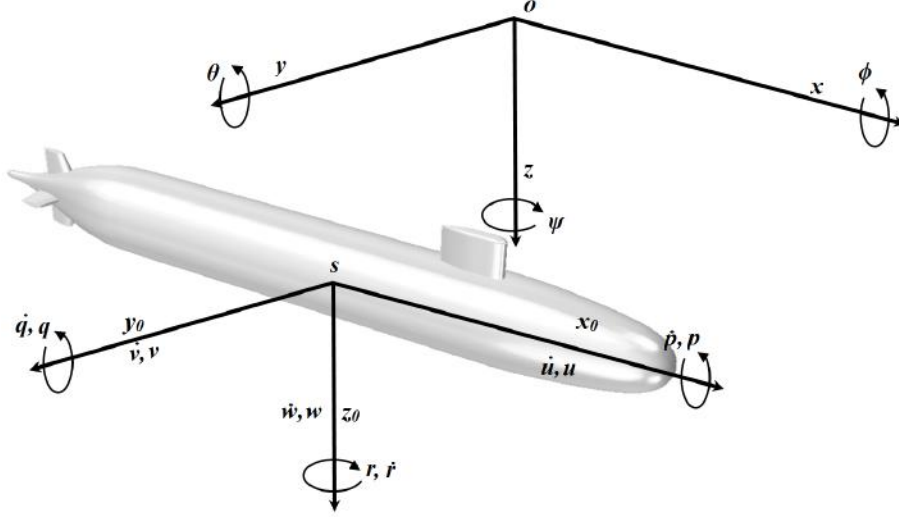
Figure 2.1: Body-fixed $sx_0y_0z_0$ and earth-fixed $oxyz$ coordinate systems used to express the dynamics of the UVs

The position and orientation vectors of the UV relative to the earth-fixed reference frame are expressed as $\eta_1 = [x, y, z]$ and $\eta_2 = [\phi, \theta, \psi]$, respectively (Figure 2.1) [45, 46]. The orientations about x-axis, y-axis and z-axis are expressed using Euler angles ϕ, θ and ψ, respectively (see Figure 2.1) [45]. u, v, w, p, q and r are utilized to denote the velocity components with respect to the body-fixed frame (Figure 2.1) [45, 46]. In this regard, u, v and w are the linear axial, lateral and vertical velocity components, respectively, while p, q and r are the angular roll, pitch and yaw velocity components, respectively, of the UV. Additionally, X, Y, Z, K, M and N are used to describe the forces and moments acting on the UV in the body-fixed frame [45, 46]. In this regard, X indicates the axial force, Y the lateral force, Z the vertical force, K the rolling moment, M the pitching moment and N the yawing moment.

The linear velocity vector of the UV with respect to the earth-fixed coordinate system, which is integrated with respect to time to calculate the UV trajectory, is obtained as follows [45]:

$$\dot{\eta}_1 = J_1(\eta_2)v_1, \qquad (2.1)$$

where $v_1 = [u, v, w]^T$ and $J_1(\eta_2)$ is calculated as:

$$J_1(\eta_2) = \begin{bmatrix} c\psi c\theta & -s\psi c\phi + c\psi s\theta s\phi & s\psi s\phi + c\psi c\phi s\theta \\ s\psi c\theta & c\psi c\phi + s\phi s\theta s\psi & -c\psi s\phi + s\theta s\psi c\phi \\ -s\theta & c\theta s\phi & c\theta c\phi \end{bmatrix}, \qquad (2.2)$$

where c and s stand for the cosine and sine functions. In addition, the Euler rate vector $\dot{\eta}_2 = \left[\dot{\phi}, \dot{\theta}, \dot{\psi}\right]^T$, which is integrated with respect to time to restore the UV

14

orientation vector, is calculated in terms of the angular velocity vector $v_2 = [p, q, r]^T$ of the UV as follows [45]:

$$\dot{\eta}_2 = J_2(\eta_2) v_2, \tag{2.3}$$

where $J_2(\eta_2)$ is calculated as:

$$J_2(\eta_2) = \begin{bmatrix} 1 & \text{s}\phi\text{t}\theta & \text{c}\phi\text{t}\theta \\ 0 & \text{c}\phi & -\text{s}\phi \\ 0 & \frac{\text{s}\phi}{\text{c}\theta} & \frac{\text{c}\phi}{\text{c}\theta} \end{bmatrix}. \tag{2.4}$$

where t stands for the tangent functions. Note that $J_2(\eta_2)$ is not defined for $\theta = \pm 90°$. This is not a problem here, as we are considering the motions solely in the horizontal plane.

After a brief description of kinematics of the UVs, in the following section, the standard equations of motion proposed by GERTLER e HAGEN [1] for maneuvering predictions of totally submerged UVs in the horizontal plane are presented.

2.1.1 Maneuvering equations for totally submerged UVs in the horizontal plane

The standard equations of motion in non-dimensional form proposed by GERTLER e HAGEN [1] for maneuvering predictions of totally submerged UVs in the horizontal plane can be written as follows:

Surge:

$$\begin{aligned}
m'[\dot{u}' - v'r' &- x'_G r'^2] = \\
X'_{\dot{u}}\dot{u}' & \\
&+ X'_{u|u|} u' \, |u'| + X'_{vv} v'v' + X'_{rr} r'r' \\
&+ X'_{\delta r \delta r} \delta_r^2 \\
&+ T'(1 - t),
\end{aligned} \tag{2.5}$$

Sway:

$$\begin{aligned}
m'[\dot{v}' + u'r' &+ x'_G \dot{r}'] = \\
Y'_{\dot{v}}\dot{v}' &+ Y'_{\dot{r}}\dot{r}' \\
&+ Y'_{v}v' + Y'_{v|v|} v' \, |v'| + Y'_{r}r' + Y'_{r|r|} r' \, |r'| \\
&+ Y'_{\delta r}\delta_r,
\end{aligned} \tag{2.6}$$

Yaw:

$$I'_z \dot{r}' + m'[x'_G(\dot{v}' + u'r')] =$$
$$N'_{\dot{v}}\dot{v}' + N'_{\dot{r}}\dot{r}'$$
$$+ N'_v v' + N'_{v|v|}v'\,|v'| + N'_r r' + N'_{r|r|}r'\,|r'| \tag{2.7}$$
$$+ N'_{\delta r}\delta_r,$$

where the primed symbols stand for the dimensionless variables. Note that the nondimensionalisation is carried out based on LEWIS [3] and SNAME [47]. In this regard, to obtain the nondimensional form, the force terms are divided by $\frac{1}{2}\rho U^2 L^2$ while the moment terms are divided by $\frac{1}{2}\rho U^2 L^3$, where U indicates the UV overall speed in the horizontal plane, i.e., $U = \sqrt{u^2 + v^2}$ and L is the UV overall length. x'_G is the dimensionless x_0 coordinate of the center of gravity, m' is the dimensionless UV mass and I'_z is the dimensionless moment of inertia about z_0 axis. In Equations 2.5, 2.6 and 2.7 it is assumed that the axis through $sx_0 y_0 z_0$ are the principal axes of inertia, and y_0 and z_0 coordinates of the center of gravity are zero, i.e., $y'_G = z'_G = 0$. Additionally, $X'_{\dot{u}}, Y'_{\dot{v}}, Y'_{\dot{r}}, N'_{\dot{v}}$ and $N'_{\dot{r}}$ are the dimensionless hydrodynamic added-mass coefficients. Moreover, $X'_{u|u|}$, $X'_{vv}, Y'_v, Y'_{v|v|}, N'_v, N'_{v|v|}$, $X'_{rr}, Y'_r, Y'_{r|r|}, N'_r$ and $N'_{r|r|}$ are the dimensionless hydrodynamic coefficients arising from the velocity components. Furthermore, $X'_{\delta r \delta r}, Y'_{\delta r}, N'_{\delta r}$ are the dimensionless hydrodynamic coefficients of the rudder and δ_r is the effective angle of deflection of rudder relative to the inflow velocity. Also, t is the thrust deduction factor, and T' is the dimensionless thrust force generated by the propeller.

As can be seen in Equations 2.5, 2.6 and 2.7, the external forces and moments (right hand side of these equations) are considered as a superposition of several forces and moments as follows:

- The hydrodynamic forces and moments exerted on a UV due to acceleration or deceleration:

$$\text{Axial force} = X'_{\dot{u}}\dot{u}', \tag{2.8}$$

$$\text{Lateral force} = Y'_{\dot{v}}\dot{v}' + Y'_{\dot{r}}\dot{r}', \tag{2.9}$$

$$\text{Yaw moment} = N'_{\dot{v}}\dot{v}' + N'_{\dot{r}}\dot{r}', \tag{2.10}$$

- The hydrodynamic forces and moments acting on a UV due to the linear and angular velocities of the UV:

$$\text{Axial force} = X'_{u|u|}u'\,|u'| + X'_{vv}v'v' + X'_{rr}r'r', \tag{2.11}$$

$$\text{Lateral force} = Y'_v v' + Y'_{v|v|} v' \, |v'| + Y'_r r' + Y'_{r|r|} r' \, |r'| \,, \qquad (2.12)$$

$$\text{Yaw moment} = N'_v v' + N'_{v|v|} v' \, |v'| + N'_r r' + N'_{r|r|} r' \, |r'| \,, \qquad (2.13)$$

Equation 2.11 shows that the relationship between the X-force and u is expressed by a purely odd quadratic polynomial function. Since, if the vehicle moves forward ($u > 0$) it experiences a force toward aft; conversely, if the vehicle moves aftward ($u < 0$) it experiences a force toward bow. On the other hand, the X-force in terms of v and r velocity components is approximated by purely even quadratic polynomial functions. Since, for instance, a UV swaying to the starboard ($v > 0$) or port ($v < 0$) will experience the same reaction in x_0 direction. The same argument is applicable for a UV with an angular yaw velocity r.

Moreover, Equations 2.12 and 2.13 show that purely odd quadratic polynomial functions are used to approximate the lateral force Y and yaw moment N arising from the lateral velocity v and the angular yaw velocity r. Since, for instance, if the UV sways to starboard ($v > 0$), it will experience a counteracting force toward the port ($Y < 0$); while, if a UV sways to port ($v < 0$), it will experience a counteracting force toward the starboard ($Y > 0$). Also, as the N-moment is generated by the Y-force about the z_0-axis, the N-moment follows the same behavior as that of the Y-force. The same argument is applicable for a UV with an angular yaw velocity r.

- Hydrodynamic forces and moments generated by control surfaces:

  In the present study, it is assumed that the UV under consideration is merely equipped with a vertical rudder in the aft region, which is used for maneuvering in the horizontal plane (Figure 2.2).

Figure 2.2: The UV under consideration equipped with a vertical rudder in the stern region

Additionally, the contribution of the rudder to the forces and moments in the horizontal plane is as follows:

$$\text{Axial force} = X'_{\delta r \delta r} \delta_r^2, \qquad (2.14)$$

$$\text{Lateral force} = Y'_{\delta r} \delta_r, \qquad (2.15)$$

$$\text{Yaw moment} = N'_{\delta r}\delta_r, \tag{2.16}$$

Equations 2.14, 2.15 and 2.16 demonstrate that the relationship between the X-force and δ_r is purely even, while this relationship for the Y-force and N-moment is purely odd.

The effective angle of deflection of rudder δ_r is equal to the sum of the user-defined deflection (δ_{r0}) and the deflection formed due to the linear lateral and angular yaw velocity components (δ'_r) (Figure 2.3):

$$\delta_r = \delta_{r0} + \delta'_r, \tag{2.17}$$

where δ'_r is defined as:

$$\delta'_r = \mathrm{atan}\frac{x_r r - v}{u}, \tag{2.18}$$

where x_r is the distance between the rudder's location and the center of the local coordinate system.
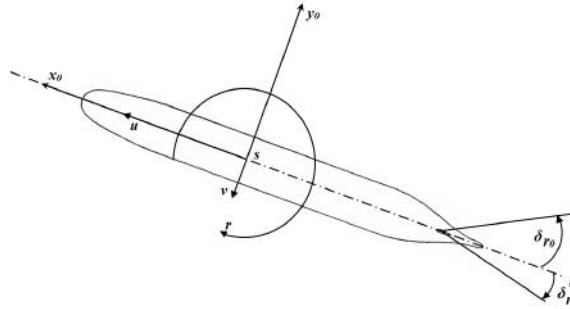
Figure 2.3: Definition of the δ_{r0} and δ'_r

- The hydrodynamic force generated by propeller:

  Herein, it is assumed that the UV is equipped with a propeller in the stern downstream the rudder, which produces the following axial force:

$$\text{Axial force} = T'(1 - t), \tag{2.19}$$

Furthermore, Equations 2.5, 2.6 and 2.7 lack the hydrodynamic forces and moments related to the coupling effects between the sway and yaw degrees of freedom, such as $X'_{vr}v'r'$. Since the presence of these terms requires the dedication of much significant time to determine the external forces and moments resulting from them while yet, as shown by GAO *et al.* [48], these coupling terms show limited effect on the total forces and moments and thus can be removed.

2.1.2 Free surface effect on the hydrodynamics and dynamics of a shallowly submerged UV

An immediate consequence of a UV traversing near the free surface is the creation of surface gravity waves that are stationary with respect to the body. The creation of this gravity wave system is attributed to the interaction between the dynamic pressure distribution around the hull and the free surface.

In case of a shallowly submerged UV moving beneath the free surface in the horizontal plane, there are three components of velocity, i.e., the axial (surge) u, the lateral (sway) v and the angular yaw r, interacting with the flexible free surface, which deforms the free surface in both lateral and longitudinal directions. In other words, the wave system of a shallowly submerged UV traveling beneath the free surface in the horizontal plane emanates from the interaction of the free surface with both the longitudinal and circumferential dynamic pressure distributions, which arise from the axial, lateral and angular yaw velocity components of a UV in the horizontal plane.

This wave system is a combination of several wave systems created by the dynamic pressure distribution along the body and probably is a function of UV overall length, body form and velocity components [49]. In this respect, the wave system generated by a shallowly submerged UV traveling along a straight path in a deep-water condition resembles closely the classical Kelvin wave pattern [10].

Applying the dispersion relation of linear surface waves in a deep-water condition to the stationary wave system generated by a UV traveling along a straight path yields the following relationship between the wavelength and UV overal speed U [3]:

$$\lambda = 2\pi \frac{U^2}{g} \cos^2\Theta. \tag{2.20}$$

Theta $(\Theta, \frac{-\pi}{2} < \Theta < \frac{\pi}{2})$ is the angle between the UV's direction of travel and the vector normal to the crest of the wave. Equation 2.20 can be rewritten as follows:

$$\frac{\lambda}{L} = 2\pi \frac{U^2}{gL} \cos^2\Theta = 2\pi F_n^2 \cos^2\Theta, \tag{2.21}$$

where $F_n = \frac{U}{\sqrt{gL}}$ is Froude number. This relation suggests that for $F_n > \frac{1}{\sqrt{2\pi}} \approx 0.4$ the wavelength exceeds the UV overall length L.

As is well known from NEWMAN [21], the energy required for the creation of the surface wave system leads to an increase in the hydrodynamic forces generated by the velocity components on a shallowly submerged UV. Likewise, as shown by MAALI AMIRI *et al.* [19], the increase in the forces induced by the velocity components with a decrease in submergence depth can also be explained through the effect of the free surface deformations on the dynamic pressure distribution along

the length of the UV hull. In this regard, MAALI AMIRI *et al.* [19] show that the crests and troughs of the self-induced wave system of a shallowly submerged UV modify the dynamic pressure distribution around the UV hull by creating local regions of high and low dynamic pressure, respectively, along the UV length.

Thus, it can be inferred that a crucial effect of the wave system generated by a shallowly submerged UV is the modification that it introduces into the dynamic pressure distribution around the submerged body. In this regard, the degree of modification introduced into the dynamic pressure distribution around the UV hull by the free surface deformations depends on submergence depth. The less the submergence depth the more will be the free surface deformations, which consequently increases the free surface effect on the dynamic pressure distribution around the hull [19].

Accordingly, the modification of the dynamic pressure distribution across the length, width and depth of the hull affects all the external forces and moments exerted on the UV hull and likely gives rise to the generation of the forces and moments in the vertical plane [19].

As shown in section 2.1.1, the external forces and moments are considered as a superposition of the hydrodynamic forces and moments arising from the velocity and acceleration components, hydrodynamic forces and moment due to rudder and the hydrodynamic axial force generated by the propeller. From a theoretical point of view, all of these external forces and moments presented on the right hand side of Equations 2.5, 2.6 and 2.7 are subject to change as a result of approaching the free surface. However, for the sake of simplicity, in the present thesis, the free surface effect is merely considered on the hydrodynamic forces and moments arising from the velocity components. Therefore, the above discussion is continued for the hydrodynamic forces and moments resulting from the velocity components of the UV in the horizontal plane.

Free surface effect on the hydrodynamic forces and moments generated by the velocity components

Generally, as a UV approaches the free surface, the axial hydrodynamic forces X arising from the velocity components are prone to an increase. As is well known, this is associated with the energy required for the creation of the surface wave system generated by the UV as it approaches the free surface [21]. On the other hand, as the submergence depth is reduced, the hydrodynamic lateral forces Y and yaw moments N resulting from the lateral and yaw angular velocity components, are bound to either an increase or decrease, depending on the behavior of the Y-force distribution along the length of the UV.

Anyhow, due to the inevitable change in X, Y and N generated by the velocity

components with respect to submergence depth, for a shallowly submerged UV, these forces and moments are functions of both the velocity components and submergence depth h.

As can be seen in Equations 2.5, 2.6 and 2.7, for a totally submerged UV, the hydrodynamic forces and moments arising from the velocity components are approximated as quadratic polynomial functions in terms of the velocity components of the UV.

On the other hand, to account for the free surface effect on the UV maneuverability the question may come up that whether to maintain the equations of motion for a totally submerged UV given in Equations 2.5, 2.6 and 2.7 with the hydrodynamic forces and moments obtained for a specific submergence depth, or to formulate a new set of equations of motion with the hydrodynamic forces and moments defined explicitly in terms of both the velocity components and submergence depth.

In this regard, extending the quadratic polynomial functions, which approximate the hydrodynamic forces and moments in terms of the UV velocities, to account explicitly for the effect of the submergence depth increases notably the regression problem with considerable identification effort. Since, as shown by MAALI AMIRI *et al.* [19] and DAWSON [10], the free surface effect on the hydrodynamic forces and moments induced by the velocity components increases exponentially with a decrease in h.

Therefore, in the present research, for the sake of simplicity, and also to fulfill the main purpose of this study, the maneuverability analysis is performed by using Equations 2.5, 2.6 and 2.7 with the hydrodynamic forces and moments arising from the velocity components obtained at several submergence depths beneath the free surface.

Thus, herein, an attempt is made to propose appropriate functions that capture the behavior of the hydrodynamic forces and moments acting on a shallowly submerged UV in terms of each velocity component at a desired submergence depth beneath the free surface. For this purpose, the forces and moments resulting from each velocity component are closely examined as follows:

- Axial X-force generated by the axial velocity component u:

In case of a shallowly submerged UV traveling beneath the free surface, the axial X-force has an oscillatory behavior with respect to the axial velocity component, which emanates from the interference effects between the dominant wave systems inside the submarine wake [19]. Therefore, the utilization of a quadratic polynomial function in terms of u velocity component, as presented in Equation 2.5, may not adequately represent the axial force as a function of u. Thus, the axial force exerted on a shallowly submerged UV hull traveling beneath the free surface is stored in a

one-dimensional tabular form at various submergence depths as $X_{f(u,h)}$, and a cubic interpolation is used to express the axial force X as a function of axial velocity u in the maneuvering equations.

- Hydrodynamic forces and moment arising from the lateral velocity component v:

In this case, although the advent of the wave-making resistance modifies the forces and moment arising from the lateral velocity v, as is shown later in the result section, the forces and moment arising from the lateral velocity component v acting on a shallowly submerged UV, the same as those acting on a totally submerged one, are approximated reasonably well by using quadratic polynomial functions in terms of sway velocity v. This is due to the negligible interference effects between the wave systems generated by the sway velocity component v at points along the body length, which unlike the axial force resulting from the u velocity component does not provoke an oscillatory behavior in the forces and moment generated by the lateral velocity v. Therefore, in this case, the hydrodynamic forces and moment are expressed as follows:

$$\text{Axial force} = X'_{vv,h} v' v', \tag{2.22}$$

$$\text{Lateral force} = Y'_{v,h} v' + Y'_{v|v|,h} v' \left| v' \right|, \tag{2.23}$$

$$\text{Yaw moment} = N'_{v,h} v' + N'_{v|v|,h} v' \left| v' \right|, \tag{2.24}$$

where coefficients $X'_{vv,h}, Y'_{v,h}, Y'_{v|v|,h}, N'_{v,h}$ and $N'_{v|v|,h}$ are the dimensionless sway hydrodynamic coefficients as a function of submergence depth h, which are obtained at several submergence depths in a range of $h_{min} \leq h \leq \infty$.

- Hydrodynamic forces and moment generated by the angular yaw velocity component r:

In this case again, as is shown later in the result section, the forces and moment generated by the angular yaw velocity component r on a shallowly submerged UV, the same as those acting on a totally submerged one, are approximated reasonably well using quadratic polynomial functions in terms of r. This is also due to the negligible interference effects between the wave systems generated by the yaw velocity component r at points along the body length, which contrary to the axial force resulting from the u velocity component does not provoke an oscillatory behavior in the forces and moment caused by the angular yaw velocity. Therefore, in this case, the hydrodynamic forces and moment are expressed as follows:

$$\text{Axial force} = X'_{rr,h} r' r', \tag{2.25}$$

$$\text{Lateral force} = Y'_{r,h}r' + Y'_{r|r|,h}r'\left|r'\right|, \tag{2.26}$$

$$\text{Yaw moment} = N'_{r,h}r' + N'_{r|r|,h}r'\left|r'\right|, \tag{2.27}$$

where coefficients $X'_{rr,h}$, $Y'_{r,h}$, $Y'_{r|r|,h}$, $N'_{r,h}$ and $N'_{r|r|,h}$ are the dimensionless yaw hydrodynamic coefficients as a function of submergence depth h, which are obtained at several submergence depths in a range of $h_{min} \leq h \leq \infty$.

Therefore, the maneuvering equations for a shallowly submerged UV in the horizontal plane are closely similar to the maneuvering equations for a deeply submerged one presented in Equations 2.5, 2.6 and 2.7. However, the forces and moments generated by the velocity components are obtained at several submergence depths in a range of $h_{min} \leq h \leq \infty$ to reflect the effect of the presence of the free surface on the maneuverability of the UV in the horizontal plane.

2.1.3 Parameter identification

The mathematical model presented in section 2.1.1 includes several unknown parameters, which analytical and numerical methods are used to identify them. In this regard, this section deals with both the identification procedure of the forces and moments arising from the acceleration components, rudder and thrust, based on the existing analytical methods in the literature, and the identification procedure of the forces and moments induced by the velocity components using the hydrodynamic tests.

Hydrodynamic forces and moments arising from the acceleration components

In this section, the hydrodynamic forces and moments arising because of the acceleration components are estimated using the analytical equations proposed by HUMPHREYS e WATKINSON [50], which are obtained for a prolate-spheroid moving through an infinite volume of stationary ideal fluid. In this regard, the UV is considered as a prolate-spheroid with axes equal to the length and maximum diameter of the UV as follows:

$$\frac{x^2}{a^2} + \frac{y^2}{b^2} + \frac{z^2}{c^2} = 1, b = c, a > b, \tag{2.28}$$

where $a = \frac{L}{2}$ and $b = c = \frac{\text{Maximum diamter of the UV}}{2}$. Accordingly, the following expressions are given by HUMPHREYS e WATKINSON [50] to estimate the hydrodynamic added-mass coefficients of a prolate-spheroid in terms of its geometrical characteristics:

$$X'_{\dot{u}} = -k_1 m', \tag{2.29}$$

$$Y'_{\dot{v}} = -k_2 m', \tag{2.30}$$

$$N'_{\dot{r}} = -k' I'_z, \tag{2.31}$$

$$Y'_{\dot{r}} = (x'_B - x'_G) Y'_{\dot{v}}, \tag{2.32}$$

$$N'_{\dot{v}} = (x'_B - x'_G) Y'_{\dot{v}}, \tag{2.33}$$

where x'_B indicates the dimensionless x_0 coordinate of the center of buoyancy. Furthermore, the k-factors in Equations 2.29, 2.30 and 2.31 are defined as follows:

$$k_1 = \frac{\alpha_0}{2 - \alpha_0}, \tag{2.34}$$

$$k_2 = \frac{\beta_0}{2 - \beta_0}, \tag{2.35}$$

$$k' = \frac{e^4(\beta_0 - \alpha_0)}{(2 - e^2)\left[2e^2 - (2 - e^2)(\beta_0 - \alpha_0)\right]}, \tag{2.36}$$

where α_0, β_0 and e are calculated as follows:

$$\alpha_0 = \frac{2(1 - e^2)}{e^3}\left(\frac{1}{2}\ln\left[\frac{1 + e}{1 - e}\right] - e\right), \tag{2.37}$$

$$\beta_0 = \frac{1}{e^2} - \frac{1 - e^2}{2e^3}\ln\left[\frac{1 + e}{1 - e}\right], \tag{2.38}$$

$$e^2 = 1 - \left(\frac{b}{a}\right)^2. \tag{2.39}$$

Hydrodynamic forces and moments generated by the rudder

In this section, to calculate the hydrodynamic forces and moment generated by the rudder at an effective angle of deflection δ_r, the semi-empirical formulations presented by DE BARROS *et al.* [51] and FIELD [9] are used. According to FIELD [9], to calculate the hydrodynamic forces and moment related to rudder, first the lift coefficient C_L of the rudder is estimated as:

$$C_L = \frac{1.8\pi AR_e}{1.8 + \cos\gamma_p\sqrt{4 + \frac{AR_e^2}{(\cos\gamma_p)^4}}}, \tag{2.40}$$

where AR_e is the effective aspect ratio. AR_e is defined as a function of the rudder span and hull radius at the rudder location and is estimated from the curves presented by DE BARROS *et al.* [51] as a percentage of the geometrical aspect ratio of the isolated rudder. Accordingly, based on DE BARROS *et al.* [51], the effective aspect ratio of the rudder (AR_e) in the presence of the body is estimated as follows:

$$AR_e = f(b_v, r)AR, \qquad (2.41)$$

where AR is the geometrical aspect ratio of the isolated rudder, b_v indicates the rudder span and r is the hull radius at one-fourth of the root-chord length. The function $f(b_v, r)$ is determined from the curves represented in Figure 2.4. In this figure, $\lambda = \frac{\text{tip chord length}}{\text{root chord length}}$ is the taper ratio.
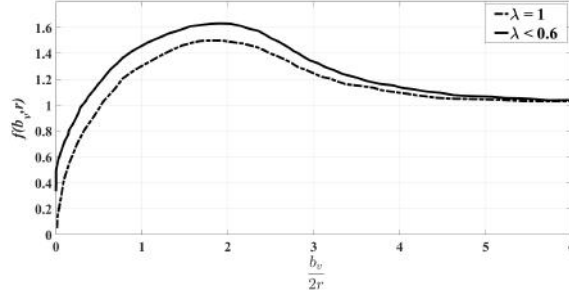
Figure 2.4: Ratio of AR_e to AR [51]

Additionally, γ_p is the sweep angle at one-fourth of the chord length, as shown in Figure 2.5. After the calculation of C_L, the values of the hydrodynamic forces and moment generated by rudder are quantified as, FIELD [9]:

$$\text{Lateral force} = 0.5\rho S_{rud} I_{RB} C_L U^2 \delta_r, \qquad (2.42)$$

$$\text{Axial force} = -0.5\rho S_{rud} I_{RB} \left\{ \frac{1}{0.9\pi AR_e} \right\} C_L^2 U^2 \delta_r^2, \qquad (2.43)$$

$$\text{Yaw moment} = -0.5\rho S_{rud} x_r I_{RB} C_L U^2 \delta_r, \qquad (2.44)$$

where S_{rud} is the rudder surface area. In Equations 2.42, 2.43 and 2.44, I_{RB} is an empirical coefficient proposed by DE BARROS $et\ al.$ [51] to consider the interference effect between the body and the rudder, which is determined in Figure 2.6.
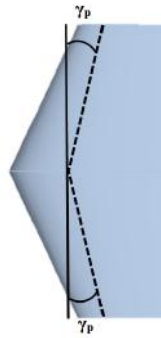
Figure 2.5: Definition of the γ_p
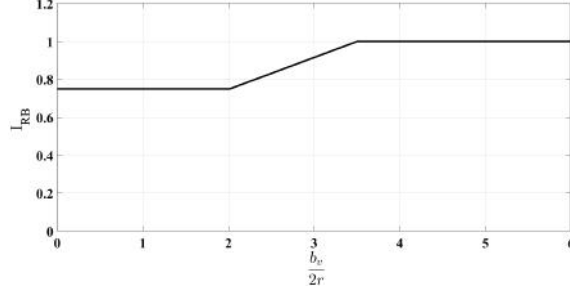
Figure 2.6: I_{RB} is an empirical coefficient proposed by [51] to consider the interference effect between the body and the rudder

The location of the forces generated by the rudder is assumed to be axially at one-fourth of the chord length from the leading edge. Equations 2.42, 2.43 and 2.44 are applicable for $\delta r < 25°$ (FIELD [9]).

Note that a positive deflection of rudder generates a negative moment about z_0-axis together with a positive force in y_0 direction, while a negative deflection of rudder imposes a positive moment about z_0-axis along with a negative force in y_0 direction. This explains the minus sign on the right hand side of Equation 2.44.

Thrust force

The thrust force T generated by the propeller (Equations 2.19) is obtained as follows:

$$T = K_T(J)\rho n^2 D_p^4, \tag{2.45}$$

where ρ indicates the fluid density, n the propeller rotation rate, D_p the propeller diameter and $K_T(J)$ the normalized thrust coefficient, which is expressed as a function of advance velocity ratio J. J is defined as:

$$J = \frac{u_A}{nD_p}, \tag{2.46}$$

where u_A indicates the mean flow velocity at the propeller plane, which is related to u through the following equation:

$$u_A = u(1 - w), \tag{2.47}$$

where w is referred to as the wake fraction.

Thrust coefficient $K_T(J)$ can be obtained from the open-water propeller performance curves. In this regard, the following thrust coefficient $K_T(J)$ of the generic seven bladed propeller E1619 with the general characteristics presented in Table 2.1 is used to estimate the thrust force:

$$K_T = -0.1941J^2 - 0.2437J + 0.5375. \tag{2.48}$$

26

The E1619 propeller is manufactured and tested in the INSEAN towing tank, as reported by SEZEN *et al.* [52].

Table 2.1: General characteristics of the E1619 propeller [52]

D_p (m)	0.262
Z	7
P/D_p	1.15
D_h/D_p	0.226

Furthermore, to estimate the mean flow velocity at the propeller plane u_A, a value of 0.1 is considered for the wake fraction w, as suggested by TRIANTAFYLLOU e HOVER [53]. Moreover, TRIANTAFYLLOU e HOVER [53] recommend to assign a value of 0.2 to the thrust deduction factor t.

Hydrodynamic forces and moments arising from the velocity components

This section deals with the process of identification of the hydrodynamic forces and moments arising from the velocity components acting on both totally submerged and shallowly submerged UVs, based on a regression analysis.

- Hydrodynamic axial force due to the axial velocity component u

The axial force arising from the axial velocity component u can be obtained through the straight-ahead resistance tests. In these tests, the model with no angle of incidence is suspended from a carriage in a towing tank and is towed in several u velocities [1, 3].

The axial hydrodynamic coefficient $X'_{u|u|}$ given in Equation 2.11 for a totally submerged UV is estimated by fitting the polynomial function to the axial forces obtained from the straight-ahead tests via the linear least squares method.

Additionally, as mentioned earlier, in the maneuvering simulations with the presence of the free surface, a cubic interpolation is used to express the axial force $X_{f(u,h)}$ in the equations of motion. Since at this condition, due to its oscillatory behavior, the axial force $X_{f(u,h)}$ arising from the axial velocity is stored in a one-dimensional tabular form.

- Hydrodynamic forces and moment generated by the lateral velocity component v

The forces and moment resulting from the lateral velocity component v can be obtained through the drift tests (Figure 2.7). In these tests, the model with a certain

angle of drift (β) is mounted from a carriage in a towing tank and is towed in several angles of drift, while keeping the speed U constant [1, 3].

The sway hydrodynamic coefficients $X'_{vv}, Y'_v, Y'_{v|v|}, N'_v$ and $N'_{v|v|}$ given in Equations 2.11, 2.12 and 2.13 for a totally submerged UV and the coefficients $X'_{vv,h}, Y'_{v,h}, Y'_{v|v|,h}, N'_{v,h}$ and $N'_{v|v|,h}$ given in Equations 2.22, 2.23 and 2.24 for a shallowly submerged one, are estimated by fitting the polynomials to the forces and moments obtained from the drift tests via the linear least squares method.
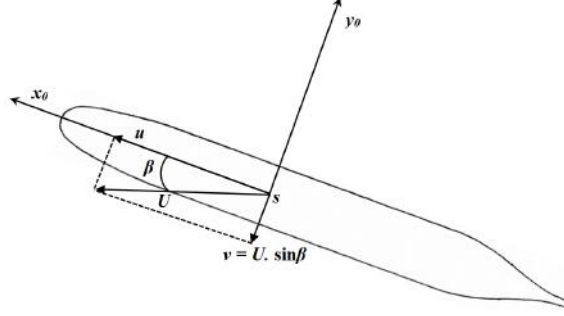
Figure 2.7: A UV undergoing the drift tests

- Hydrodynamic forces and moment arising from the angular yaw velocity r

The forces and moment due to the yaw rate r, can be obtained by performing the rotating arm tests (Figure 2.8). In these tests, while the axial velocity, which is a product of the yaw rate and the radius of rotation, is kept constant the yaw rate is changed through changing the radius of rotation. The tests are performed on a model with zero incidence at a number of angular yaw velocities [2, 3].

The yaw hydrodynamic coefficients $X'_{rr}, Y'_r, Y'_{r|r|}, N'_r$ and $N'_{r|r|}$ given in Equations 2.11, 2.12 and 2.13 for a totally submerged UV and the coefficients $X'_{rr,h}, Y'_{r,h}, Y'_{r|r|,h}, N'_{r,h}$ and $N'_{r|r|,h}$ given in Equations 2.25, 2.26 and 2.27 for a shallowly submerged one, are estimated by fitting the polynomials to the forces and moments obtained from the rotating arm tests via the linear least squares method.

2.1.4   Dynamic stability of UVs in the horizontal plane

To evaluate the dynamic stability of UVs in the horizontal plane, herein, the classical criterion presented by LEWIS [3] is used. This criterion is written as follows:

$$\frac{N'_r - m'x'_G}{Y'_r - m'} - \frac{N'_v}{Y'_v} > 0. \tag{2.49}$$

Equation 2.49 is obtained from the linearized equations of motion in sway and yaw directions. In this equation, the first term corresponds to the lever of the hydrodynamic moment generated by the angular yaw velocity component (l_r) and the second term corresponds to the lever of the hydrodynamic moment generated
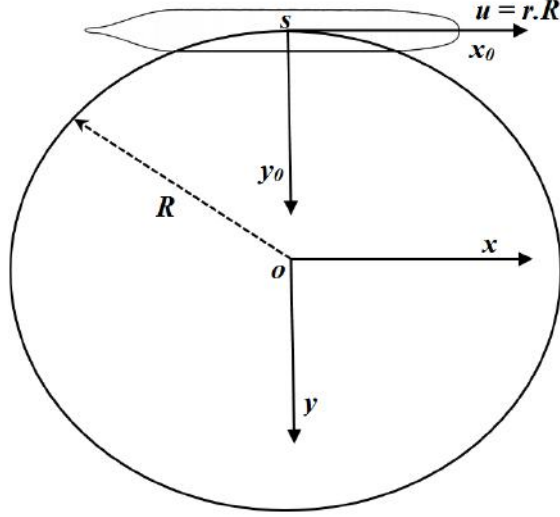
Figure 2.8: A UV undergoing the rotating arm test

by the lateral velocity component (l_v). Thus, the stability criterion states that for a UV to be stable the lever of the hydrodynamic moment generated by the angular yaw velocity component must be larger than the lever of the hydrodynamic moment generated by the lateral velocity component. In other words:

$$l_r - l_v > 0. \tag{2.50}$$

Additionally, taking into account the contribution of the rudder to the linear hydrodynamic coefficients arising from the lateral velocity and yaw rate, as presented by LEWIS [3], Equation 2.49 can be rewritten as follows:

$$\frac{N'_r - m'x'_G + x'_r N'_{\delta r}}{Y'_r - m' + x'_r Y'_{\delta r}} - \frac{N'_v - N'_{\delta r}}{Y'_v - Y'_{\delta r}} > 0. \tag{2.51}$$

Note that $N_{\delta r}$ is always negative and $Y_{\delta r}$ is always positive [3]. Accordingly, as mentioned by LEWIS [3], it can be inferred that the rudder always acts to stabilize the UV, even when it has no deflection. In other words, based on Equation 2.51, it can be clearly seen that the rudder contributes to the lever of the moment generated by the yaw rate, while it diminishes the lever of the moment induced by the sway velocity. Thus, in cases where the UVs are inherently unstable, a proper adjustment of rudder size can stabilize the UVs to a desirable level.

More generally, the dynamic stability criterion (SC) presented in Equation 2.51 for a UV traveling in the horizontal plane at a submergence depth h is written as follows:

$$SC = \frac{N'_{r,h} - m'x'_G + x'_r N'_{\delta r}}{Y'_{r,h} - m' + x'_r Y'_{\delta r}} - \frac{N'_{v,h} - N'_{\delta r}}{Y'_{v,h} - Y'_{\delta r}} > 0, \tag{2.52}$$

29

where the coefficients $N'_{r,h}, Y'_{r,h}, N'_{v,h}$ and $Y'_{v,h}$ are obtained at several submergence depths in a range of $h_{min} \leq h \leq \infty$ beneath the free surface to reflect the free surface effect on the dynamic stability of UVs over various submergence depths.

2.1.5   Numerical implementation of the equations of motion

To solve the equations of motion represented in Equations 2.5-2.7 for a totally submerged UV and a shallowly submerged one, it is convenient to separate the acceleration terms from the other terms. In this regard, the equations of motion for a UV traveling in the horizontal plane at a submergence depth h can be written as follows:

Surge:

$$(m' - X'_{\dot{u}})\,\dot{u}' = \{X'\}_{f(u,v,r,h)} + \{X'\}_{f(\delta r)} + \{T'(1-t)\}, \qquad (2.53)$$

Sway:

$$(m' - Y'_{\dot{v}})\,\dot{v}' + (m'x'_G - Y'_{\dot{r}})\,\dot{r}' = \{Y'\}_{f(u,v,r,h)} + \{Y'\}_{f(\delta r)}, \qquad (2.54)$$

Yaw:

$$(I'_z - N'_{\dot{r}})\,\dot{r}' + (m'x'_G - N'_{\dot{v}})\,\dot{v}' = \{N'\}_{f(u,v,r,h)} + \{N'\}_{f(\delta r)}, \qquad (2.55)$$

where to avoid working with large equations, the right hand sides are given in generic forms. From the above system of equations the acceleration components of the UV in the horizontal plane $(\dot{u}, \dot{v}, \dot{r})$ are obtained. Subsequently, to calculate the UV velocity, position and orientation, numerical integration based on the second-order improved Euler method is used. The second-order improved Euler method is significantly more accurate than the Euler method, since it uses the average of the slopes of the lines tangent to the function at both the beginning and end of an interval.

2.1.6   Evaluation of UV maneuverability

In order to assess the maneuvering capabilities of UVs, several standard maneuvers are put forward [3]. In the present thesis, to evaluate the free surface effect on the maneuverability of a UV, the turning and zigzag standard maneuvers are performed for various submergence depths, which are explained as follows:

Turning maneuver

To analyze the turning capability of a UV, the turning maneuver is performed. In this test, after achieving a steady advance velocity and a zero yaw rate, the rudder is deflected to either port or starboard until the yaw rate reaches to a constant value. Figure 2.9 shows a UV undergoing a turning maneuver under a command rudder deflection of $-\delta r_0$.

The information obtained from this test to analyze the turning ability are the advance, transfer, tactical diameter, turning diameter and drift angle, as shown in Figure 2.9 [3]. The advance and transfer are defined as the longitudinal and lateral distances, respectively, traveled by the UV when the yaw angle ψ changes $90°$. Similarly, the tactical diameter is defined as the lateral distance traveled by the UV when the yaw angle ψ changes $180°$.
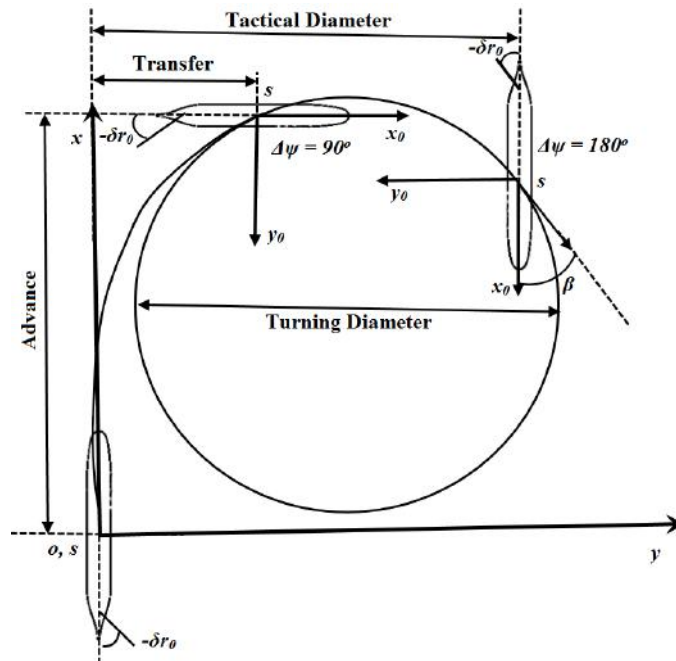
Figure 2.9: Trajectory of a UV undergoing the turning maneuver

Zigzag maneuver

To analyze the capability of the rudder to control the UV, i.e., to evaluate the course-keeping ability of the UV using the rudder, the zigzag test is performed. In this regard, after achieving a steady advance velocity using a zero command rudder deflection, the rudder is deflected δr_0 to either port or starboard, and is held until the yaw angle reaches the command rudder deflection δr_0. In this moment, the rudder is alternatively deflected to the other side with a command deflection angle of δr_0. Again, the rudder is held until the yaw angle reaches the command rudder deflection δr_0. Depending on the purpose of the test, this procedure is repeated for

31

a number of runs.

For instance, Figure 2.10 shows a typical graph containing the time histories of the command rudder deflection angle (δr_0) and the yaw angle (ψ) during a zigzag maneuver initiated at time zero. Note that a negative deflection of the rudder (deflection toward starboard) gives rise to a positive yaw angle, and a positive rudder deflection causes a negative heading angle. This explains the negative sign used to represent the rudder deflection in Figure 2.10.

The information obtained from this test to analyze the course-keeping ability of the UV are the first and second overshoot angles (ψ_{os1}, ψ_{os2} (Figure 2.10)), together with the times to execute the rudder for the n-th time, such as the second time t_{re2}, the third time t_{re3} and the fourth time t_{re4} (Figure 2.10)).
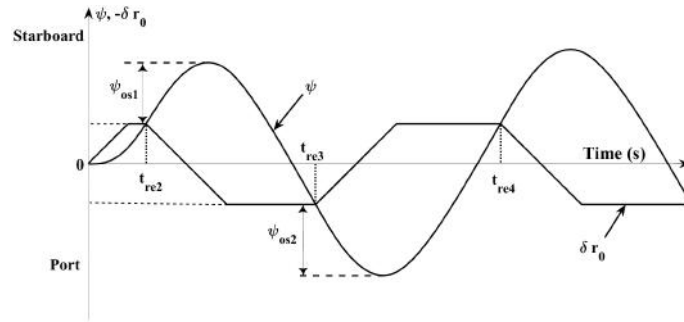
Figure 2.10: Time histories of the command rudder deflection angle (δr_0) and the yaw angle (ψ) of a UV undergoing the zigzag maneuver

2.2 Fluid flow characteristics around a totally submerged axisymmetric UV

As mentioned earlier, herein to investigate the free surface effect on the hydrodynamics and dynamics of an axisymmetric UV in the horizontal plane, relevant hydrodynamic captive tests are performed in this plane. In this regard, to have a better understanding of the free surface effect on the UV hydrodynamics and dynamics, a good knowledge of the general fluid flow characteristics around the totally submerged UV undergoing a steady drift and turning motion is extremely helpful. Thus, in the following sections, a brief description of the fluid flow characteristics around a totally submerged UV undergoing steady drift and turning motions is presented.

2.2.1 Fluid flow characteristics around a UV at steady drift

As shown in Figure 2.7, a UV at a steady drift angle β has two components of velocity, one parallel to the UV long axis (x_0) $u = U.\cos\beta$ and another one parallel

to the y_0 axis $v = U.\sin\beta$. The latter, which is also the lateral velocity component of the UV, gives rise to the development of a three-dimensional separation called the crossflow separation (WETZEL *et al.* [24], CHESNAKAS e SIMPSON [25], PHILLIPS *et al.* [54] and KIM *et al.* [55]).

To explain the reason for the development of the crossflow separation around the axisymmetric UVs at incidence, consider Figure 2.11 representing a two-dimensional fluid domain in a cross-section plane perpendicular to the long axis of an axisymmetric UV at a steady drift angle β. This fluid domain represents the behavior of the streamlines of the fluid particles. In Figure 2.11, ϕ indicates the circumferential location measured from the leading edge.
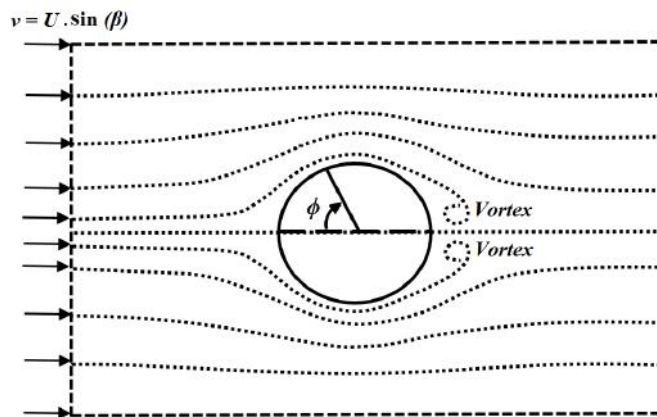
Figure 2.11: A two dimensional fluid domain in a cross-section plane perpendicular to the long axis of an axisymmetric UV at a steady drift angle β

As is well known from the fluid flowing over a two dimensional circular cylinder, a favorable pressure gradient is imposed over the fluid flowing from leading edge toward $\phi = 90°$ (this region is called the windward side). The velocity reaches the highest value at $\phi = 90°$. However, in the region from $\phi = 90°$ toward the trailing edge (this region is called the leeward side) an adverse pressure gradient is imposed over the fluid flow. Accordingly, since the fluid flowing inside the boundary layer is unable to negotiate the resultant adverse circumferential pressure gradient, the flow separates from the body surface. The separation region gives rise to the formation and evolution of a vortical structure on the leeward side. For instance, Figure 2.12 shows the formation of the leeward vortical flow structure arising from the crossflow separation over the totally submerged SUBOFF axisymmetric UV at $\beta = 18.11°$ and $F_n = 0.512$. This figure through representing the vorticity magnitude at several plane sections perpendicular to the long axis of the UV serves well to highlight several important fluid flow characteristics around a UV at steady drift such as the development of the crossflow separation and the formation and evolution of a vortical flow structure over the leeward side.
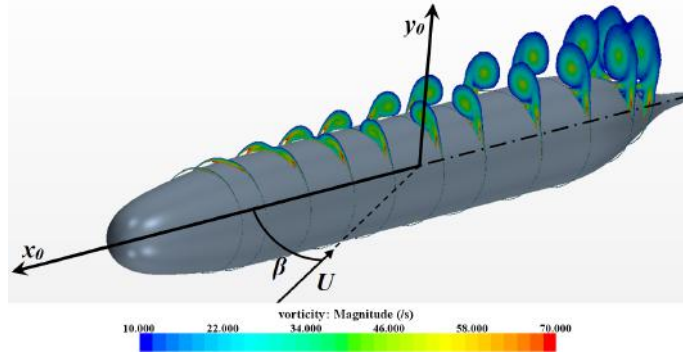
Figure 2.12: Crossflow separation pattern over the totally submerged SUBOFF at $\beta = 18.11°$ and $F_n = 0.512$

As can be inferred from Figure 2.12, the size of the vortical flow structure formed on the leeward side undergoes an increase with an increase in the distance from the UV nose. Additionally, based on CHESNAKAS e SIMPSON [25], PHILLIPS *et al.* [54] and KIM *et al.* [55], the size of this vortical structure also increases with an increase in drift angle, which is attributed to an increase in the lateral velocity component v with respect to drift angle.

At low drift angles ($\beta < 10°$), the separation region in the leeward side is small and located merely at the downstream of body [24]. However, with an increase in drift angle, the separation region moves both forward and windward. For $\beta < 20°$, which brackets the typical operating scenarios for UVs [56], in a totally submerged condition, the leeward vortical structure is steady and symmetric with respect to a plane passing through the leading edge and trailing edge (Figure 2.11) (WETZEL *et al.* [24], CHESNAKAS e SIMPSON [25], PHILLIPS *et al.* [54] and KIM *et al.* [55]).

The significance of the leeward vortical flow structure is its convective property, which gives rise to an increase in the flow velocity in the leeward side. This, consequently, reduces the local dynamic pressure in this region. As a result, the leeward vortical flow structure exerts considerable forces and moments over the UV and, accordingly, is largely responsible for the behavior of the Y-force and N-moment, especially at large lateral velocities.

In this regard, as shown in several experimental and numerical studies such as CHESNAKAS e SIMPSON [25], PHILLIPS *et al.* [54] and KIM *et al.* [55], the correct numerical estimation of the forces and moments acting on an axisymmetric UV at moderate drift relies highly upon the accurate prediction of the crossflow separation and its resultant leeward vortical flow structure. Accordingly, as shown by CHESNAKAS e SIMPSON [25], PHILLIPS *et al.* [54] and KIM *et al.* [55], the utilization of sophisticated turbulence models, which are capable of representing the complex three-dimensional anisotropic fluid flow developed over the axisymmetric

UVs at moderate incidence, is necessary for a correct estimation of the forces and moments acting on the body.

2.2.2 Fluid flow characteristics around a UV undergoing a steady turning motion

When a UV is moving ahead with a linear velocity u and an angular yaw velocity r is imposed on the body, a linear distribution of lateral velocity v is developed along the length of the UV. For instance, Figure 2.13 shows the lateral velocity distribution $v(x_0) = rx_0$ along the length of the SUBOFF UV undergoing a steady turning motion performed in this thesis at an angular yaw velocity $r' = -0.4$ about the z_0 axis. Accordingly, every point along the length of the SUBOFF experiences a specific angle of drift defined as $\beta(x_0) = \tan^{-1}(\frac{-v(x_0)}{u})$ [56].

Moreover, due to the lateral velocity reversal during a steady turning motion, the starboard and port sides of an axisymmetric UV act as a combination of both windward side and leeward side. To further clarify this, consider Figure 2.13. In this case, the starboard side at the fore half part of the SUBOFF is the leeward side, while it becomes the windward side at the aft half part. On the other hand, the portside at the fore half part of the SUBOFF is the windward side while it turns into the leeward side over the aft half part.

Thus, the fluid flow characteristics are different from those in steady drift motion as the flow is subject to the lateral velocity reversal, which imposes different drift angles along the UV length with the largest occurring at the extreme end of the stern.
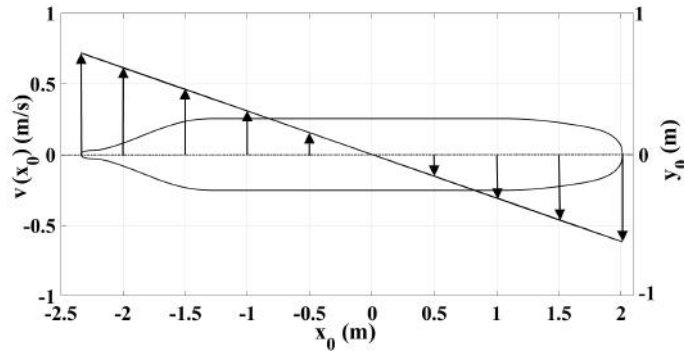
Figure 2.13: Lateral velocity distribution $v(x_0)$ along the length of the SUBOFF UV undergoing a steady turning motion with an angular yaw velocity $r' = -0.4$ about the z_0 axis

2.3 Computational fluid dynamics

As mentioned in section 2.1, to evaluate the free surface effect on the hydrodynamics and dynamics of a generic UV, the hydrodynamic captive tests, as explained in section 2.1.3, are performed for various submergence depths and proper ranges of UV velocity components. To perform these hydrodynamic tests, computational fluid dynamics (CFD) is used. Herein, the numerical simulations of hydrodynamic tests are carried out in the commercial code STARCCM+ [37]. Accordingly, this section presents the methodology related to the CFD approach used in this thesis.

2.3.1 General governing equations

Incompressible fluid motion is governed by the Navier-Stokes and continuity equations. The Navier-Stokes equations for a Newtonian flow in an arbitrary control volume Ω, which is bounded by the control surface S, is written as follows [37]:

$$\frac{\partial}{\partial t} \int_\Omega \rho \overrightarrow{V} d\Omega + \oint_S \rho \overrightarrow{V} (\overrightarrow{V}.d\overrightarrow{S}) - \oint_S \tau.d\overrightarrow{S} + \oint_S pI.d\overrightarrow{S} = \int_\Omega \rho \overrightarrow{f_e} d\Omega. \qquad (2.56)$$

The first term on the left hand side shows the rate of variation of the momentum within the volume Ω. The term $\rho \overrightarrow{V} (\overrightarrow{V}.d\overrightarrow{S})$ is the convection per unit volume through the control surface S. The term pI represents the isotropic pressure component and τ is the tensor of viscous shear stress, which is estimated as:

$$\tau = 2\mu E, \qquad (2.57)$$

where E indicates the deformation tensor, whose components are:

$$E = \frac{1}{2} (\frac{\partial u_i}{\partial x_j} + \frac{\partial u_j}{\partial x_i}). \qquad (2.58)$$

Finally, $\rho \overrightarrow{f_e}$ indicates the body forces, which can be due to gravity and/or rotation. In this regard, in the present study, to conduct the rotating arm tests explained in section 2.1.3, a rotating coordinate system is adopted. Accordingly, due to computation in a rotating reference frame, the Coriolis $(-\rho \left(2\overrightarrow{\omega} \times \overrightarrow{V}\right))$ and centrifugal $(-\rho \left(\overrightarrow{\omega} \times \left(\overrightarrow{\omega} \times \overrightarrow{\Delta r}\right)\right))$ forces are added to the momentum equations as source terms as follows [37]:

$$\rho \overrightarrow{f_e} = -\rho \left(2\overrightarrow{\omega} \times \overrightarrow{V}\right) - \rho \left(\overrightarrow{\omega} \times \left(\overrightarrow{\omega} \times \overrightarrow{\Delta r}\right)\right), \qquad (2.59)$$

where $\overrightarrow{\omega}$ indicates the angular velocity and $\overrightarrow{\Delta r}$ the rotation radius.

Additionally, the continuity equation, which states that within a fluid system the mass is not disappeared or created, for the same control volume Ω is written as follows:

$$\frac{\partial}{\partial t} \int_\Omega \rho d\Omega + \oint_S \rho \vec{\mathbf{V}}.d\vec{S} = 0. \tag{2.60}$$

The above forms of representation of Navier-Stokes and continuity equations are the integral form of the conservation of momentum and mass, respectively.

2.3.2 Level of representation of reality

In order to solve the Navier-Stokes equations three main methods exist as follows [57]:

- Direct Numerical Simulation (DNS)

- Large Eddy Simulation (LES)

- Unsteady Reynolds Averaged Navier-Stokes equations (URANS)

In DNS method, the Navier-Stokes equations are directly solved without using any turbulence model. Hence, by using proper computational grids the whole range of spatial and temporal turbulence scales are resolved. Accordingly, it can be shown that the memory storage demand in a DNS grows very fast with Reynolds number. Considering the computational resources available, utilization of DNS is not practicable.

Therefore, to reduce the computational cost of DNS, LES resolves large scales of the turbulence and models the smaller scale ones, rather than resolving them as DNS does. However, considering the computational resources, it is not still attainable to use this method, neither.

On the other hand, URANS, which uses the averaging concept introduced by Reynolds (1895), is currently the most common method used to approximate the Navier-Stokes equations. Additionally, the average values of the forces, moments and fluid flow characteristics suffice to fulfill the main objective of the present research. Thus, it is decided to utilize a URANS solver to fulfill the main purpose of the current research.

In URANS, all the properties of the fluid flow are expressed as the sum of a mean and a fluctuating part. Accordingly, the instantaneous value of any quantity ϕ is written as the sum of a time-averaged part, $\overline{\phi}$, and a part showing the fluctuations about the average value, ϕ':

$$\phi = \overline{\phi} + \phi', \tag{2.61}$$

where the average value $\overline{\phi}$ is obtained as follows:

$$\overline{\phi} = \frac{1}{T} \int_0^T \phi(\overrightarrow{x}, t) dt. \tag{2.62}$$

Note that in practice the period T for averaging should be very large compared to the time scale of the turbulent fluctuations and at the same time for unsteady (non-stationary) fluid flows, it should be less than the time scale of the variations of the mean flow.

After the averaging process is introduced into the governing equations, the continuity equation becomes:

$$\frac{\partial}{\partial t} \int_\Omega \rho d\Omega + \oint_S \rho \overrightarrow{\overline{V}}.d\overrightarrow{S} = 0. \tag{2.63}$$

Furthermore, the Navier-Stokes equations take the following form:

$$\frac{\partial}{\partial t} \int_\Omega \rho \overrightarrow{\overline{V}} d\Omega + \oint_S \rho \overrightarrow{\overline{V}} (\overrightarrow{\overline{V}}.d\overrightarrow{S}) - \oint_S (\overline{\tau_V} + \overline{\tau_R}).d\overrightarrow{S} + \oint_S \overline{p}I.d\overrightarrow{S} = \int_\Omega \rho \overrightarrow{f_e} d\Omega, \tag{2.64}$$

where $\overline{\tau_V}$ indicates the tensor of average viscous shear stress and $\overline{\tau_R}$ is the Reynolds stress tensor [37]. The Reynolds stress tensor, which appears in the momentum equation due to the averaging process, is symmetric and therefore, there are six unknown components that must be calculated. Interestingly, along with the three unknown velocity components and the pressure, there are ten unknowns and only four equations. Accordingly, to close this problem, various turbulence models have been proposed to model the Reynolds stresses.

2.3.3 Selection of turbulence model

The selection of turbulence model can affect the accuracy of CFD results. In this regard, there are two main types of turbulence models: turbulence models based on the isotropic turbulent eddy viscosity assumption, which is first introduced by Joseph Boussinesq (1877), and anisotropic Reynolds stress turbulence models.

In the eddy viscosity models, which may be algebraic or have one or two differential equations such as $k - \varepsilon$ and $k - \omega$ models, the Reynolds stresses $\overline{u_i' u_j'}$ are coupled to the gradients of the mean velocity $(\frac{\partial \overline{u}_i}{\partial x_j} + \frac{\partial \overline{u}_j}{\partial x_i})$ through an eddy viscosity (μ_t) as follows:

$$-\rho \overline{u_i' u_j'} = \mu_t (\frac{\partial \overline{u}_i}{\partial x_j} + \frac{\partial \overline{u}_j}{\partial x_i}). \tag{2.65}$$

Therefore, the Reynolds stress tensor is treated in the same manner as the viscous

stress tensor, where the viscous stresses are coupled to the mean deformation rate of the flow (gradients of the average velocities) by using the isotropic dynamic viscosity of the fluid μ (Equation 2.57). In other words, the Reynolds stresses are considered aligned with the deformation rate of the flow. More precisely, it is assumed that the angles of turbulent shear stress γ_τ:

$$\gamma_\tau = \text{atan}\left(\frac{\overline{u_2' u_3'}}{\overline{u_1' u_2'}}\right) \qquad (2.66)$$

and the flow gradient γ_g:

$$\gamma_g = \text{atan}\left(\frac{\frac{\partial \overline{u}_2}{\partial x_3} + \frac{\partial \overline{u}_3}{\partial x_2}}{\frac{\partial \overline{u}_1}{\partial x_2} + \frac{\partial \overline{u}_2}{\partial x_1}}\right) \qquad (2.67)$$

are equal, CHESNAKAS e SIMPSON [25]. However, as mentioned in section 2.2.1, several experimental and numerical studies such as CHESNAKAS e SIMPSON [25], PHILLIPS *et al.* [54], KIM *et al.* [55] and HOLLOWAY *et al.* [58] demonstrate that the eddy viscosity models are inadequate for the simulations of the fluid flow around the axisymmetric bodies at incidence. In this regard, CHESNAKAS e SIMPSON [25], PHILLIPS *et al.* [54], KIM *et al.* [55] and HOLLOWAY *et al.* [58] show that the eddy viscosity models are incapable of representing adequately the complex three dimensional anisotropic fluid flow developed over the axisymmetric UVs at incidence. Later in Appendix B, it is also demonstrated that the eddy viscosity models are inadequate for axisymmetric bodies at zero incidence, either.

Therefore, it is necessary to employ the Reynolds stress turbulence (RST) models to account for the anisotropy of the flow encountered in this research to avoid erroneous prediction of fluid properties. Since, as mentioned earlier in section 2.2.1, the correct prediction of the forces and moments acting on the axisymmetric UVs at incidence relies largely upon the accurate prediction of the fluid flow characteristics developed around the body. The RST model is the most sophisticated turbulence model. The RST, by discarding the isotropic eddy-viscosity assumption, closes the URANS equations by solving transport equations for each six component of Reynolds stress tensor, together with an equation for the dissipation rate.

The transport equation for each Reynolds stress term ($R_{ij} = \overline{u_i' u_j'}$) is written as follows [37]:

$$\frac{\partial}{\partial t} \int_\Omega \rho R_{ij} d\Omega + \oint_S \rho R_{ij}(\overrightarrow{\mathbf{V}}.d\overrightarrow{S}) - \oint_S D_{ij}.d\overrightarrow{S} = \int_\Omega (P_{ij} - \frac{2}{3}\rho\varepsilon\mathbf{I} + \Pi_{ij})d\Omega. \quad (2.68)$$

The terms appear in this equation are defined as follows:

- D is the Reynolds-stress diffusion and is modeled by assuming that the rate

of transport of Reynolds stresses through diffusion is proportional to the gradients of the Reynolds stress terms. Accordingly, it is obtained as:

$$D_{ij} = (\mu + \frac{\mu_t}{\sigma_k})\nabla R_{ij}, \tag{2.69}$$

where $\sigma_k = 0.82$ and the isotropic turbulent eddy viscosity μ_t is calculated as:

$$\mu_t = \rho C_\mu \frac{k^2}{\varepsilon}, \tag{2.70}$$

where $C_\mu = 0.099$.

- k is the kinetic energy of the turbulence and is calculated by adding the three normal Reynolds stresses $(i = j)$:

$$k = \frac{1}{2}tr(R). \tag{2.71}$$

- P_{ij} is turbulent production due to mean flow deformation and is obtained as follows by retaining this term in its exact form:

$$P_{ij} = -\rho(R_{im}\frac{\partial \overline{u}_j}{\partial x_m} + R_{jm}\frac{\partial \overline{u}_i}{\partial x_m}). \tag{2.72}$$

- Π_{ij} indicates the turbulent pressure-strain interaction. In this regard, as pointed out by VERSTEEG e MALALASEKERA [38], the turbulent pressure-strain interaction although is the most difficult term in the transport equations of Reynolds stresses to model, it is substantially important to be modeled correctly. This term takes into account the fluctuations in pressure due to two types of interactions: first the interactions between two eddies and second the interaction between an eddy and a fluid flow having a different mean velocity. The pressure strain term has a role to make the normal stresses $(i = j)$ more isotropic by redistributing the turbulent kinetic energy over the three normal stresses and reducing the shear stresses $(i \neq j)$. This term in STARCCM+ is based on the work conducted by SPEZIALE *et al.* [59], and is modeled as follows:

$$\begin{aligned}
\Pi_{ij} = &- \left[C_{s1}\rho\varepsilon + C_{r4}tr(P)\right]A_{ij} \\
&+ C_{s2}\rho\varepsilon\left(A_{ik}A_{kj} - \frac{1}{3}A_{mn}A_{mn}\delta_{ij}\right) + \\
&\left(C_{r3} - C_{r3}^*\sqrt{A_{ij}A_{ij}}\right)\rho k E_{ij} + \\
&C_{r1}\rho k\left(A_{ik}E_{jk} + E_{ik}A_{jk} - \frac{2}{3}A_{mn}E_{mn}\delta_{ij}\right) + C_{r2}\rho k\left(A_{ik}W_{jk} + W_{ik}A_{jk}\right),
\end{aligned} \tag{2.73}$$

where the anisotropy tensor A, is defined as follows:

$$A_{ij} = \frac{R_{ij}}{k} - \frac{2}{3}\mathbf{I}, \tag{2.74}$$

where $\mathbf{I}$ is the identity matrix. Additionally, δ_{ij} is the delta Kronecker function. Moreover, W is the tensor of rotation:

$$W_{ij} = \frac{1}{2}(\frac{\partial \overline{u}_i}{\partial x_j} - \frac{\partial \overline{u}_j}{\partial x_i}). \tag{2.75}$$

In addition, the coefficients have the following values:

$$
\begin{aligned}
&C_{s1} = 1.7, C_{s2} = 1.05, \\
&C_{r1} = 1.25, C_{r2} = 0.2, C_{r3} = 0.8, \\
&C_{r3}^* = 0.65, C_{r4} = 0.9.
\end{aligned}
\tag{2.76}
$$

- ε is the dissipation rate of the turbulent kinetic energy. To model this term, it is assumed that only the normal Reynolds stresses $(i = j)$ are affected equally by the dissipation rate. Hence, it is obtained from a transport equation similar to that of the standard $k - \varepsilon$ model:

$$
\begin{aligned}
&\frac{\partial}{\partial t} \int_{\Omega} \rho\varepsilon d\Omega + \oint_S \rho\varepsilon(\overrightarrow{\mathbf{V}}.d\overrightarrow{S}) - \oint_S (\mu + \frac{\mu_t}{\sigma_k})\nabla\varepsilon.d\overrightarrow{S} \\
&= \int_{\Omega} (\frac{\varepsilon}{k}\left[C_{\varepsilon 1}\left(\frac{1}{2}tr(P)\right) - C_{\varepsilon 2}\rho\varepsilon\right] d\Omega.
\end{aligned}
\tag{2.77}
$$

The coefficients are considered the same as those in the standard $k - \varepsilon$ model as follows:

$$C_{\varepsilon 1} = 1.44, C_{\varepsilon 2} = 1.83. \tag{2.78}$$

Near wall treatment

To formulate the wall treatment, the following dimensionless parameters are used:

$$Y^+ = \frac{yu^*}{\vartheta}, \tag{2.79}$$

$$u^+ = \frac{v_p}{u^*}, \tag{2.80}$$

where y indicates the distance from the wall to the centroid of the cell next to the wall, u^* is the reference velocity, ϑ is the kinematic viscosity, and v_p is the component of the velocity parallel to wall.

Turbulence models use two common approaches to capture the boundary layer near the surface of a body. The first approach is using a very fine mesh with a high resolution to resolve the fluid characteristics within this region, and the second one is using a coarser mesh to employ the standard wall function in this region.

For simulations without wall function, a target Y^+ of five or less is desirable, while the target Y^+ range for using the wall function is typically from 30 to 100. In other words, to use wall function the cell next to the wall should lay within the logarithmic region of the boundary layer.

In the present research, the RST model uses the standard wall function to represent near-wall turbulence. For this purpose, therefore, a range of Y^+ from 30 to 100 is favorable. In this range of Y^+, the reference velocity u^*, which is related to the wall shear stress through $u^* = \sqrt{\frac{\tau_w}{\rho}}$, is calculated as:

$$u^* = \sqrt{(C_\mu)^{\frac{1}{2}} k}. \tag{2.81}$$

In addition, the velocity of the cell next to the wall is obtained as:

$$u^+ = \frac{1}{0.42} \ln(9 Y^+). \tag{2.82}$$

Furthermore, the dissipation of the turbulent kinetic energy is estimated as:

$$\varepsilon = \frac{(u^*)^3}{\mathrm{k} y}, \tag{2.83}$$

where k is the Von Karman constant, which is equal to 0.42.

The main advantage of using the wall function is the elimination of iterative convergence problems and the excessive calculation time, as mentioned by EÇA *et al.* [60]. Additionally, KIM *et al.* [55] have shown a good performance of RST models in conjunction with wall function in capturing the crossflow features of a 6 : 1 prolate-spheroid at moderate incidence.

2.3.4   Modeling the free surface

The free surface exists between two immiscible flow phases, namely water and air, which originates from the large difference in the densities of the flow phases. Due to this difference in densities, the inertia of the air can generally be ignored in comparison with water.

Thus modeling a free and moving surface brings some serious complications. Especial approaches are required to define its properties along with the effect that it introduces in flow.

On the free surface two conditions exist: the kinematic and the dynamic conditions [61]. The kinematic condition considers that the particles of fluid never leave

the free surface. In addition, the dynamic free surface condition states that the pressure at free surface is constant and is equal to the atmospheric pressure. In this respect, there are two main approaches to impose these conditions in CFD, interface tracking and interface capturing methods [62].

Interface tracking methods, which is also called the Lagrangian grid methods, uses a Lagrangian grid to define the free surface as an interface and follows its evolution over time. Therefore, the free surface is regarded as a boundary and then the kinematic and dynamic conditions are imposed directly upon this boundary.

However, where large amplitude surface motions exists the interface tracking methods have difficulty to track the free surface without introducing remeshing techniques with respect to the new position of free surface. The remeshing process signifies that the field values from the old mesh must be projected to the new one. This is computationally costly and can be a source for errors.

On the other hand, the interface capturing methods capture a volume inside a fixed domain, which contains the free surface. The volume of fluid (VOF) approach, which is one the interface capturing methods, requires reasonable computational resources and is robust enough to handle the problems such as breaking waves, droplets, and bubbles.

STARCCM+ uses the VOF method for handling the simulations with free surface [37, 39]. The VOF uses the fraction of the cell occupied by water (α_i) to locate the free surface. This fraction is calculated by solving the following transport equation for α_i:

$$\frac{\partial}{\partial t} \int_\Omega \alpha_i d\Omega + \oint_S \alpha_i \overrightarrow{\mathbf{V}}.d\overrightarrow{S} = 0. \tag{2.84}$$

In this regard, the value of α_i equal to one indicates the cells filled with water, equal to zero indicates the cells filled with air, and cells where the value of α_i lays in a range from zero to one contain the free surface.

In this approach, both air and water phases are treated as a single phase that share velocity and pressure fields, while their properties (density and viscosity) vary according to α_i as follows:

$$\rho = \sum_i \rho_i \alpha_i, \mu = \sum_i \mu_i \alpha_i, \tag{2.85}$$

where ρ_i and μ_i denote the density and viscosity of the $i-$th phase.

To acquire a sharp interface, some special cares must be taken to discretize the convection term in Equation 2.84, since the value of α_i must be bounded in a range from zero to one. In this regard, using the low order schemes such as the first-order upwind scheme though fulfill the boundedness criterion, cause the surface to become overly diffusive. While the higher order schemes, such as the second-order central

43

differencing, cause the α_i to take values that are physically impossible since they violate the requirement of boundedness.

To obtain a sharp interface, STARCCM+ uses the High Resolution Interface Capturing (HRIC) scheme [63], which is based on the normalized variable diagram proposed by LEONARD [64], to discretize the convective term. In this scheme, first, the normalized value of the volume fraction in a cell, say C represented in Figure 2.14, is defined based on the volume fraction values in cells U and D, as follows:

$$\zeta_C = \frac{\alpha_C - \alpha_U}{\alpha_D - \alpha_U}. \tag{2.86}$$

Similarly, the normalized face value is defined as:

$$\zeta_f = \frac{\alpha_f - \alpha_U}{\alpha_D - \alpha_U}. \tag{2.87}$$
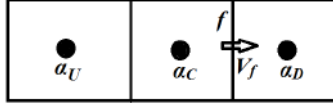
Figure 2.14: Volume fractions in central (C), upwind (U) and downwind (D) cells

Accordingly, to avoid non-physical oscillations arising from the locally un-bounded α_C and consequently α_f in the entire solution domain, the normalized face value is estimated as follows based on the normalized cell value:

$$\zeta_f = \begin{cases} \zeta_C, & \text{if } \zeta_C < 0 \\ 2\zeta_C, & \text{if } 0 \leq \zeta_C \leq 0.5 \\ 1, & \text{if } 0.5 \leq \zeta_C \leq 1 \\ \zeta_C, & \text{if } 1 < \zeta_C \end{cases} \tag{2.88}$$

The value of ζ_f is then corrected based on the local Courant number (C_u) to account for the availability criterion, which states that in a time step the quantity of a fluid convecting through a face is less than or equal to the quantity of the fluid available in the donor cell, as follows:

$$\zeta_f^* = \begin{cases} \zeta_f, & \text{if } C_u < C_{uL} \\ \zeta_C + (\zeta_f - \zeta_C)\frac{C_{uU}-C_u}{C_{uU}-C_{uL}}, & \text{if } C_{uL} \leq C_u \leq C_{uU} \\ \zeta_C, & \text{if } C_{uU} < C_u \end{cases} \tag{2.89}$$

where, C_{uL} and C_{uU} are user-adjustable parameters to control the blending of HRIC and the first-order upwind method. Therefore, based on this equation, where the Courant number is less than C_{uL} HRIC is used, and where the Courant number is in

the range between $C_{uL} < C_u < C_{uU}$ a combination of HRIC and upwind methods is employed, and finally where the Courant number is larger than C_{uU} only the upwind method is used.

For problems with a steady state solution, in order to take advantage of the features of HRIC scheme, it is recommended by STARCCM+ [37] to specify these limits (C_{uL} and C_{uU}), values higher than the Courant number encountered in the simulation. SPENCE [65] reported an improvement in the simulation results, by increasing C_{uL} and C_{uU}. Accordingly, to use the HRIC method in the present study, values of 5 and 5.5 are assigned to C_{uL} and C_{uU}, which are well above the Courant numbers encountered in the simulations.

The final correction is introduced into the normalized face value ζ_f in accordance with the angle θ enclosed by the vector normal to the interface (, which is defined as the gradient of the volume fraction $\nabla \alpha_i$,) and the vector normal to the surface of the cell face as follows:

$$\zeta_f^{**} = \zeta_f^*(\cos\theta)^{C_\theta} + \zeta_C(1 - (\cos\theta)^{C_\theta}), \tag{2.90}$$

where C_θ (angle factor) is a user-adjustable parameter with a default value of 0.05. This value should be increased for simulations where the free surface does not follow the grid lines. Herein, the default value of the angle factor is used. Note that the reason to use this last correction is to prevent the alignment of the interface with the numerical grid [63]. Finally, the value of α_f on the face is calculated as:

$$\alpha_f^{HRIC} = \zeta_f^{**}(\alpha_D - \alpha_U) + \alpha_U. \tag{2.91}$$

2.3.5 Discretization of the governing equations

After spatial discretization, the equations governing the physical problem, 2.63 and 2.64, are discretized. STARCCM+ uses the Finite Volume Method (FVM) to discretize directly the integral form of the governing equations over the finite volumes representing the discretized form of the computational domain [37]. An immediate advantage of the FVM is the assurance of the conservation of the basic flow quantities for each finite volume, by using the integral form of conservation laws [38].

In this section, the procedure used by STARCCM+ [37] to discretize the continuity and the momentum equations is presented. Additionally, the discretized form of each term in the momentum equation including the transient term, the convection term, diffusion term and pressure term is presented.

Continuity Equation

The continuity equation in the discretized form is written as follows:

$$\sum_f \dot{m}_f = \sum_f (\dot{m}_f^* + \dot{m}_f') = 0, \tag{2.92}$$

where f stands for face, $\dot{m}_f$ is the mass rate in cell face, $\dot{m}_f^*$ is the uncorrected mass rate (which is calculated by using the velocities obtained from solving the discretized form of momentum equation with velocity and pressure values specified from the initial or previous iteration) and $\dot{m}_f'$ is the mass rate correction. As is well known from VERSTEEG e MALALASEKERA [38] and FERZIGER e PERIC [57], the continuity equation is normally used to obtained an equation for pressure correction, which is used to update the velocity and pressure fields. In this regard, the value of $\dot{m}_f^*$ for an interior face is estimated in terms of the cell variables as follows:

$$\dot{m}_f^* = \rho \left(\frac{\vec{\mathbf{V}}_0^* + \vec{\mathbf{V}}_1^*}{2} \right) . \vec{S} - Q_f (p_0^* - p_1^* - \overline{\nabla p_f^*} . \Delta \vec{x}), \tag{2.93}$$

where $\vec{\mathbf{V}}_0^*$ and $\vec{\mathbf{V}}_1^*$ are the velocities of the cell 0 and 1 that are obtained from solving the discretized form of momentum equation with velocity and pressure values specified from the initial or previous iteration. p_0^* and p_1^* indicate the pressure values of the cell 0 and 1, respectively, at initial or previous iteration. The second term on the right hand side of Equation 2.93 is called the Rhie-and-Chow dissipation at the face. The term $\overline{\nabla p_f^*}$ is the average of the cell pressure gradients calculated using a volume-weighted averaging interpolation scheme between the gradient values of the cell 0 and 1. This term is especially important in non-orthogonal grids where the angle between the cell face normal and the line connecting the centers of cell 0 and 1 on either side of the face f is nonzero. Additionally, $\Delta \vec{x} = \vec{x}_1 - \vec{x}_0$, with $\vec{x}_1$ and $\vec{x}_0$ being the position vector of cell 0 and 1, respectively, indicates the vector connecting two cells 0 and 1 centroids. Furthermore, the parameter Q_f is calculated as follows:

$$Q_f = \rho \left(\frac{\Omega_0}{\bar{a}_0} + \frac{\Omega_1}{\bar{a}_1} \right) \vec{\alpha} . \vec{S}, \tag{2.94}$$

where Ω_0, Ω_1 imply the volume, and $\bar{a}_0$, $\bar{a}_1$ the average of the coefficients of the discretized momentum equations of finite volume controls 0 and 1, respectively. The parameter $\vec{\alpha}$ is the face metric quantity and is calculated as:

$$\vec{\alpha} = \frac{\vec{S}}{\vec{S} . \Delta \vec{x}}. \tag{2.95}$$

After calculation of $\dot{m}_f^*$, the mass rate correction $\dot{m}_f'$ is estimated from an equation similar to that proposed by VERSTEEG e MALALASEKERA [38] for the calculation of the mass rate correction as follows:

$$\dot{m}_f' = Q_f(p_0' - p_1').$$

(2.96)

Substituting equation 2.96 into equation 2.92 provides a system of equations to obtain the pressure correction terms p_0' and p_1' as follows:

$$a_p p_p' + \sum_n a_n p_n' = \sum_f \dot{m}_f^*.$$

(2.97)

From the above system of equations with linear coefficients, a_p and a_n, the unknown pressure correction terms p' are obtained; consequently, this pressure correction is used to calculate the mass rate correction $\dot{m}_f'$ and mass rate $\dot{m}_f$ from Equations 2.96 and 2.92, respectively.

Momentum equation

The discretized form of the Navier-Stokes equations without the presence of the external forces is written as follows:

$$\frac{\partial}{\partial t}(\rho \overrightarrow{\mathbf{V}} \Omega)_0 + \sum_f \left[\rho \overrightarrow{\mathbf{V}}(\overrightarrow{\mathbf{V}}.\overrightarrow{S}) \right]_f = \sum_f \tau.\overrightarrow{S} - \sum_f \left(pI.\overrightarrow{S} \right)_f.$$

(2.98)

The first term on the left hand side is the transient term; the second term is the convection term. Additionally, on the right hand side, the first term indicates the diffusion term, while the second one is the pressure term. The discretization procedure for each term is outlined as follows:

- Transient term:

This term is only included in time-dependent simulations, i.e., simulations with the presence of the free surface. Note that, in the present thesis, the simulations in which the UV is totally submerged are performed as steady. In this regard, in case of the simulations with the presence of free surface, a first-order implicit scheme, also called the Euler Implicit, is used to discretize the transient term as follows:

$$\frac{\partial}{\partial t}(\rho \overrightarrow{\mathbf{V}} \Omega)_0 = \rho \frac{\overrightarrow{\mathbf{V}}^{n+1} - \overrightarrow{\mathbf{V}}^n}{\Delta t} \Omega_0,$$

(2.99)

where $n+1$ indicates the solution at the current time step, and n the solution at the previous time step.

- Convection term:

For a general scalar quantity ϕ, the convection term is discretized as follows:

$$\left[\rho\phi\left(\vec{\mathbf{V}}.\vec{S}\right)\right] = \dot{m}_f\phi_f, \tag{2.100}$$

where ϕ_f and $\dot{m}_f$ are the value of the scalar quantity ϕ and the mass rate at the cell face, respectively. To calculate ϕ_f a second-order upwind method is utilized as:

$$\dot{m}_f\phi_f = \begin{cases} \dot{m}_f\left[\phi_0 + (\vec{x}_f - \vec{x}_0).\vec{\nabla}\phi_{r,0}\right], & \text{if } \dot{m}_f^* \geq 0 \\ \dot{m}_f\left[\phi_1 + (\vec{x}_f - \vec{x}_1).\vec{\nabla}\phi_{r,1}\right], & \text{if } \dot{m}_f^* < 0 \end{cases} \tag{2.101}$$

where ϕ_0 and ϕ_1 are the values of the scalar quantity ϕ at cell-0 and cell-1. The value $(\vec{x}_f - \vec{x}_0).\vec{\nabla}\phi_{r,0}$ and $(\vec{x}_f - \vec{x}_1).\vec{\nabla}\phi_{r,1}$ are the linear interpolations of the values of the scalar quantity ϕ at cell centroids to the mutual face of these cells. The terms $\vec{\nabla}\phi_{r,0}$ and $\vec{\nabla}\phi_{r,1}$ are the limited reconstruction gradients in cell-0 and cell-1, respectively. In Equation 2.101 it is assumed that the centroids of cells 0 and 1 lie on opposing sides of the face f.

- Pressure evaluation at faces:

The pressure at each face is estimated based on the interpolated pressure values p_{f0} and p_{f1} from cell-0 and cell-1, as follows:

$$p_f = \frac{\bar{a}_0 p_{f0} + \bar{a}_1 p_{f1}}{\bar{a}_0 + \bar{a}_1}, \tag{2.102}$$

where $\bar{a}_0$, $\bar{a}_1$ are the average of the coefficients of the discretized momentum equations of finite volume controls 0 and 1, respectively. Note that p_{f0} and p_{f1} are interpolated from cell-0 and cell-1 using the limited reconstruction gradients $\vec{\nabla}p_{r,0}$ and $\vec{\nabla}p_{r,1}$ as follows:

$$p_{f0} = p_0 + (\vec{x}_f - \vec{x}_0).\vec{\nabla}p_{r,0}, \tag{2.103}$$

$$p_{f1} = p_1 + (\vec{x}_f - \vec{x}_1).\vec{\nabla}p_{r,1}. \tag{2.104}$$

- Diffusion term:

For a general scalar quantity ϕ, the diffusion term is written as $\Gamma\vec{\nabla}\phi.\vec{S}$, where Γ indicates the diffusivity. To obtain a second-order expression for diffusion value at an interior face f in terms of cell values ϕ_1 and ϕ_0, the following second-order scheme is used:

$$\Gamma_f \overrightarrow{\nabla}\phi_f . \overrightarrow{S} =$$

$$\Gamma_f \left[(\phi_1 - \phi_0)\, \overrightarrow{\alpha}.\overrightarrow{S} + \left(\frac{\overrightarrow{\nabla}\phi_0 + \overrightarrow{\nabla}\phi_1}{2} \right).\overrightarrow{S} - \left(\left(\frac{\overrightarrow{\nabla}\phi_0 + \overrightarrow{\nabla}\phi_1}{2} \right).\Delta\overrightarrow{x} \right) \overrightarrow{\alpha}.\overrightarrow{S} \right],$$

$$(2.105)$$

where $\Delta\overrightarrow{x} = \overrightarrow{x}_1 - \overrightarrow{x_0}$ with $\overrightarrow{x}_1$ and $\overrightarrow{x_0}$ being the position vector of cell 1 and 0, respectively, indicates the vector connecting two cells 0 and 1 centroids. In Equation 2.105 it is assumed that the centroids of cells 0 and 1 lie on opposing sides of the face f. Note that the second and third terms on the right hand side of Equation 2.105 are the secondary gradients, which are essential especially in non-orthogonal grids.

Calculation of gradients

When using FVM on an unstructured grid, especial attention must be paid to calculate the spatial derivatives (gradients). Calculation of gradients, which is called the gradient reconstruction, consists of approximating the gradient vectors attributed to the control volumes using a finite set of discrete scalar values. In STARCCM+ the gradients are used in the following places:

- To calculate the reconstructed field values at faces

- To calculate the diffusion terms

- Pressure gradients

- In turbulence models to calculate the strain and rotation rates

STARCCM+ uses two main steps to calculate the gradients:

1. In the first step, the unlimited reconstruction gradients are calculated. The unlimited refers to the calculations of reconstruction gradients, where the availability criteria is not accounted for. In other words, the variables on faces can exceed the values of the cells in vicinity.

2. The second step is limiting the reconstruction gradients calculated in the first step. In this step, in order for the reconstructed face values not to fall outside the range of the values in neighboring cells, the reconstruction gradients are limited based on the minimum and maximum values found in the neighboring cells. These limited reconstruction gradients are employed for the estimation of the scalar values on faces, which are used to calculate flux integrals.

In the present work, a hybrid Gauss Least-Square method is employed for the purpose of calculation of reconstruction gradients.

2.3.6 Multiphase segregated flow solver

A multiphase segregated flow solver is used to control the overall solution. The multiphase refers to the phases involved in the simulations, whose shares of the computational domain are determined by the volume fraction (Equation 2.85). Additionally, in the numerical simulations, a colocated variable arrangement proposed by RHIE e CHOW [66] is used. Note that the segregated solver is another name for a SIMPLE-type solver for pressure-velocity coupling, STARCCM+ [37]. The SIMPLE algorithm, which controls the overall solution, can be described briefly as follows:

1. The velocity and pressure fields are specified from initial or previous iteration. Also, the boundary conditions are imposed.

2. The reconstruction gradients of pressure and velocity fields are computed.

3. The pressure and velocity gradients are limited.

4. Through solving the discretized form of momentum equation (Equation 2.98) the intermediate velocity field $\overrightarrow{\mathbf{V}}^*$ is obtained.

5. The uncorrected mass rate $\dot{m}_f^*$ is computed from Equation 2.93.

6. The pressure correction equation (Equation 2.97) is solved to provide the cell values of the pressure correction p'.

7. The pressure field is updated through $p^{n+1} = p^n + 0.3p'$, where, 0.3 is the under-relaxation factor for pressure.

8. The mass rates on faces are updated through $\dot{m}_f^{n+1} = \dot{m}_f^* + \dot{m}_f'$.

9. The velocity is corrected through $\overrightarrow{\mathbf{V}}^{n+1} = \overrightarrow{\mathbf{V}}^* - \frac{\Omega \nabla p'}{\overrightarrow{a}_p^\Omega}$ where $\nabla p'$ is the gradient of the pressure corrections and $\overrightarrow{a}_p^\Omega$ is the vector of central coefficients of the discrete linear system of equations expressing the velocity.

10. Set $\overrightarrow{\mathbf{V}}^* = \overrightarrow{\mathbf{V}}$ and $p^* = p$.

2.3.7 Solution to the algebraic system of equations

The result of the discretization of the governing equations is a set of linear algebraic equations as follows:

$$Ax = B, \tag{2.106}$$

where the matrix A represents the coefficients of the linear system, the vector x is the unknowns and the vector B represents the boundary and initial conditions along with the source terms. Since most of the elements in matrix A are zero this matrix is typically a sparse matrix. Using direct methods, such as Gauss elimination can be costly, especially on large grids. Therefore, STARCCM+ uses an iterative method called the algebraic multigrid (AMG) method to solve this set of linear algebraic equations [37]. This method has three major steps as follows:

1. Gathers the cells together in the fine grid to form a coarser grid level. The reason for this is the faster convergence of the Gauss-Seidel's method on coarse grids. The coarse-grid equations are obtained from the arithmetic combinations of the fine-grid coefficients.

2. The B matrix is transferred from the fine-grid level to the coarse-grid level.

3. The corrections are transferred back to the fine-grid level from the coarse-grid level.

The main reason to use the AMG method is only to speed the convergence of the Gauss-seidel's iterative method. More information about this approach can be found in STARCCM+ [37].

Generally, in iterative methods, a better approximation (x^{k+1}) of the exact solution x, at the iteration $k + 1$ is sought from the solution in previous iteration k, x^k. The error at the iteration k is defined as:

$$e^k = x - x^k. \tag{2.107}$$

Additionally, the residual can be defined as:

$$r^k = B - Ax^k. \tag{2.108}$$

Multiplying both sides of Equation 2.107 by matrix A results in:

$$Ae^k = Ax - Ax^k. \tag{2.109}$$

Equation 2.109 can be rewritten as:

$$Ae^k = B - Ax^k = r^k. \tag{2.110}$$

Accordingly, the iterations are continued to drive the residual to a small value, which is equivalent to drive the error to a small and negligible value.

In the present work, it is assumed that the convergence of the simulations achieve once the mean values of the forces and moments converge to nearly-constant values with oscillations of less than 2%-3% of the mean values. Accordingly, the convergence of the simulations without the presence of the free surface achieve approximately after 1400 iterations. At the same time the root mean square of the absolute residuals drop to values less than 10^{-4}. Furthermore, the simulations with the presence of the free surface converge approximately within 25 seconds simulation time and at the same time the root mean square of the absolute residuals drop to values less than 10^{-3}. Additionally, the number of inner iterations is considered as 5, which is the default value proposed by STARCCM+ [37].

2.4 Geometry and computational conditions

In this work, a 1/1-scale of the bare hull axisymmetric SUBOFF geometry with principal dimensions presented in Table 2.2 [40] is used. Figure 2.15 shows the bare hull SUBOFF model along with the body-fixed coordinate system with positive x_0 pointing toward the bow and negative z_0 pointing toward the free surface. The center of the body-fixed coordinate system coincides with the center of buoyancy of the model, which is located at the location $0.462L$ from the nose. As can be seen in Figure 2.15, the model possesses a bow part, a parallel middle part and a stern part with lengths presented in Table 2.2. The model has a length to diameter ratio equal to $L/D = 8.575$.

Table 2.2: Principal dimensions of the SUBOFF [40]

Length	4.356 m
Diameter	0.508 m
Bow-part length	1.016 m
Parallel Middle part length	2.229 m
Stern-part length	1.111 m
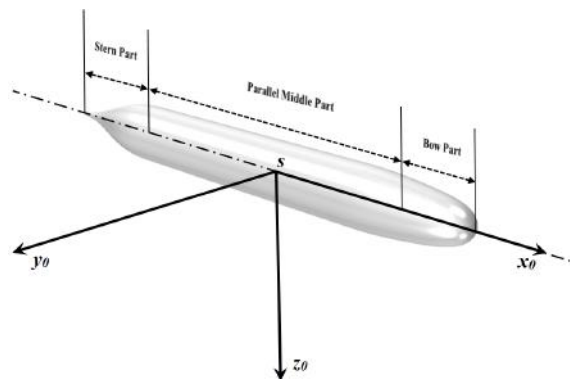
Figure 2.15: The axisymmetric SUBOFF bare hull model used in this thesis

In the present thesis, to obtain the axial force acting on the SUBOFF, the straight-ahead resistance tests are performed over Froude numbers and submergence depths ranging from $F_n = 0.205$ to $F_n = 0.512$ and from $h = 1.1D$ to $h = \infty$, respectively. Additionally, to estimate the forces and moment arising from the lateral velocity component, the drift tests are carried out at a constant advance velocity based on $F_n = 0.512$ over submergence depths and drift angles ranging from $h = 1.1D$ to $h = \infty$ and from $\beta = 0$ ($v' = 0$) to $\beta = 18.11°$ ($v' = -0.31$), respectively. Moreover, to calculate the forces and moment generated by the yaw rate, the rotating arm tests are performed at a constant advance velocity based on $F_n = 0.512$ over submergence depths and yaw angular velocities ranging from $h = 1.1D$ to $h = \infty$ and from $r' = -0.05$ to $r' = -0.4$, respectively.

It can be demonstrated that, in the rotating arm tests, the dimensionless yaw angular velocity has the following relation with the radius of rotation R:

$$r' = \frac{L}{R}. \tag{2.111}$$

Accordingly, the rotating arm tests are performed over the radius of rotations ranging from $R = 2.5L$ to $R = 20L$.

For the purpose of validation of the numerical simulations, several sets of available experimental data of the forces and moments acting on the bare hull SUBOFF model are employed.

Accordingly, the validation of the straight-ahead resistance tests is performed using the experimental resistance force data provided by LIU e HUANG [42] and WILSON-HAFFENDEN *et al.* [35]. The experiments of LIU e HUANG [42] are conducted on a 1/1-scale SUBOFF model at $h = \infty$ over Froude numbers ranging from $F_n = 0.438$ to $F_n = 1.416$. Additionally, to support the SUBOFF model during the experiments two NACA0015 struts are used. On the other hand, the experiments of WILSON-HAFFENDEN *et al.* [35] are performed on a 1/2.8-scale SUBOFF model over submergence depths and Froude numbers ranging from $h = 1.1D$ to $h = 3.3D$ and from $F_n = 0.128$ to $F_n = 0.640$, respectively. Moreover, to support the SUBOFF model during the experiments a mounting device composed of a vertical post and a horizontal sting is used.

Also, to validate the drift tests, the experimental data of the forces and moment acting on a 1/1-scale SUBOFF model given by RODDY [43] is used. The experiments are performed for $h = \infty$ and a constant advance velocity based on $F_n = 0.512$ over drift angles ranging from $\beta = 0$ ($v' = 0$) to $\beta = 18.11°$ ($v' = -0.31$). The model was supported using the same technique as that used by LIU e HUANG [42].

Furthermore, the validation of the rotating arm tests is performed using the experimental data of the forces and moment acting on a 1/1-scale SUBOFF model

provided by ETEBARI *et al.* [41]. The experiments are carried out for $h = \infty$ and a constant advance velocity based on $F_n = 0.236$ over drift angles and yaw angular velocities ranging from $\beta = -3.8°$ to $\beta = -16.5°$ and from $r' = -0.3577$ to $r' = -0.3702$, respectively. During the experiments, while the SUBOFF is supported using the same technique as that used by WILSON-HAFFENDEN *et al.* [35], it undergoes a turning motion at different yaw angular velocities and drift angles.

Note that the utilization of the horizontal sting by ETEBARI *et al.* [41] and WILSON-HAFFENDEN *et al.* [35] to support the SUBOFF during the experiments requires the truncation of the model in the stern region. Therefore, the presence of the sting, due to a reduction in the hull surface area together with the modification that it introduces into the pressure distribution over the stern region, affects the forces and moments acting on the UV.

Thus, in this study to validate the rotating arm tests using the data provided by ETEBARI *et al.* [41], the simulations are performed with the presence of the support, as shown in Figure 2.16. Furthermore, to identify the sting effect on the resistance force data provided by WILSON-HAFFENDEN *et al.* [35], the simulation for $F_n = 0.462$ and $h = 1.1D$ is repeated with the presence of the support, as shown in Figure 2.17.

Figure 2.16: The axisymmetric SUBOFF bare hull model with the support used by ETEBARI *et al.* [41]

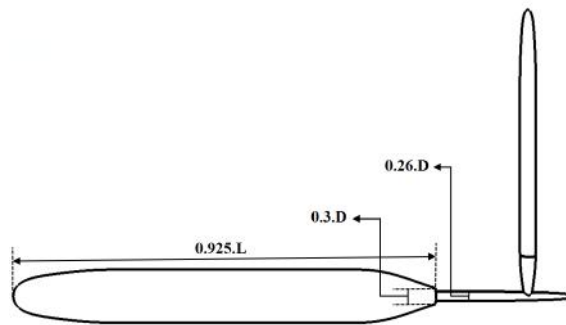Figure 2.17: The axisymmetric SUBOFF bare hull model with the support used by WILSON-HAFFENDEN *et al.* [35]

Note that, in the simulations, the submergence depth h is considered as the distance between the $x_0 s y_0$ plane and the calm water level (,i.e., the z coordinate of the $x_0 s y_0$ plane).

Finally, a general matrix of the simulations that are performed in this study is presented in Table 2.3.

Table 2.3: A general matrix of the simulations that are performed in this thesis. The table contains the ranges of the variables where the hydrodynamic forces and moments are obtained (RVFM), the ranges of the variables where the validations are carried out (RVV) and the ranges of the variables where the effect of the support used in the equivalent experiments is considered or investigated (SE).

Captive Test	RVFM	RVV	SE
Straight-ahead	$0.205 \leq F_n \leq 0.512$ $1.1D \leq h \leq \infty$	$0.205 \leq F_n \leq 0.512$ $1.1D \leq h \leq \infty$	$F_n = 0.462$ $h = 1.1D$
drift	$F_n = 0.512$ $0 \leq \beta \leq 18.11°$ $1.1D \leq h \leq \infty$	$F_n = 0.512$ $0 \leq \beta \leq 18.11°$ $h = \infty$	-
Rotating arm	$F_n = 0.512$ $-0.05 \leq r' \leq -0.4$ $1.1D \leq h \leq \infty$	$F_n = 0.236$ $-0.36 \leq r' \leq -0.37$ $-3.8° \leq \beta \leq -16.5°$ $h = \infty$	$F_n = 0.236$ $-0.36 \leq r' \leq -0.37$ $-3.8° \leq \beta \leq -16.5°$ $h = \infty$

2.5 Computational domains and boundary conditions

In the current thesis, to perform the straight-ahead resistance tests along with the drift tests, the computational domain is considered as a rectangular box; while to conduct the rotating arm tests, a computational domain in a circular form with a rectangular cross section is used.

Figure 2.18 shows the computational domain used to perform the straight-ahead resistance and drift tests for $h = \infty$. As can be seen, the computational domain stretches two body lengths ($2L$) in the upstream direction, five body lengths ($5L$) in the downstream direction and ten body diameters ($10D$) to the side, bottom and top. Because of the symmetry of the fluid flowing over the SUBOFF, only half of the UV is modeled.

The upstream boundary is considered as a velocity inlet, where a uniform velocity is specified based on Froude number. Furthermore, by using the reconstruction gradients the pressure on this boundary is extrapolated from the adjacent cells. In the downstream boundary a pressure outlet is defined. In this boundary, a relative pressure equal to zero is specified and the velocity is extrapolated from the interior cells using the reconstruction gradients. Additionally, the side, bottom and top boundaries are treated as symmetry walls, where the normal velocity along with the normal gradients of all the variables (except for the normal velocity) is assumed zero. Also, by using the reconstruction gradients the pressure on these boundaries is extrapolated from the adjacent cells.

In addition, Figures 2.19 and 2.20 show the computational domain used to per-

form the straight-ahead resistance and drift tests, respectively, with the presence of the free surface, i.e., for $1.1D \leq h \leq 3.3D$. Note that in the presence of the free surface the fluid flowing around the SUBOFF at a steady drift angle may not be symmetric; therefore, in the drift tests with the presence of the free surface the SUBOFF UV is fully simulated. On the other hand, in the straight-ahead resistance tests, due to the symmetry of the problem with respect to x_0sz_0 plane, only half of the UV is modeled. As can be seen in Figures 2.19 and 2.20, in both cases, the computational domain stretches two body lengths ($2L$) in the upstream direction, five body lengths ($5L$) plus a wavelength of the UV-generated waves in the downstream direction and ten body diameters ($10D$) plus a wavelength to side(s). Furthermore, in both cases, the box extends twenty body diameters ($20D$) above and below the body.

In both cases, at the upstream, top and bottom boundaries a velocity inlet is used, where a uniform velocity is specified based on Froude number. The use of the velocity inlet condition at the top and bottom boundaries eliminates the fluid reflection from these boundaries and also facilitates the modeling of an open sea, which is defined as deep water and infinite air conditions. Furthermore, by using the reconstruction gradients the pressure on these boundaries is extrapolated from the adjacent cells. Also, the downstream boundary is considered as a pressure outlet, where a hydrostatic pressure is specified and the velocity is extrapolated from the interior cells using the reconstruction gradients. Moreover, a symmetry boundary condition is used for the boundaries at two sides, where the normal velocity along with the normal gradients of all the variables (except for the normal velocity) is assumed zero. Also, by using the reconstruction gradients the pressure on these boundaries is extrapolated from the adjacent cells.

In the simulations with the presence of the free surface, to eliminate the wave reflections at the boundaries located at the downstream and (two) side(s), a damping zone is established next to these boundaries, as can be seen in Figures 2.19 (a) and 2.20 (a). In this zone, a source term, which acts as a resistance force, is added to the momentum equation of the vertical velocity component to cancel this component over the damping zone. Although in STARCCM+ this source term is defined as a combination of both linear and quadratic functions in terms of the vertical velocity component [37], only the linear one is used in this thesis. Thus, the linear source term with a coefficient defined as $f_1 = \pi\omega$ is added to the momentum equation of the vertical velocity component over the damping zone, which has a thickness equal to the length of the UV-generated wave system. This configuration for the source term and the damping zone thickness is recommended by PERIĆ e ABDEL-MAKSOUD [67] for simple flow phenomena and, as shown by MAALI AMIRI et al. [19], works satisfactory in the present simulations.

Finally, Figures 2.21 (a) and (b) depict the computational domains used to simulate the rotating arm tests for $h = \infty$ and for $1.1D \leq h \leq 3.3D$, respectively. For $h = \infty$ due to the symmetry of the problem regarding the $x_0 s y_0$ plane, only half of the UV is modeled, while for $1.1D \leq h \leq 3.3D$ the SUBOFF UV is fully simulated. Note that, in both cases, the distances of the boundaries from the SUBOFF are considered the same as those used to perform the straight-ahead resistance and drift tests. Additionally, the boundary conditions are predominantly the same as those used to carry out the straight-ahead resistance and drift tests, except for the boundaries located at two sides of the domain. In this regard, to prevent any fluid reflection, a velocity inlet is also used at the two boundaries located at two sides, which as a result facilitates the iterative convergence of the simulations related to the rotating arm tests.

It is worthy to mention that, in this study, the rotational motion is implemented by rotating the flow around the stationary SUBOFF UV, which is the same approach used in the research conducted by TOXOPEUS *et al.* [68]. Therefore, as a rotating coordinate system is adopted to perform the simulations of the rotating arm tests, the Coriolis and centrifugal forces (Equation 2.59) resulting from the computation in a rotating reference frame are added explicitly to the momentum equations as source terms.

Note that, in all the simulations in this thesis, a no-slip boundary condition is imposed over the SUBOFF model, which states that the relative velocity between the body surface and the fluid immediately at the body surface is zero. Thus, from the continuity equation it can be inferred that the normal gradient of the normal velocity is also zero on this boundary. Also, by using the reconstruction gradients the pressure on this boundary is extrapolated from the adjacent cells.

Additionally, the treatment of the Reynolds stresses on the boundaries is presented in Appendix C.

(a) Top View   (b) Side View, for $\beta = 0$
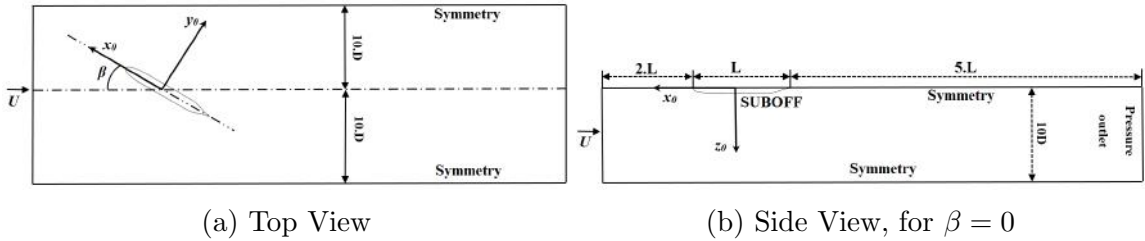
Figure 2.18: Computational domain used to perform the straight-ahead resistance and drift tests for $h = \infty$

(a) Top View   (b) Side View
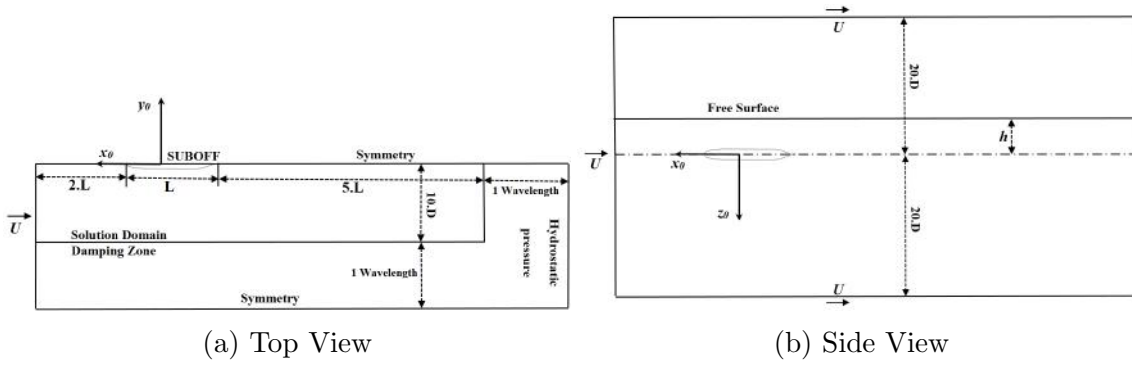
Figure 2.19: Computational domain used to perform the straight-ahead resistance tests with the presence of the free surface, i.e., for $1.1D \leq h \leq 3.3D$

(a) Top View   (b) Side View, at $\beta = 0$
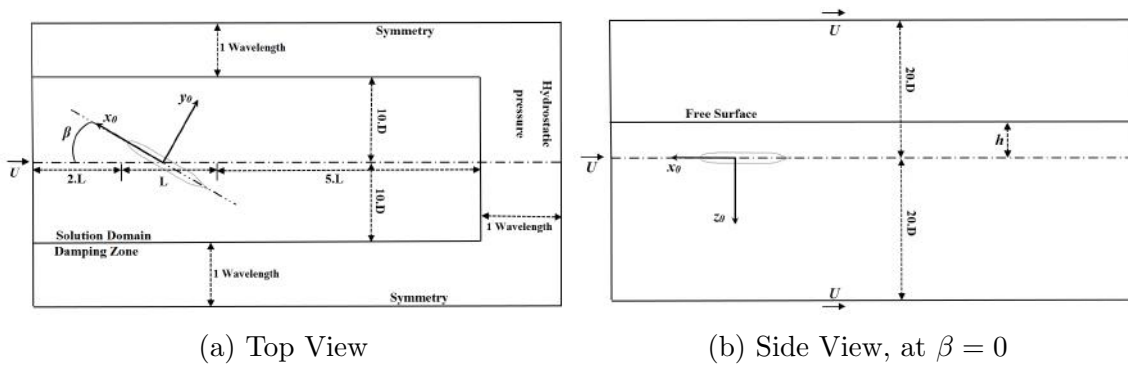
Figure 2.20: Computational domain used to perform the drift tests with the presence of the free surface, i.e., for $1.1D \leq h \leq 3.3D$

(a) Top View, at $h = \infty$ (b) Top View, for $1.1D \leq h \leq 3.3D$
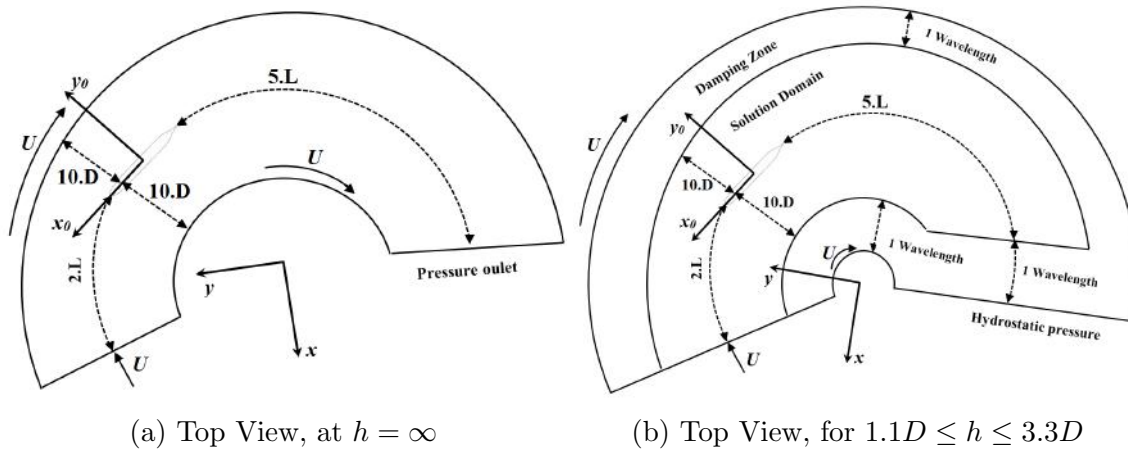
Figure 2.21: Computational domains used to simulate the rotating arm tests for $h = \infty$ and for $1.1D \leq h \leq 3.3D$

2.6   Grid generation

The grid in this study is generated automatically by STARCCM+ using two different methods: prism layer and trimmer.

The trimmer mesh is used to discretize almost the entire computational domain except for the region close to the body surface. This mesh is mainly composed of hexahedral cells with a small number of trimmed cells next to the UV hull to accommodate the body.

Additionally, the prism layer mesh, which is constructed from orthogonal prismatic cells, is employed to resolve the turbulent boundary layer close to the body surface. In this mesh, a geometric progression with an expansion factor of 1.1 is used to increase progressively the thickness of the prismatic cells from the inner cell immediately next to the UV hull to the outer cells. Furthermore, as the RST model in this thesis employs the standard wall function to capture the near-wall turbulence, the first cell immediately next to body surface resides within the logarithmic region of the boundary layer. This corresponds to the Y^+ values in the range from 30 to 100.

Moreover, to capture properly the wave system generated by the UV together with the pressure drop in the wake region and leeward side of the SUBOFF at drift, appropriate local mesh refinements are utilized. For instance, as recommended by SPENCE [65], approximately 100 to 160 cells in wavelength and 30 to 50 cells in height discretize the free surface to resolve properly the generated wave system of the UV. A detailed description of the grid generation process can be found in Appendix A

In this regard, Figures 2.22, 2.23, 2.24 and 2.25 present the grids used to simulate the straight-ahead resistance tests, the straight-ahead resistance tests with the presence of the support used by WILSON-HAFFENDEN *et al.* [35], the drift tests and the rotating arm tests, respectively. Local mesh refinements used in the mesh generation process can be clearly identified in these figures.
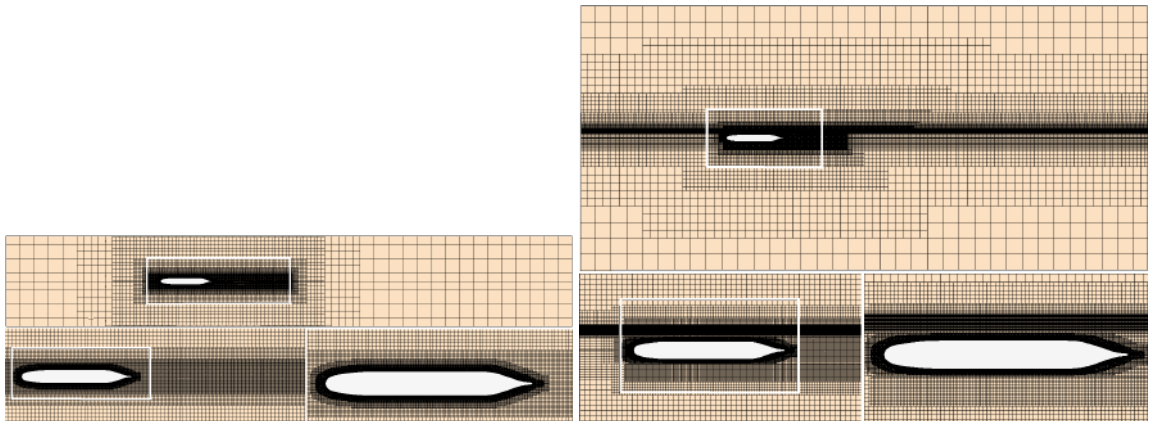
(a) The grid generated in $x_0 s y_0$ plane for $F_n = 0.466$ and $h = \infty$

(b) The grid generated in $x_0 s z_0$ plane for $F_n = 0.462$ and $h = 1.1D$

Figure 2.22: Grids used to simulate the straight-ahead resistance tests

Figure 2.23: Generated grid in $x_0 s z_0$ plane, which is used to repeat the straight-ahead resistance test for $F_n = 0.462$ and $h = 1.1D$ with the presence of the support used in the equivalent experiments of WILSON-HAFFENDEN *et al.* [35].
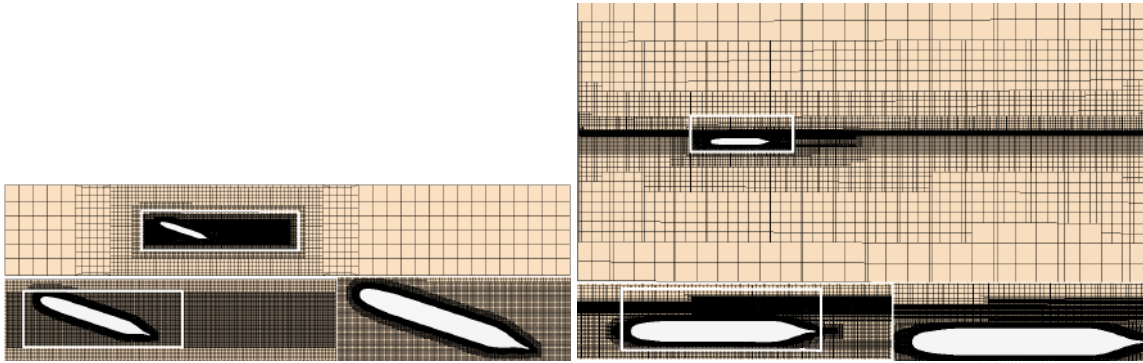
(a) The grid generated in $x_0 s y_0$ plane for $\beta = 18.11°$ ($v' = -0.31$) and $h = \infty$

(b) The grid generated in $x_0 s z_0$ plane for $\beta = 18.11°$ ($v' = -0.31$) and $h = 1.1D$

Figure 2.24: Grids used to simulate the drift tests

(a) The grid generated in $x_0 s y_0$ plane for $\beta = -14.3°$, $r' = -0.3681$ and $h = \infty$, which is used to validate the simulations of the rotating arm tests. Note that the support used in the equivalent experiments conducted by ETE-BARI *et al.* [41] is also present.

(b) The grid generated in $x_0 s y_0$ plane for $r' = -0.4$ and $h = \infty$

(c) The grid generated in $x_0 s z_0$ plane for $r' = -0.4$ and $h = 1.1D$
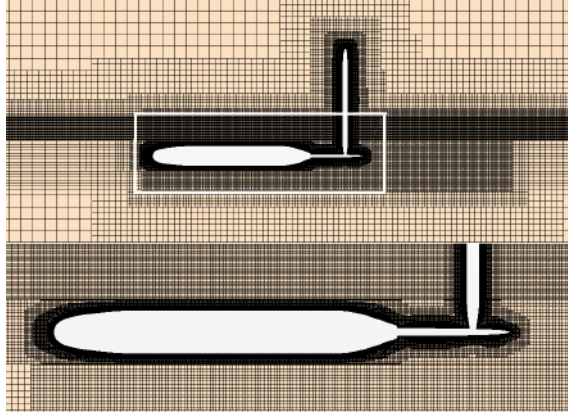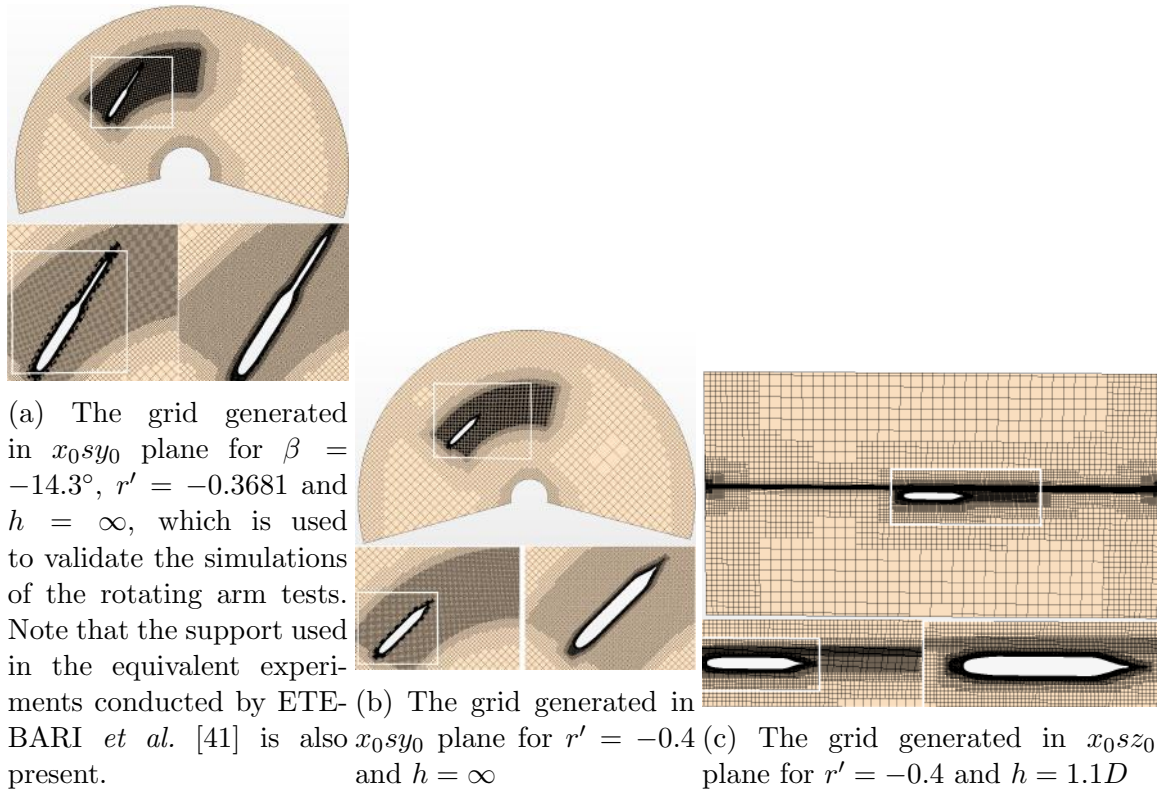
Figure 2.25: Grids used to simulate the rotating arm tests

Chapter 3

Verification and Validation

This chapter deals with the verification and validation of the numerical model used in this thesis. Herein, the verification process encompasses the grid convergence study together with the evaluation of the effect of the support used in the experiments conducted by WILSON-HAFFENDEN *et al.* [35] on the forces and moment acting on the SUBOFF. Additionally, the validation includes the comparison of the calculated forces and moments with the available measured ones. As outlined in Table 2.3, the validation is performed over the ranges of variables for which the experimental data are available.

3.1   Grid convergence study

In this section, the sensitivity of the solutions to the grid resolution is determined through performing a systematic grid convergence study over three grids, namely I, II and III. This study is carried out for each hydrodynamic test at two different computational conditions: without and with the presence of the free surface, i.e., for $h = \infty$ and $h = 1.1D$.

In this research, to refine the grid systematically, all the mesh quantities in the grid generation process are defined in terms of a reference value called BS. In this regard, the grid is uniformly refined using a refinement factor equal to 1.2 in all the dimensional directions.

Accordingly, the grid convergence study for the straight-ahead resistance tests is carried out without the presence of the free surface for $h = \infty$ and $F_n = 0.466$, and with the presence of the free surface for $h = 1.1D$ and $F_n = 0.462$. Tables 3.1 and 3.2 show the grids I, II and III used for grid convergence study in straight-ahead tests.

Moreover, this study for the drift tests is carried out without the presence of the free surface for $h = \infty$, $F_n = 0.512$ and $v' = -0.31$ ($\beta = 18.11°$), and with the presence of the free surface for $h = 1.1D$, $F_n = 0.512$ and $v' = -0.31$ ($\beta = 18.11°$).

Tables 3.3 and 3.4 show the grids I, II and III used for grid convergence study in drift tests.

Furthermore, the grid convergence study for the rotating arm tests is performed without the presence of the free surface for $h = \infty$, $F_n = 0.236$, $r' = -0.3702$ and $\beta = -16.5°$, and with the presence of the free surface for $h = 1.1D$, $F_n = 0.512$ and $r' = -0.4$. Note that, the simulation without the presence of the free surface is performed with the presence of the support used in the experiments conducted by ETEBARI *et al.* [41]. Tables 3.5 and 3.6 show the grids I, II and III used for grid convergence study in rotating arm tests.

Table 3.1: Different grids used for grid convergence study in straight-ahead resistance tests at $h = \infty$

Mesh	BS (m)	Number of cells
I	1.2^2	$1,476,570$
II	1.2	$2,187,240$
III	1	$3,286,182$

Table 3.2: Different grids used for grid convergence study in straight-ahead resistance tests at $h = 1.1D$

Mesh	Time Step	BS (m)	Number of cells
I	$1.2^2 \times 0.02$	1.2^2	$4,263,986$
II	0.02	1.2	$7,880,477$
III	$\frac{0.02}{1.2^2}$	1	$12,650,388$

Table 3.3: Different grids used for grid convergence study in drift tests at $h = \infty$

Mesh	BS (m)	Number of cells
I	1.2^2	$2,233,578$
II	1.2	$3,412,608$
III	1	$5,065,748$

Table 3.4: Different grids used for grid convergence study in drift tests at $h = 1.1D$

Mesh	Time Step	BS (m)	Number of cells
I	$1.2^2 \times 0.0288$	1.2^2	$4,720,191$
II	0.0288	1.2	$7,676,547$
III	$\frac{0.0288}{1.2^2}$	1	$11,818,224$

Table 3.5: Different grids used for grid convergence study in rotating arm tests at $h = \infty$

Mesh	BS (m)	Number of cells
I	1.2^2	$2,066,039$
II	1.2	$3,126,058$
III	1	$4,872,519$

Table 3.6: Different grids used for grid convergence study in rotating arm tests at $h = 1.1D$

Mesh	Time Step	BS (m)	Number of cells
I	$1.2^2 \times 0.0288$	1.2^2	$3,540,027$
II	0.0288	1.2	$5,249,496$
III	$\frac{0.0288}{1.2^2}$	1	$7,779,781$

Figure 3.1 represents the Y^+ distribution over the SUBOFF hull using grid III presented in Table 3.1, which is the finest grid utilized in this thesis. As can be seen, the Y^+ values mostly fall in the range from 30 to 100 where the wall function can be used.
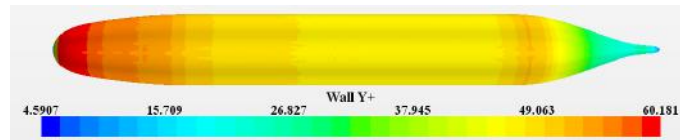
Figure 3.1: Y^+ distribution over the SUBOFF hull using grid III presented in Table 3.1

The BS values used in the simulations are shown in Tables 3.1, 3.2, 3.3, 3.4, 3.5 and 3.6. Additionally, note that, in the simulations with the presence of the free surface, the spatial grid refinement is accompanied by a temporal refinement. However, since the orders of accuracy are different in space and time, the temporal refinement factor is defined in such a manner so as to obtain the same order of error reduction in both the temporal and spatial discretizations [69]. Accordingly, as a second-order scheme is used for spatial discretization and a first-order one for temporal discretization, temporal refinement factor is chosen as the square of the spatial refinement factor [69].

In this regard, in the simulations with the presence of the free surface, the time-step size for grid II is calculated as $\frac{\text{wave period}}{\text{number of cells per wavelength}}$, which is recommended by STARCCM+ [37], and then it is adjusted in the corresponding grids I and III, based on the square of the spatial refinement factor, as mentioned above.

Therefore, using the sets of grids presented in Tables 3.1, 3.2, 3.3, 3.4, 3.5 and 3.6, the simulations are performed to calculate the X-force from the straight-ahead resistance tests for $h = \infty$ together with the X-force, Z-force and M-moment from the same tests for $h = 1.1D$. Additionally, from the drift tests for $h = \infty$ the X-force, Y-force and N-moment and from the same tests for $h = 1.1D$ the X-force, Y-force, N-moment, Z-force and M-moment are calculated. Furthermore, the simulations of the rotating arm tests are performed for $h = \infty$ to estimate the X-force, Y-force and N-moment and the same tests are performed for $h = 1.1D$ to determine the X-force, Y-force, N-moment, Z-force and M-moment. Tables 3.7, 3.8, 3.9, 3.10, 3.11 and 3.12 show the normalized values of the forces and moments obtained from the corresponding simulations.

Table 3.7: Normalized X-force obtained from the simulations of the straight-ahead resistance tests for $h = \infty$

Mesh	X'
I	-0.00080838
II	-0.00080364
III	-0.00080154

Table 3.8: Normalized X-force, Z-force and M-moment obtained from the simulations of the straight-ahead resistance tests for $h = 1.1D$

Mesh	X'	Z'	M'
I	-0.0020631	-0.0008504	-0.000718
II	-0.0020478	-0.0008556	-0.000722
III	-0.0020392	-0.0008591	-0.000721

Table 3.9: Normalized X-force, Y-force and N-moment obtained from the simulations of the drift tests for $h = \infty$

Mesh	X'	Y'	N'
I	-0.000700	0.0064293	0.0030451
II	-0.000693	0.0064321	0.0030512
III	-0.000688	0.0064339	0.0030549

Table 3.10: Normalized X-force, Y-force, Z-force, N-moment and M-moment obtained from the simulations of the drift tests for $h = 1.1D$

Mesh	X'	Y'	N'	Z'	M'
I	-0.003043	0.010944	0.002646	0.002931	-0.0005344
II	-0.003025	0.010915	0.002654	0.002882	-0.0005247
III	-0.003011	0.010897	0.002659	0.002849	-0.0005183

Table 3.11: Normalized X-force, Y-force and N-moment obtained from the simulations of the rotating arm tests for $h = \infty$

Mesh	X'	Y'	N'
I	-0.0023044	-0.007080661	-0.0018664
II	-0.0022957	-0.007126781	-0.001854916
III	-0.0022892	-0.007157779	-0.001848176

Table 3.12: Normalized X-force, Y-force, Z-force, N-moment and M-moment obtained from the simulations of the rotating arm tests for $h = 1.1D$

Mesh	X'	Y'	N'	Z'	M'
I	-0.00271	-0.00093638	0.00057401	-0.000009938	-0.000752194
II	-0.0026985	-0.00094463	0.00057672	-0.000009659	-0.000752711
III	-0.0027055	-0.00095071	0.00057841	-0.000009431	-0.000752304

Tables 3.13, 3.14, 3.15, 3.16, 3.17 and 3.18 show the percentage of changes in the corresponding forces and moments obtained from the simulations. As can be seen, the changes in the forces and moments between grids II and III are consistently smaller than the changes in the forces and moments between grids I and II. This drop in the changes of the forces and moments indicates the convergence of the solutions as the grid is refined.

Table 3.13: Percentage of changes in the variable between grids used in the straight-ahead resistance tests at $h = \infty$

% changes	X'
I to II	-0.59
II to III	-0.26

Table 3.14: Percentage of changes in the variables between grids used in the straight-ahead resistance tests at $h = 1.1D$

% changes	X'	Z'	M'
I to II	-0.74	0.61	0.56
II to III	-0.42	0.41	-0.14

Table 3.15: Percentage of changes in the variables between grids used in the drift tests at $h = \infty$

% changes	X'	Y'	N'
I to II	-1.000	0.044	0.200
II to III	-0.722	0.028	0.121

Table 3.16: Percentage of changes in the variables between grids used in the drift tests at $h = 1.1D$

% changes	X'	Y'	N'	Z'	M'
I to II	-0.592	-0.265	0.302	-1.672	-1.815
II to III	-0.462	-0.165	0.188	-1.145	-1.220

Table 3.17: Percentage of changes in the variables between grids used in the rotating arm tests at $h = \infty$

% changes	X'	Y'	N'
I to II	-0.378	0.651	-0.615
II to III	-0.283	0.435	-0.363

Table 3.18: Percentage of changes in the variables between grids used in the rotating arm tests at $h = 1.1D$

% changes	X'	Y'	N'	Z'	M'
I to II	-0.424	0.881	0.472	-2.807	0.069
II to III	0.259	0.644	0.293	-2.360	-0.054

Based on the changes of the forces and moments between the grids, the convergence ratio, which is required for the estimation of the order of discretization together with the grid uncertainty, can be estimated as follows:

$$R_G = \frac{\varepsilon_{G32}}{\varepsilon_{G21}}, \tag{3.1}$$

where $\varepsilon_{G_{32}} = S_{III} - S_{II}$ is the variation in the forces/moments between grids II and III, and $\varepsilon_{G_{21}} = S_{II} - S_I$ is the variation in the forces/moments between grids I and II.

The values of R_G indicate the following four conditions [70]:

1. $0 < R_G < 1$, monotonic convergence.

2. $-1 < R_G < 0$, oscillatory convergence.

3. $R_G > 1$, monotonic divergence.

4. $R_G < -1$, oscillatory divergence.

For conditions 3 and 4, where the grid divergence occurs no order of discretization and uncertainty can be calculated. For condition 2, only the uncertainty is calculated as:

$$U_G = \frac{1}{2}|S_U - S_L|, \tag{3.2}$$

where S_U and S_L are the maximums and minimums of the oscillations of the forces and moments [70]. For condition 1, where the grid convergence occurs and the forces and moments show asymptotic monotonic convergence, the generalized Richardson extrapolation [71] based on the procedure proposed by MCHALE e FRIEDMAN [72] is used to calculate the order of discretization together with the grid uncertainty.

In this regard, first the refinement factors between grids I, II and III are determined as:

$$r_{12} = \frac{h_I}{h_{II}},$$
$$\tag{3.3}$$
$$r_{23} = \frac{h_{II}}{h_{III}},$$

where h_i is defined as a representative cell size and is calculated as follows:

$$h_i = \sqrt[3]{\frac{\text{Total Volume}}{\text{Total Number of Cells in Grid i}}}. \tag{3.4}$$

Then, one can calculate the observed order of discretization using the following relation:

$$P_G = \frac{1}{\ln r_{23}} \left[\ln \left(\frac{1}{R_G} \right) + \ln \left(\frac{r_{23}^{P_G} - 1}{r_{12}^{P_G} - 1} \right) \right]. \tag{3.5}$$

Finally, the uncertainties associated with the forces and moments calculated from grids II are predicted as follows:

$$U_G = F_S \left| \frac{\varepsilon_{G_{32}}}{S_{II}(r_{23}^{P_G} - 1)} \right|, \tag{3.6}$$

where F_S indicates the factor of safety, which is assigned a value of 1.25 for three-grid studies. The value of U_G is a measure of the distance between the values of the forces and moments obtained from the simulations and their asymptotic values. In other words, small values of U_G demonstrate that the values of the solution results are close to their asymptotic values.

The values of R_G, P_G and U_G related to the forces and moments obtained from the grids II are given in Tables 3.19, 3.20, 3.21, 3.22, 3.23 and 3.24.

Based on the values of R_G, almost all the forces and moments show an asymptotic monotonic convergence behavior, except for the M-moment obtained from the simulations of the straight-ahead resistance tests for $h = 1.1D$ and the X-force and M-moment both obtained from the simulations of the rotating arm tests for $h = 1.1D$, which all show an oscillatory convergence behavior.

In Tables 3.19, 3.20, 3.21, 3.22, 3.23 and 3.24, deviations of the observed P_G from its theoretical value, which is 2, is observed. These deviations can be due to several factors such as the boundary conditions, the existing non-linearities in the problem, turbulence modeling and mesh quality, EÇA e HOEKSTRA [73]. Additionally, in cases with super-convergence of the observed order of discretization, i.e., $P_G > 2$, the theoretical value of P_G is used instead of the observed P_G to calculate the grid uncertainty, as recommended by EÇA e HOEKSTRA [73]. Since, according to EÇA e HOEKSTRA [73], the super-convergence of the observed P_G is unreliable and is only the consequence of several factors such as the existing non-linearities in the problem, turbulence modeling and mesh quality.

Generally, the small values of the U_G presented in Tables 3.19, 3.20, 3.21, 3.22, 3.23 and 3.24 demonstrate the negligible sensitivity of the solutions to the grid resolution.

Table 3.19: Calculated U_G and the order of discretization of X-force obtained from the simulation of the straight-ahead resistance tests for $h = \infty$

Quantity	R_G	P_G	$U_G \% S_{II}$
X'	0.44	6.39	1.05

Table 3.20: Calculated U_G and the order of discretization of X-force, Z-force and M-moment obtained from the simulation of the straight-ahead resistance tests for $h = 1.1D$

Quantity	R_G	P_G	$U_G\%S_{II}$
X'	0.56	1.73	1.67
Z'	0.67	0.74	4.1
M'	-0.25	-	0.28

Table 3.21: Calculated U_G and the order of discretization of X-force, Y-force and N-moment obtained from the simulation of the drift tests for $h = \infty$

Quantity	R_G	P_G	$U_G\%S_{II}$
X'	0.71	1.94	3.09
Y'	0.64	2.71	0.12
N'	0.61	3.14	0.50

Table 3.22: Calculated U_G and the order of discretization of X-force, Y-force, Z-force, N-moment and M-moment obtained from the simulation of the drift tests for $h = 1.1D$

Quantity	R_G	P_G	$U_G\%S_{II}$
X'	0.78	0.86	4.40
Y'	0.62	2.33	0.62
N'	0.63	2.28	0.71
Z'	0.67	1.79	4.85
M'	0.70	1.54	6.55

Table 3.23: Calculated U_G and the order of discretization of X-force, Y-force and N-moment obtained from the simulation of the rotating arm tests for $h = \infty$

Quantity	R_G	P_G	$U_G\%S_{II}$
X'	0.75	2.53	1.03
Y'	0.67	3.27	1.58
N'	0.59	4.23	1.32

Table 3.24: Calculated U_G and the order of discretization of X-force, Y-force, Z-force, N-moment and M-moment obtained from the simulation of the rotating arm tests for $h = 1.1D$

Quantity	R_G	P_G	$U_G\%S_{II}$
X'	-0.61	-	0.21
Y'	0.74	2.32	2.68
N'	0.62	3.59	1.22
Z'	0.82	1.90	10.41
M'	-0.79	-	0.03

Finally, as the changes in the forces and moments between grids II and III are indeed smaller than the changes in the forces and moments between grids I and II, the grids II are chosen to perform the rest of the simulations in this thesis.

3.2 Validation

In this section, the validation of the numerical simulations for each captive test is performed by comparing the calculated forces and moments against the available experimental data. In this regard, based on TOXOPEUS *et al.* [68], it is assumed that the numerical simulations are solely affected by the uncertainty associated with the grid U_G. Accordingly, the validation uncertainty U_{val} is calculated as:

$$U_{val} = \sqrt{U_G^2 + U_E^2} \tag{3.7}$$

where U_E is the uncertainty in the experimental measurement. Accordingly, if the comparative difference between the calculated and measured forces and moments is smaller than the validation uncertainty U_{val}, it is said that the model is validated; otherwise, the model is not validated.

3.2.1 Validation of the simulations of the straight-ahead resistance tests

To validate the simulations of the straight-ahead resistance tests, the normalized X-force obtained from these simulations is compared against the experimental data given by LIU e HUANG [42] and WILSON-HAFFENDEN *et al.* [35] over Froude numbers and submergence depths ranging from $F_n = 0.205$ to $F_n = 0.512$ and from $h = 1.1D$ to $h = \infty$, respectively. Note that the experiments of LIU e HUANG [42] are performed for $h = \infty$ while the experiments of WILSON-HAFFENDEN *et al.* [35] are carried out for submergence depths $h = 1.1D$ through $h = 3.3D$.

To the knowledge of the present author, no uncertainty has been reported by LIU e HUANG [42] in the measurement of the X-force. On the other hand, the uncertainty in the measurement of the X-force in the experiments conducted by WILSON-HAFFENDEN *et al.* [35] is reported to be within $U_E = 3.1\%$. Note that the uncertainty reported by WILSON-HAFFENDEN *et al.* [35] does not include the contribution from the support used during the experiments.

Figure 3.2 depicts the normalized calculated and measured X-forces. The general trends of the calculated X-force are similar to those of the measured one. The numerical model has captured reasonably well the oscillatory behavior of the X-force at the shallowest submergence depth. The average comparative difference between the calculated and measured X-forces for $h = \infty$ is approximately 4.05%, while for submergence depths $h = 1.1D$ through $h = 3.3D$ this value is about 10.27%. The larger difference for the simulations with the presence of the free surface is attributed to the presence of the support used in the experiments, which is further evaluated in the next section. The validation uncertainty associated with the X-force for submergence depths $h = 1.1D$ through $h = 3.3D$ is $U_{val} = \sqrt{U_G^2 + U_E^2} = \sqrt{1.67^2 + 3.1^2} = 3.52\%$. It will be shown that taking into account the support effect reduces the difference between the calculated and measured X-forces to a point, where it falls within the validation uncertainty $U_{val} = 3.52\%$.
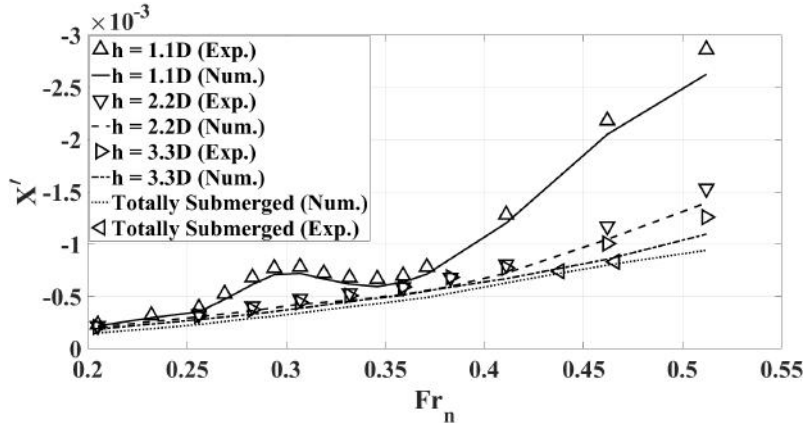

Figure 3.2: Normalized calculated and measured (LIU e HUANG [42] and WILSON-HAFFENDEN *et al.* [35]) X-forces obtained from the straight-ahead resistance tests for Froude numbers and submergence depths ranging from $F_n = 0.205$ to $F_n = 0.512$ and from $h = 1.1D$ to $h = \infty$, respectively

3.2.2   Validation of the simulations of the drift tests

To validate the simulations of the drift tests, the normalized X-force, Y-force and N-moment obtained from these simulations are compared against the experimental data given by RODDY [43] for $h = \infty$ and $F_n = 0.512$ over lateral velocities ranging from $v' = 0$ ($\beta = 0$) to $v' = -0.311$ ($\beta = 18.11°$). The uncertainty in the measure-

ments of the the X-force, Y-force and N-moment was reported to be $U_E = 10\%$, which does not include the contribution from the mounting device.

Figures 3.3 (a), (b) and (c) depict the normalized calculated and measured X-forces, Y-forces and N-moments. The calculated forces and moment are found to be in a fairly good agreement with the measured ones. However, for $|v'| < 0.035$ ($\beta < 2°$) an unexpected large difference between the calculated and measured Y-forces and N-moments is observed. For instance, for $v' = -0.018$ ($\beta = 1.06°$) comparative differences between the calculated and measured Y-forces and N-moments are roughly 50% and 27%, respectively. These large differences are unusual because, as pointed out by CHESNAKAS e SIMPSON [25], KIM *et al.* [55] and PHILLIPS *et al.* [54], the accurate prediction of the forces and moments acting on an axisymmetric UV hull at incidence is particularly difficult at large angles of drift due to the development of the complex three dimensional crossflow separation over the body at this range. Therefore, the large discrepancies observed for $|v'| < 0.035$ ($\beta < 2°$) are likely due to either the resolution of the load cells used during the experiments, which apparently was not adequate for the measurement of the small forces or a numerical problem in the calculation of the forces and moments of very small values.

Aside from the large differences observed for $|v'| < 0.035$ ($\beta < 2°$), the average comparative differences between the numerical and experimental X-forces, Y-forces and N-moments are about 4.01%, 6.07% and 5.58%. Additionally, the validation uncertainties associated with the X-force, Y-force and N-moment are $U_{val} = \sqrt{U_G^2 + U_E^2} = \sqrt{3.09^2 + 10^2} = 10.47\%$, $U_{val} = \sqrt{U_G^2 + U_E^2} = \sqrt{0.12^2 + 10^2} = 10.00\%$ and $U_{val} = \sqrt{U_G^2 + U_E^2} = \sqrt{0.50^2 + 10^2} = 10.01\%$, respectively. Therefore, the calculated X-force, Y-force and N-moment are well within their validation uncertainties.
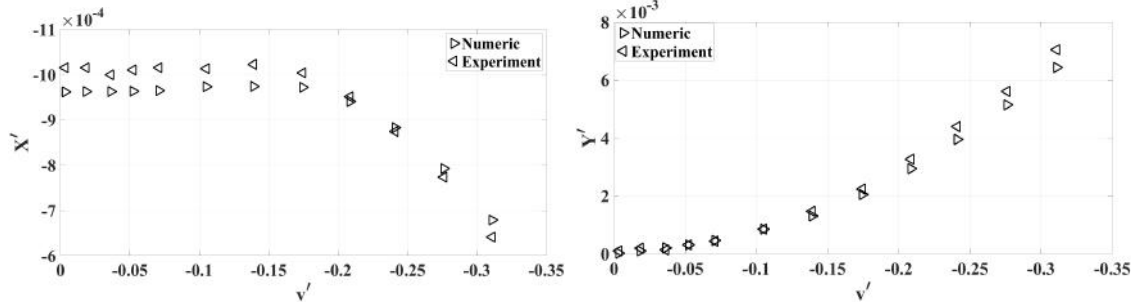
(a) Normalized calculated and measured X-forces obtained from the drift tests for $F_n = 0.512$ and $h = \infty$ over lateral velocities ranging from $v' = 0$ to $v' = -0.311$

(b) Normalized calculated and measured Y-forces obtained from the drift tests for $F_n = 0.512$ and $h = \infty$ over lateral velocities ranging from $v' = 0$ to $v' = -0.311$
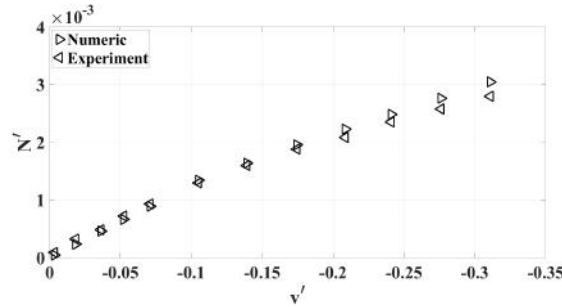
(c) Normalized calculated and measured N-moments obtained from the drift tests for $F_n = 0.512$ and $h = \infty$ over lateral velocities ranging from $v' = 0$ to $v' = -0.311$

Figure 3.3: Comparison of the calculated forces and moment against the experimental data presented by RODDY [43] in drift tests

### 3.2.3 Validation of the simulations of the rotating arm tests

To validate the simulations of the rotating arm tests the X-force, Y-force and N-moment obtained from these simulations are compared against the experimental data given by ETEBARI *et al.* [41] for $h = \infty$ and $F_n = 0.236$ over drift angles and angular yaw velocities ranging from $\beta = -3.8°$ to $\beta = -16.5°$ and from $r' = -0.3577$ to $r' = -0.3702$, respectively. As mentioned earlier, the simulations are performed with the presence of the support shown in Figure 2.16. The experiments incorporate two hydrodynamic tests, the rotating arm and drift tests, in a single test, which is the case of a UV undergoing a steady turning maneuver shown in Figure 2.9. The uncertainty in the measurements of the X-force, Y-force and N-moment in the experiments conducted by ETEBARI *et al.* [41] is reported to be within $U_E = 8.1\%$, $U_E = 4.9\%$ and $U_E = 4.1\%$, respectively, which does not include the contribution from the mounting device.

Figures 3.4 (a), (b) and (c) show the normalized calculated and measured X-forces, Y-forces and N-moments. As can be seen, the numerical model captures

reasonably well the general trend of the experimental data. The average comparative differences between the calculated and measured X-forces, Y-forces and N-moments are approximately 4.32%, 4.78% and 4.04%. Additionally, the validation uncertainties associated with the X-force, Y-force and N-moment are $U_{val} = \sqrt{U_G^2 + U_E^2} = \sqrt{1.03^2 + 8.1^2} = 8.17\%$, $U_{val} = \sqrt{U_G^2 + U_E^2} = \sqrt{1.58^2 + 4.9^2} = 5.15\%$ and $U_{val} = \sqrt{U_G^2 + U_E^2} = \sqrt{1.32^2 + 4.1^2} = 4.31\%$, respectively. Thus, the calculated X-force, Y-force and N-moment fall within their validation uncertainties.
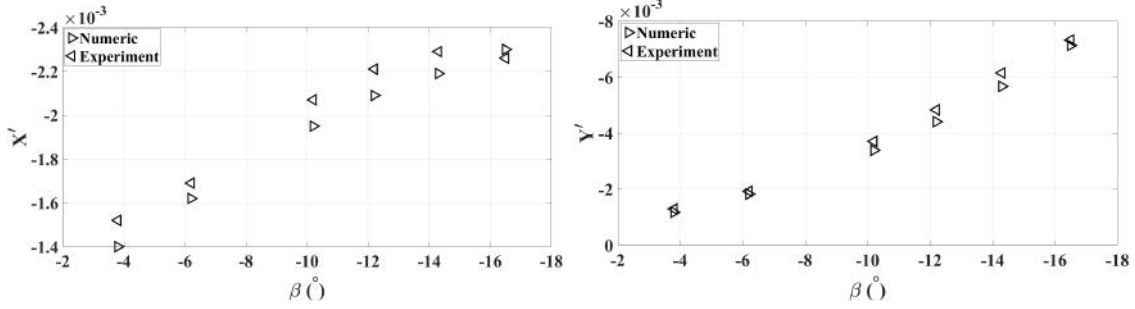
(a) Normalized calculated and measured X-forces obtained from the rotating arm tests for $F_n = 0.236$ and $h = \infty$ over drift angles and yaw angular velocities from $\beta = -3.8°$ to $\beta = -16.5°$ and from $r' = -0.3577$ to $r' = -0.3702$, respectively

(b) Normalized calculated and measured Y-forces obtained from the rotating arm tests for $F_n = 0.236$ and $h = \infty$ over drift angles and yaw angular velocities ranging from $\beta = -3.8°$ to $\beta = -16.5°$ and from $r' = -0.3577$ to $r' = -0.3702$, respectively
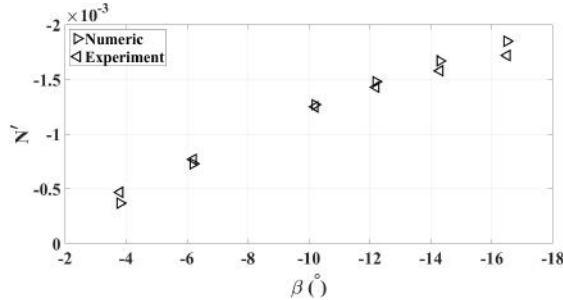
(c) Normalized calculated and measured N-moments obtained from the rotating arm tests for $F_n = 0.236$ and $h = \infty$ over drift angles and yaw angular velocities ranging from $\beta = -3.8°$ to $\beta = -16.5°$ and from $r' = -0.3577$ to $r' = -0.3702$, respectively

Figure 3.4: Comparison of the calculated forces and moment against the experimental data presented by ETEBARI *et al.* [41] in rotating arm tests

3.3 The effect of the support

In this section, the effect of the support used in the experiments conducted by WILSON-HAFFENDEN *et al.* [35] on the X-force, Z-force and M-moment acting on the SUBOFF for $F_n = 0.462$ and $h = 1.1D$ is investigated. In this regard, the

simulation is performed with the presence of the support, as shown in Figure 2.17. The grid used for this simulation is represented in Figure 2.23.

Table 3.25 shows the normalized values of the experimental and numerical X-forces with and without the presence of the support. As can be seen, the presence of the support increases the X-force by approximately 9%, which indicates an improvement in the X-force prediction. Thus, as mentioned in section 3.2.1, it can be inferred that by considering the support effect, the calculated values of the X-forces presented in section 3.2.1 will fall within the validation uncertainty bound.

Notice that adding the support to the stern region causes a reduction in the surface area of the SUBOFF, which consequently decreases the frictional component of the X-force. However, for a UV traveling close to the free surface the pressure component also contributes remarkably to the X-force. In this regard, the presence of a sting in the stern region reduces the normal pressure acting on this region and thus increases the pressure difference between the fore and aft parts. This, accordingly, results in an increase in the X-force.

Table 3.25 further shows the normalized values of the Z-force and M-moment with and without the presence of the support for $F_n = 0.462$ and $h = 1.1D$. It can be inferred that, at this Froude number, the presence of the support causes the nearly-negligible 2.5% and 2.1% increase in the Z-force and M-moment, respectively.

Table 3.25: Normalized X-force, Z-force and M-moment calculated for $h = 1.1D$ and $F_n = 0.462$ with the presence of the support (WS) and without the presence of the support (WOS)

Quantity	X'	Z'	M'
(Exp.)	-0.002211	-	-
(Num.)(WOS)	-0.002048	-0.000856	-0.000722
(Num.)(WS)	-0.002252	-0.000877	-0.000737

Additionally, Figure 3.5 shows the wave system generated by the SUBOFF UV with and without the presence of the support for $F_n = 0.462$ and $h = 1.1D$. In this figure, ψ_{max} is the SUBOFF wake angle, which is defined as the angle enclosed by the line passing through the locations of the the highest peaks inside the UV wake and the $x_0 s z_0$ plane. It is observed that the support has a negligible influence on the wavelength and wake angle since the wavelength and wake angle both are closely related to the dispersion relation, as shown by NOBLESSE et $al.$ [20]. It is further observed that the wake angle of the SUBOFF at this condition is smaller than the classical Kelvin wake angle ,i.e., $\psi_K = 19.47°$, which based on NOBLESSE et $al.$ [20] is attributed to the interference effects between the dominant wave systems inside the UV wake.
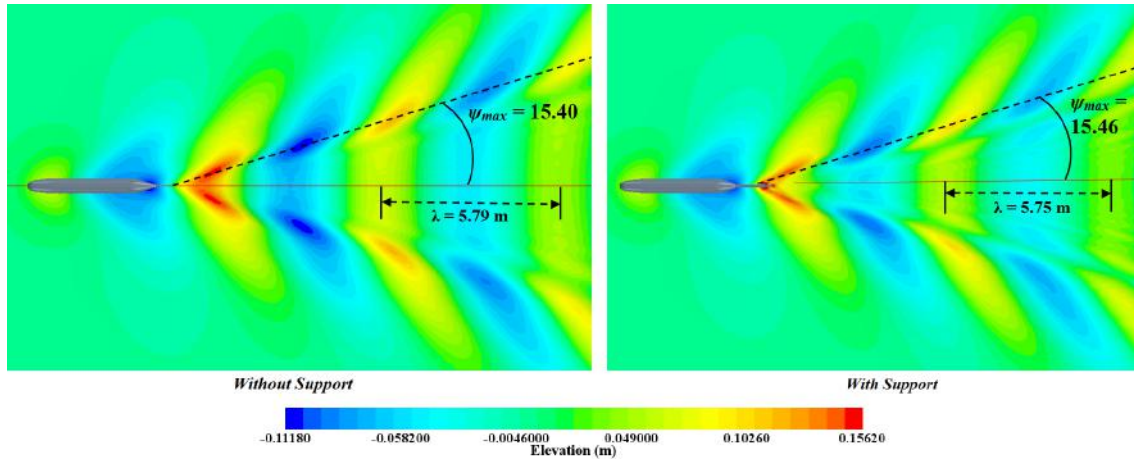
Figure 3.5: SUBOFF-generated wave system for $F_n = 0.462$ and $h = 1.1D$ for the case without the presence of the support (left-hand side) and with the presence of the support (right-hand side)

However, due to the destructive effect of the support on the free surface deformations and local variables and also to evaluate correctly the hydrodynamic forces and moments acting on the SUBOFF, all the simulations in the present study are conducted without the presence of the support.

Chapter 4

Results and Discussion

In this chapter, the results regarding the hydrodynamic forces and moments generated by the velocity components on the UV obtained from the numerical simulations, together with the hydrodynamic coefficients over various submergence depths are presented. Additionally, this chapter provides a detailed analysis of the free surface effect on the hydrodynamics of the SUBOFF axisymmetric UV undergoing steady motions in the horizontal plane. This chapter further presents the results of the dynamic stability of the SUBOFF UV in the horizontal plane along with the maneuvering simulations of the UV for various submergence depths.

4.1 Hydrodynamic forces and moments arising from the velocity components

In this section, first the hydrodynamic forces and moments arising from the velocity components of the UV acting on the SUBOFF in the horizontal plane are presented. In this respect, Figure 4.1 shows the hydrodynamic forces and moments acting on the SUBOFF in the horizontal plane for various UV velocity components and submergence depths.

Figure 4.1 (a) presents the normalized hydrodynamic axial X-force for various axial velocities and submergence depths. Significant increase is observed in the X-force with a decrease in submergence depth, which as is well known arises from the advent of the wave-making resistance component [21]. At the shallowest submergence depth, the oscillatory behavior of the X-force has to do with the interference effects between the dominant wave systems inside the UV wake on the free surface, which is further investigated in the next section.

Additionally, Figures 4.1 (b), (c) and (d) show the normalized hydrodynamic X-force, Y-force and N-moment, respectively, for various lateral velocities and submergence depths. As the UV approaches the free surface, a significant increase is

observed in the hydrodynamic X-force and Y-force over the entire range of lateral velocities. As mentioned earlier, this is due to the advent of the wave-making resistance component [21]. At the shallowest submergence depth, an increase in the lateral velocity gives rise to an increase in the X-force, whereas, at larger submergence depths, increase in this velocity component results in a reduction in the X-force. Moreover, over the entire range of submergence depths, the Y-force increases with respect to the lateral velocity, which is associated with an increase in the pressure difference between the leeward side and windward side of the UV. On the other hand, unlike the X-force and Y-force, a decrease in the submergence depth appears to cause a decrease in the N-moment, especially at large lateral velocities. Moreover, it is observed that unlike other variables, the free surface effect on the N-moment vanishes more rapidly with respect to submergence depth.

In addition, Figures 4.1 (e), (f) and (g) present the normalized hydrodynamic forces and moment for various angular yaw velocities and submergence depths. With a decrease in submergence depth, a significant increase is observed in the values of the X-force, Y-force and N-moment over the entire range of yaw velocities, which is due to the advent of the wave-making resistance component [21]. Over the entire range of submergence depths, while both the Y-force and N-moment increase with respect to the yaw rate, the X-force appears to remain nearly constant with an increase in the r velocity component. Additionally, it is observed that the N-moment arising from the angular yaw velocity, contrary to the N-moment arising from the lateral velocity v, experiences an increase with a decrease in submergence depth.

Note that due to the negligible interference effects between the wave systems generated by the lateral velocity and yaw velocity at points along the SUBOFF length, the hydrodynamic forces and moments arising from these velocity components present no oscillatory behavior with respect to the lateral velocity and angular yaw velocity components, as mentioned correctly in section 2.1.2.
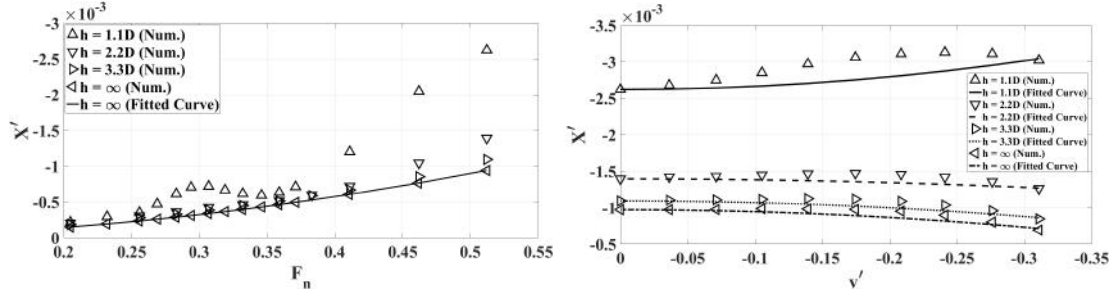
(a) Normalized X-force for various axial velocities and submergence depths

(b) Normalized X-force for various lateral velocities and submergence depths
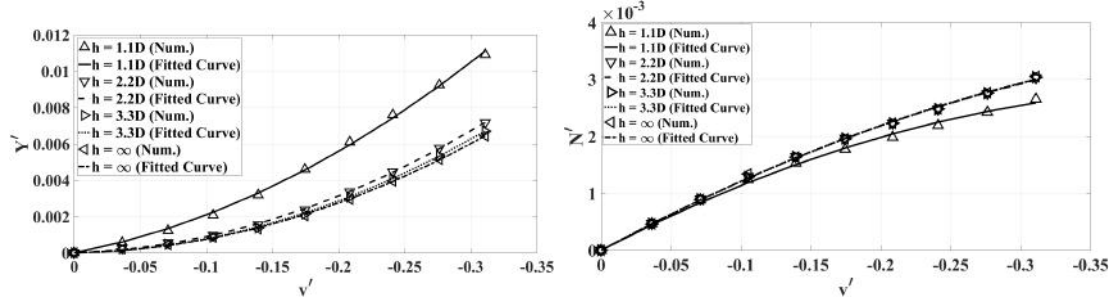
(c) Normalized Y-force for various lateral velocities and submergence depths

(d) Normalized N-moment for various lateral velocities and submergence depths
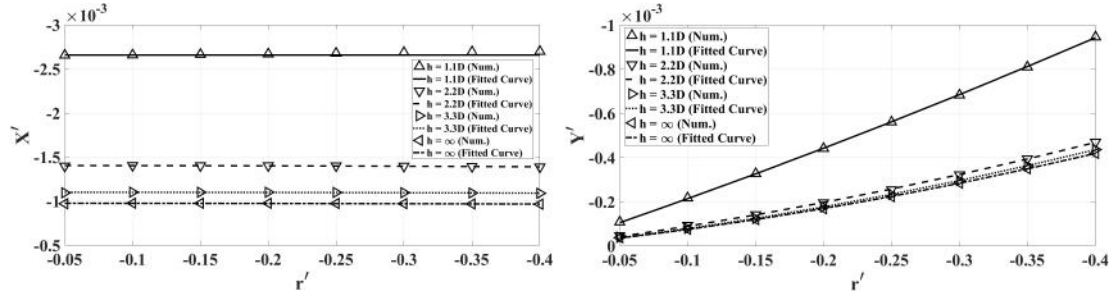
(e) Normalized X-force for various angular yaw velocities and submergence depths

(f) Normalized Y-force for various angular yaw velocities and submergence depths
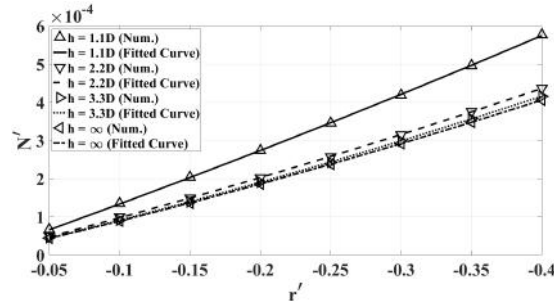
(g) Normalized N-moment for various angular yaw velocities and submergence depths

Figure 4.1: Normalized hydrodynamic forces and moments arising from the velocity components of the UV acting on the SUBOFF in the horizontal plane. The figures also depict the curves used to approximate the hydrodynamic forces and moments in terms of the UV velocity components, i.e., u', v' and r', for various submergence depths.

Furthermore, as the UV travels close to the free surface, the asymmetric dynamic

pressure distribution across the body depth provoked by the nearby self-induced wave system gives rise to the generation of the forces and moments in the vertical plane. In this regard, Figure 4.2 presents the hydrodynamic forces and moments acting on the SUBOFF in the vertical plane for various UV velocity components and submergence depths.

Figures 4.2 (a) and (b) show the normalized vertical Z-force and M-pitching moment, respectively, for various axial velocities and submergence depths. As can be seen, at the shallowest submergence depth, the UV experiences significant Z-force and M-moment. At this depth, the oscillatory behavior of the Z-force and M-moment is due mainly to the interaction between the bow wave and the low-pressure aft shoulder region, as shown by MAALI AMIRI *et al.* [19]. Additionally, over the entire range of axial velocities, the Z-force remains an upward force while the M-moment changes from a bow-down moment to a bow-up one and vice-versa several times. Moreover, for $F_n > 0.4$ the Z-force decreases rapidly and is expected to change from a force acting to draw the UV toward the free surface to a force to pull the hull away from the free surface. Moreover, with an increase in submergence depth, a small upward Z-force, together with a small bow-down M-moment, is exerted on the SUBOFF by the free surface at merely high Froude numbers.

Furthermore, Figures 4.2 (c) and (d) present the normalized vertical Z-force and M-moment, respectively, as a function of sway velocity v' for various submergence depths. At the shallowest submergence depth, both the Z-force and M-moment vary significantly with respect to the lateral velocity component. In this regard, for $|v'| > 0.15$ the Z-force transitions from an upward force to a downward one. In addition, for $|v'| > 0.15$ the M-moment undergoes a consistent decrease with respect to v velocity. Moreover, as can be observed, at large submergence depths, a small upward Z-force, together with a small and approximately constant bow-down M-moment, is exerted on the UV for almost the entire range of v velocity.

Finally, Figures 4.2 (e) and (f) show the normalized vertical Z-force and M-pitching moment, respectively, as a function of yaw velocity r' for various submergence depths. At the shallowest submergence depth, both the Z-force and M-moment undergo a slight decrease with an increase in the yaw rate. It is observed that, at this depth, the Z-force and the M-moment both present a lower level of dependency on the yaw rate compared to the lateral velocity component, as shown in Figures 4.2 (c) and (d). However, at large submergence depths, the Z-force and M-moment remain nearly-constant with respect to the angular yaw velocity component, which is also observed in the behavior of the the Z-force and M-moment with respect to the lateral velocity (see Figures 4.2 (c) and (d)).

Herein, noteworthy is the non-oscillatory behavior of the Z-force and M-moment with respect to the lateral velocity v and the yaw rate r, which is associated with the

negligible interference effects between the wave systems generated by these velocity components at points along the SUBOFF length.
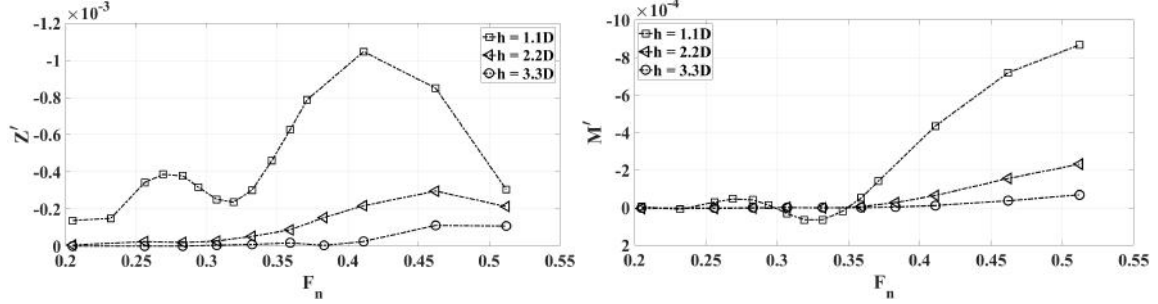
(a) Normalized Z-force for various axial velocities and submergence depths

(b) Normalized M-moment for various axial velocities and submergence depths
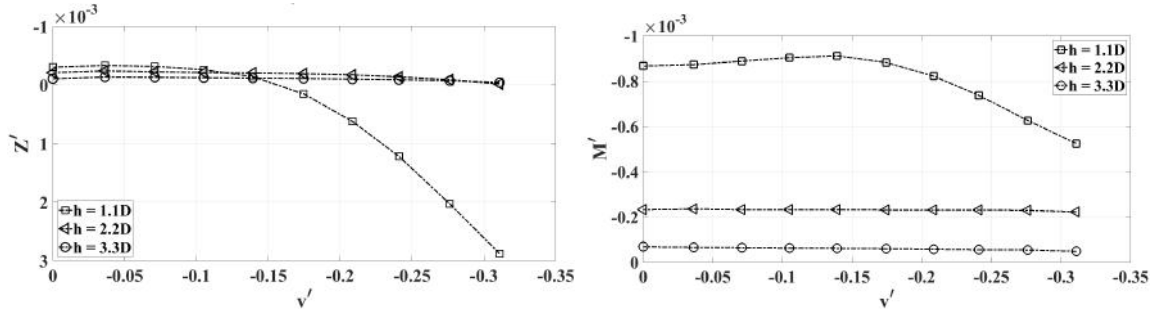
(c) Normalized Z-force for various lateral velocities and submergence depths

(d) Normalized M-moment for various lateral velocities and submergence depths
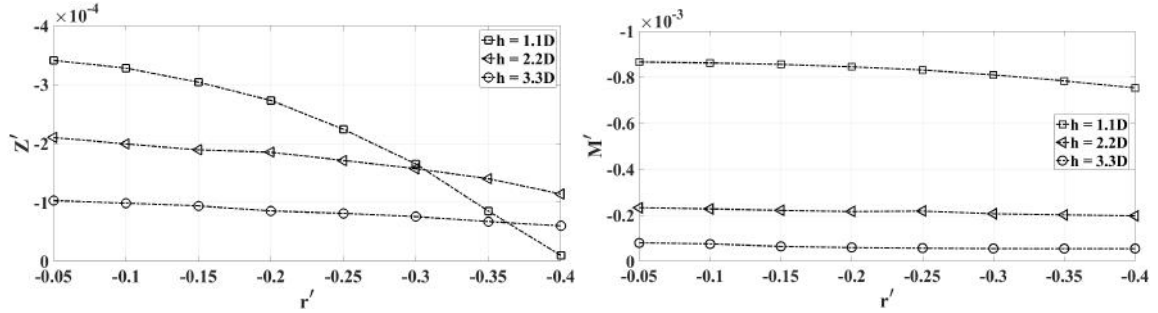
(e) Normalized Z-force for various yaw rates and submergence depths

(f) Normalized M-moment for various yaw rates and submergence depths

Figure 4.2: Normalized hydrodynamic forces and moments acting on the SUBOFF in the vertical plane for various velocity components and submergence depths.

Based on Figures 4.1 and 4.2, significant interaction is observed between the UV and the free surface at the shallowest submergence depth. Generally, a decrease in the submergence depth gives rise to an increase in almost all the forces and moments except for the N-moment arising from the lateral velocity, which unlike the other forces and moments undergoes a reduction. Additionally, it is observed that the free surface effect on the hydrodynamic forces and moments diminishes drastically with an increase in submergence depth. In this regard, based on DAWSON [10], the interaction between the free surface and the UV hull reduces exponentially with respect to submergence depth. Accordingly, as mentioned by DAWSON [10], this

interaction is negligible for $\frac{h}{D} > 3$ and completely vanishes for $\frac{h}{D} > 5$.

In the next section, the mechanism by which the free surface affects the hydrodynamics of a shallowly submerged UV is addressed. In this respect, the origin of the behavior of the forces and moments acting on the SUBOFF in the horizontal plane with respect to the UV velocity components and submergence depth is investigated in more detail.

4.2 A detailed analysis of the free surface effect on the hydrodynamics of the SUBOFF UV

In the previous section, it is observed that generally the forces arising from the velocity components of the UV undergo an increase with a decrease in submergence depth. Based on NEWMAN [21], the increase in the hydrodynamic forces as the UV approaches the free surface has to do with the advent of the wave-making resistance component.

Likewise, as shown by MAALI AMIRI *et al.* [19], the increase in the hydrodynamic forces as the UV approaches the free surface can also be associated with the free surface effect on the dynamic pressure distribution around the UV. Accordingly, the crests and troughs of the self-induced wave system of a shallowly submerged UV modify the dynamic pressure distribution around the UV hull by creating local regions of high and low dynamic pressure, respectively, along the UV hull. To further explain this, consider Figures 4.3 (a) and (b), which show the dynamic pressure distribution around the SUBOFF at $F_n = 0.256$ for two submergence depths $h = \infty$ and $h = 1.1D$. As can be inferred from Figures 4.3 (a) and (b), the local regions of high and low dynamic pressure associated with the crests and troughs of the generated wave system modify the dynamic pressure distribution around the UV hull. This modification of the pressure distribution induced by the deformations of the nearby flexible free surface is largely responsible for the behavior of the hydrodynamic forces as the UV approaches the free surface.
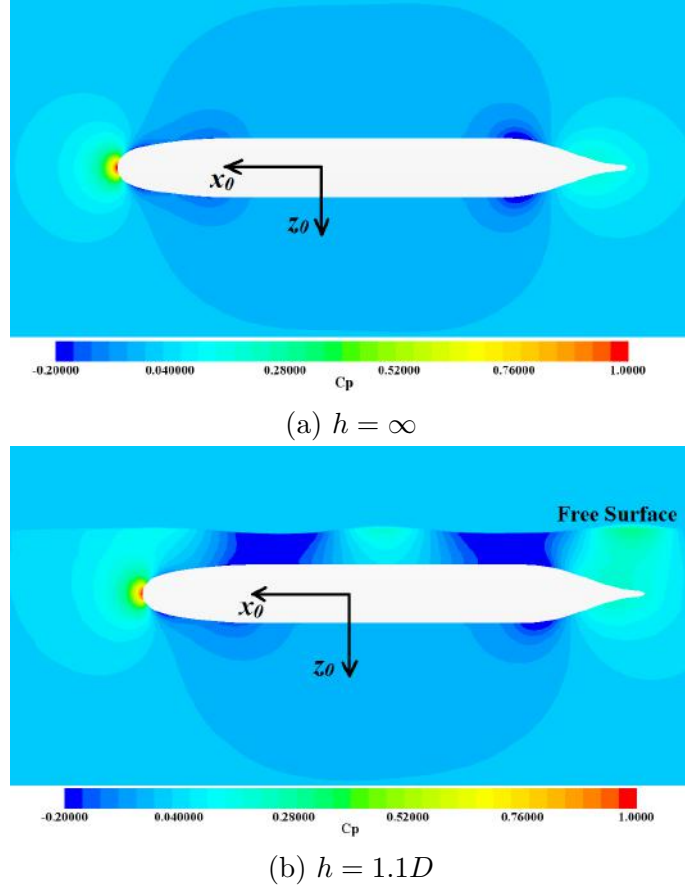
(a) $h = \infty$

(b) $h = 1.1D$

Figure 4.3: Dynamic pressure distribution around the SUBOFF for $F_n = 0.256$ over two different submergence depths $h = 1.1D$ and $h = \infty$

Thus, herein, to investigate how the free surface affects the hydrodynamics of a UV performing steady motions in the horizontal plane, the dynamic pressure distributions around the SUBOFF, together with the forces and moments acting on the UV hull, are closely analyzed over various submergence depths and UV velocity components.

However, before proceeding to investigate the free surface effect on the hydrodynamics of the SUBOFF UV undergoing steady motions in the horizontal plane, it is important to have an overview of several dominant features of the fluid flow around the totally submerged SUBOFF UV at zero incidence traveling with a constant axial speed along a straight path, as shown in Figure 4.3 (a).

The pressure at the bow is the well known stagnation pressure, which is the highest local pressure value experienced by the UV. Moreover, due to the separation of the fluid flowing over the stern, the pressure in this region is only partially recovered. Furthermore, the dynamic pressure of the fluid flowing around the SUBOFF undergoes a reduction in both aft and fore shoulders with more reduction occurring over the aft shoulder region due to a larger hull curvature.

A good knowledge of these basic flow features around the totally submerged

84

SUBOFF at zero incidence is extremely helpful for better understanding of the hydrodynamic behavior of the shallowly submerged UV at steady drift or rotational motion. Since the axial velocity component consistently has the largest magnitude among the velocity components of the UV during the steady drift and rotational motions in the horizontal plane.

4.2.1 Free surface effect on the hydrodynamics of the SUB-OFF UV undergoing a straight-ahead steady motion

In this section, to evaluate the free surface effect on the hydrodynamics of the SUBOFF UV undergoing a straight-ahead steady motion, a detailed analysis is conducted to investigate the origin of the behavior of the X-force with respect to the axial velocity u over various submergence depths, as shown in Figure 4.1 (a). Further information on the origin of the behavior of the Z-force and M-moment arising from the axial velocity acting on the SUBOFF UV in the vertical plane (Figures 4.2 (a) and (b)) can be found in MAALI AMIRI *et al.* [19].

Origin of the behavior of the X-force with respect to the axial velocity u

As mentioned earlier, the increase in the X-force with a decrease in submergence depth can also be explained through the effect of the free surface deformations on the dynamic pressure distribution along the length of the UV hull.

In this regard, Figure 4.4 presents the contribution of two components, frictional and pressure, to the total X-force at two submergence depths $h = 1.1D$ and $h = \infty$ for Froude numbers ranging from $F_n = 0.205$ to $F_n = 0.512$. As can be inferred from this figure, while the free surface effect on the frictional component is nearly-negligible, it has a remarkable effect on the pressure component of the X-force. The small increase in the frictional component with a decrease in submergence depth, as explained by MAALI AMIRI *et al.* [19], can be attributed to an increase in the fluid flow velocity between the free surface and the body, as the submergence depth decreases.

As shown in Figure 4.4, at $h = 1.1D$, due to interference between the dominant wave systems inside the UV wake the curve of the pressure component exhibits an oscillatory behavior with respect to Froude number, i.e., it exhibits humps and hollows (NEWMAN [21], LEWIS [3] and MOLLAND *et al.* [49]). As is well-known, hump occurs when the waves are in phase (reinforcement), while hollow occurs when the waves are out of phase (cancellation). Based on Figure 4.4, the reinforcement or cancellation of the wave systems are accompanied by an increase or decrease in the pressure component of the X-force, respectively.

The reinforcement and cancellation of the wave systems at $h = 1.1D$ can also be
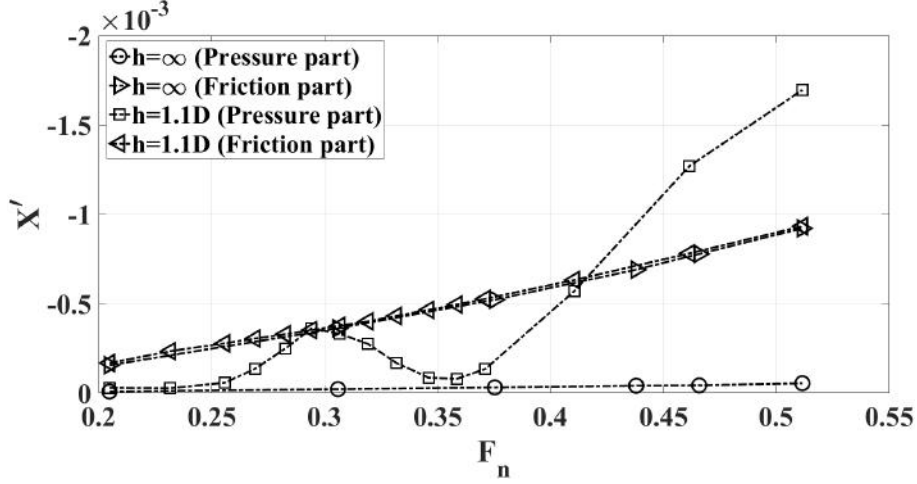
Figure 4.4: Contribution of two components, frictional and pressure, to the total X-force of the SUBOFF at two submergence depths $h = 1.1D$, ∞ for Froude numbers ranging from $F_n = 0.205$ to $F_n = 0.512$

observed in Figure 4.5, which represents the behavior of the normalized maximum height of the SUBOFF-generated wave system for Froude numbers and submergence depths ranging from $F_n = 0.205$ to $F_n = 0.512$, and from $h = 1.1D$ to $h = 3.3D$, respectively. The normalization of the maximum wave height is carried out using the maximum diameter of the SUBOFF bare hull D. As can be inferred from Figures 4.1 (a) and 4.5, at the shallowest submergence depth, the reinforcement or cancellation of the wave systems at hump or hollow leads to an increase or decrease in the wave height, which is equivalent to an increase or decrease in the energy imparted by the UV to the surrounding fluid (NEWMAN [21]).
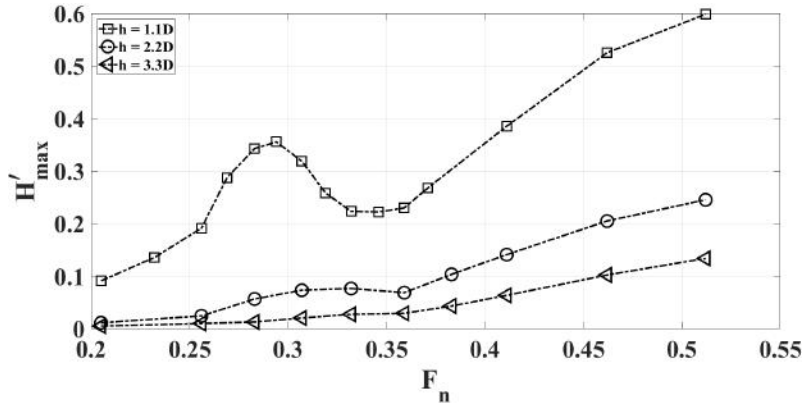
Figure 4.5: Calculated normalized maximum wave height (H'_{max}) of the SUBOFF wave system in a range of submergence depths and Froude numbers from $h = 1.1D$ to $h = 3.3D$ and from $F_n = 0.205$ to $F_n = 0.512$, respectively

As is well known, the positive and negative dynamic pressure peaks around the UV hull are the main contributors to the UV-generated wave system on the free surface [49]. Accordingly, in case of the SUBOFF UV, the dominant wave systems

86

inside the UV wake are generated by the bow, stern and aft shoulder. This can be inferred from Figure 4.6, which shows the pressure distribution along the length of the totally submerged SUBOFF for $F_n = 0.46$ measured experimentally by HUANG e LIU [44] and calculated numerically from the present simulations. The uncertainty in the measurement of the pressure coefficients is estimated to be within ± 0.015. The bow and stern waves, due to a positive peak pressure, start with a crest; while, the aft shoulder wave, due to a negative peak pressure, starts with a trough.
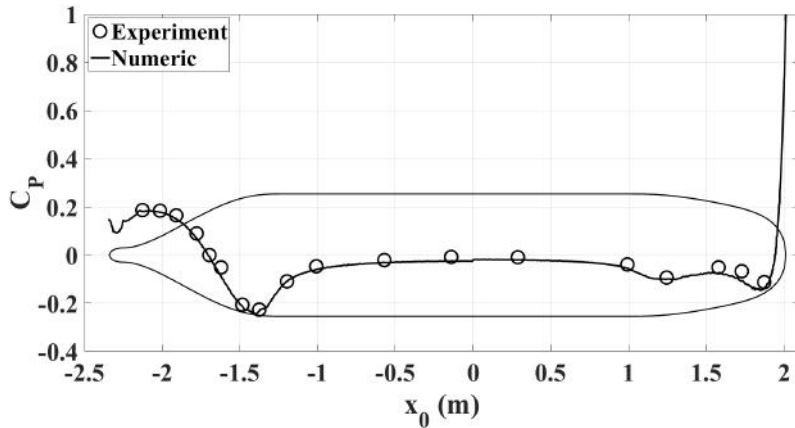

Figure 4.6: Pressure distribution along the length of the totally submerged SUBOFF for $F_n = 0.462$ measured experimentally by HUANG e LIU [44] and calculated numerically from the present simulations

In naval architecture, the analysis of interference between the dominant wave systems for identifying the humps and hollows is typically conducted between a bow wave crest and a stern wave trough (NOBLESSE et al. [20]). This originates from the potential flow theory, where it has been a common practice, and indeed a powerful approach, to represent a ship hull via distributions of sources and sinks over the bow and stern regions, respectively (NEWMAN [21]).

However, in case of the UV hulls, as can be inferred from Figure 4.6, although the local pressure value at the stern and aft shoulder regions are approximately equal, the aft shoulder operates in a closer proximity to the free surface compared to the stern; thus, it is surmised that interference between the bow and aft shoulder waves may have a more dominant effect on the behavior of the X-force, compared to interference between the bow and stern waves.

Herein, to investigate whether the interaction between the bow and aft shoulder waves or the interaction between the bow and stern waves has a more dominant effect on the behavior of the X-force, an elementary analysis of interference between the dominant wave systems, i.e., bow, stern and aft shoulder waves, is carried out at hump and hollow Froude numbers.

In this regard, as can be inferred from Figure 4.6, the negative peak pressure in the aft shoulder region is located at the axial location of $x_0/L = -0.318$ (at

the distance of $0.78L$ from the nose); thus, it is considered as the origin of the aft shoulder wave trough.

From Figure 4.4 it can be inferred that at $h = 1.1D$ the hump in the pressure component of the X-force occurs at $F_n = 0.294$. At this Froude number, based on Equation 2.21 for $\Theta = 0$, the bow generates a wave of normalized length equal to $\lambda/L = 0.54$. Thus, the bow wave trough is nearly on the aft shoulder wave trough. As a result, the hump in the curve of the pressure component of the X-force at this Froude number may be a consequence of constructive interference between the bow and aft shoulder waves.

To investigate further this hypothesis, Figure 4.7 demonstrates the centerline free surface profiles and the dynamic pressure distributions along the top of the SUBOFF at $h = 1.1D$ for Froude numbers ranging from $F_n = 0.269$ to $F_n = 0.332$.
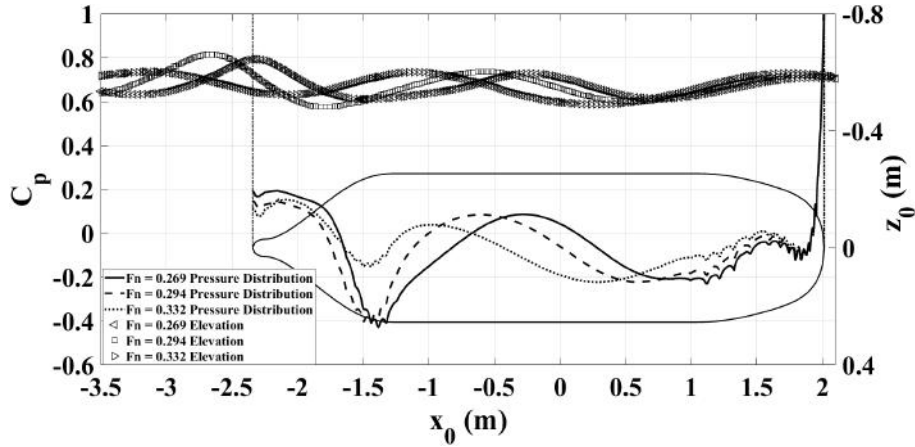

Figure 4.7: Centerline free surface profiles and the pressure distributions along the top of the SUBOFF at $h = 1.1D$ for Froude numbers ranging from $Fn = 0.269$ to $Fn = 0.332$

As can be observed in Figure 4.7, at $F_n = 0.269$ the bow-generated wave has a normalized length equal to $\lambda/L = 0.46$; thus, the bow wave crest is nearly on the stern wave crest, and in spite of constructive interference between the bow and stern waves, the hump has not occurred. This is due mainly to the increased pressure exerted at the stern, which decreases the pressure differential between the fore and aft parts of the UV.

On the other hand, based on Figure 4.7, at $F_n = 0.294$ the bow wave trough is on the aft shoulder wave trough, which is accompanied by a decrease in the pressure exerted on the aft region and, consequently, results in an increase in the pressure difference between the fore and aft parts of the UV.

Finally, according to Figure 4.7, at $F_n = 0.332$, the bow-generated wave has a normalized length equal to $\lambda/L = 0.69$. Thus, the bow wave crest is close to the aft shoulder region and, as a consequence, the pressure in the aft region of the UV

increases, which results in a decrease in the pressure differential between the fore and aft parts of the UV.

Moreover, from Figure 4.4 it can be inferred that at $h = 1.1D$ the hollow in the pressure component of the X-force occurs at $F_n = 0.359$. At this Froude number, the bow creates a wave of normalized length $\lambda/L = 0.81$. Thus, the bow wave crest is approximately on the aft shoulder wave trough. Accordingly, the hollow in the curve of the pressure component of the X-force at this Froude number may be a consequence of destructive interference between the bow and aft shoulder waves.

In this respect, Figure 4.8 shows the centerline free surface profiles and the dynamic pressure distributions along the top of the SUBOFF at $h = 1.1D$ for Froude numbers ranging from $F_n = 0.319$ to $F_n = 0.411$.

It can be clearly seen that at $F_n = 0.359$ the coincidence of the bow wave crest with the aft shoulder wave trough leads to a considerable reduction in the free surface deformation and is responsible for the increased pressure exerted at the aft region of the UV; this, consequently, decreases the pressure differential between the fore and aft parts of the UV.
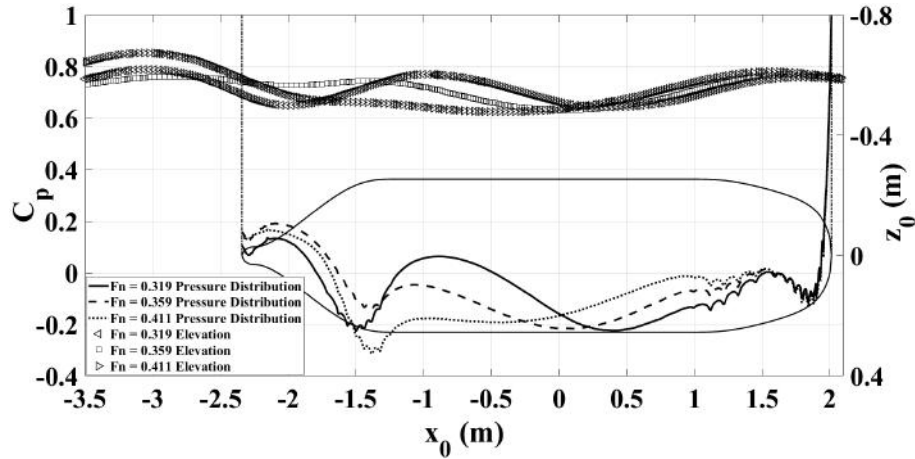
Figure 4.8: Centerline free surface profiles and the pressure distributions along the top of the SUBOFF at $h = 1.1D$ for Froude numbers ranging from $F_n = 0.319$ to $F_n = 0.411$

The discussion given above shows that, in case of the shallowly submerged UVs, the humps and hollows in the curve of the X-force arising from the axial velocity component (resistance force) are a consequence of the interference effects between the bow and aft shoulder waves, rather than between the bow and stern waves, which is usually considered in naval architecture. This is due mainly to the closer proximity of the aft shoulder to the free surface, which consequently contributes more to the UV-generated wave system, compared to the stern.

4.2.2 Free surface effect on the hydrodynamics of the SUB-OFF UV undergoing a steady drift motion

In this section, to evaluate the free surface effect on the hydrodynamics of the SUBOFF UV undergoing a steady drift motion, a detailed analysis is conducted to investigate the origin of the behavior of the X-force, Y-force and N-moment with respect to the lateral velocity v acting on the SUBOFF over various submergence depths, as shown in Figures 4.1 (b), (c) and (d).

Origin of the behavior of the X-force with respect to the lateral velocity v

The X-force component acting on the UV at a steady drift angle β can be interpreted as the resistance force exerted on the SUBOFF hull due to the axial velocity component $u = U.\cos\beta$ in x_0-direction.

In the totally submerged case, a reduction in the u velocity component (,i.e., an increase in the lateral velocity v) gives rise to a reduction in the resistance force in x_0-direction, which is in agreement with the behavior of the X-force with respect to the lateral velocity v in the totally submerged condition (Figure 4.1 (b)).

As is well known from NEWMAN [21], in the shallowly submerged case, the wave-making resistance component emerges as an additional contributor to the resistance force acting on the UV hull. The effect of the wave-making resistance can be clearly identified at the shallowest submergence depth in Figure 4.1 (b), which results in a significant increase in the X-force as the UV approaches the free surface. Furthermore, as can be inferred from Figure 4.1 (b), at the shallowest submergence depth, contrary to the totally submerged case, an increase in the lateral velocity v leads to an almost consistent increase in the X-force.

To explain the increase in the X-force with respect to v at the shallowest submergence depth, consider Figure 4.9 depicting the normalized maximum wave height of the SUBOFF-generated wave system at $F_n = 0.512$ over lateral velocities and submergence depths ranging from $v' = 0$ to $v' = -0.31$ and from $h = 1.1D$ to $h = 3.3D$, respectively. The normalization of the wave height is carried out by using the maximum diameter of the UV. As can be inferred from Figures 4.9 and 4.1 (b), at the shallowest submergence depth, a qualitative correlation exists between the behavior of the X-force and the maximum wave height curves. Therefore, it is very likely that the increase in the X-force with respect to lateral velocity is due to an increase in the imparted energy by the UV to elevate more the free surface [21], which gives rise to an increase in the wave-making resistance component.
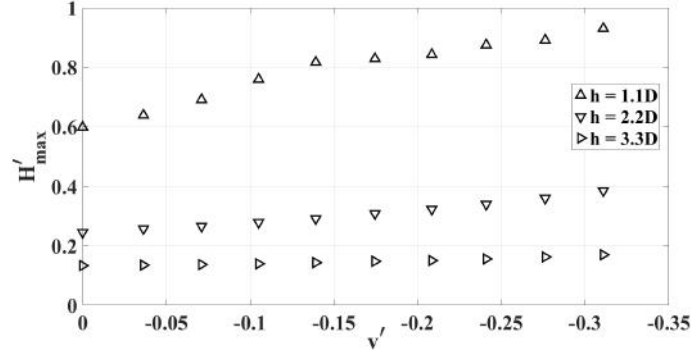
Figure 4.9: Normalized maximum wave height of the SUBOF-generated wave system at $F_n = 0.512$ over lateral velocities and submergence depths ranging from $v' = 0$ to $v' = -0.31$ and from $h = 1.1D$ to $h = 3.3D$

Although the overall speed U of the UV remains unchanged, the maximum wave height shows a considerable degree of dependency on the lateral velocity. As can be seen in Figure 4.9, the maximum wave height increases with an increase in the lateral velocity, especially at the shallowest submergence depth.

The reason for the increase in the maximum wave height with respect to the lateral velocity is associated with the effect of the leeward vortical flow structure. In other words, due to a drop in the dynamic pressure in the core of the vortical structure, the free surface above this vortical structure is subject to depress, which can be a possible reason for the increase in the maximum wave height with respect to the lateral velocity. In this regard, Figure 4.10 shows the SUBOFF-generated wave system for $h = 1.1D$ and $F_n = 0.512$ over two lateral velocities $v' = 0$ and $v' = -0.31$. As can be seen in this figure, at $v' = -0.31$, the maximum depression of the free surface is nearly on the leeward stern region, where the vortical flow structure is strongest.

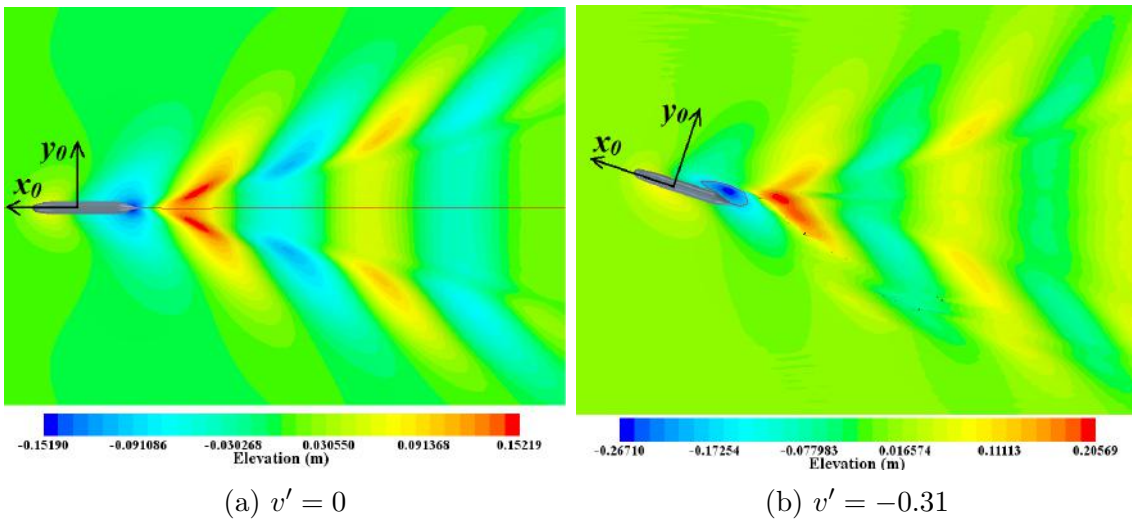

(a) $v' = 0$ (b) $v' = -0.31$

Figure 4.10: SUBOFF-generated wave system at submergence depth $h = 1.1D$ and $F_n = 0.512$ over two lateral velocities $v' = 0$ and $v' = -0.31$

The coincidence of the maximum depression of the free surface close to the UV hull with the leeward vortical flow structure can be further observed in Figure 4.11. This figure depicts the free surface profile together with vorticity magnitude around the SUBOFF at $v' = -0.31$ over two axial locations $x_0 = -0.6006\ m$ and $x_0 = -1.9074\ m$ for two submergence depths $h = 1.1D$ and $h = 2.2D$.

(a) $h = 1.1D$

(b) $h = 2.2D$
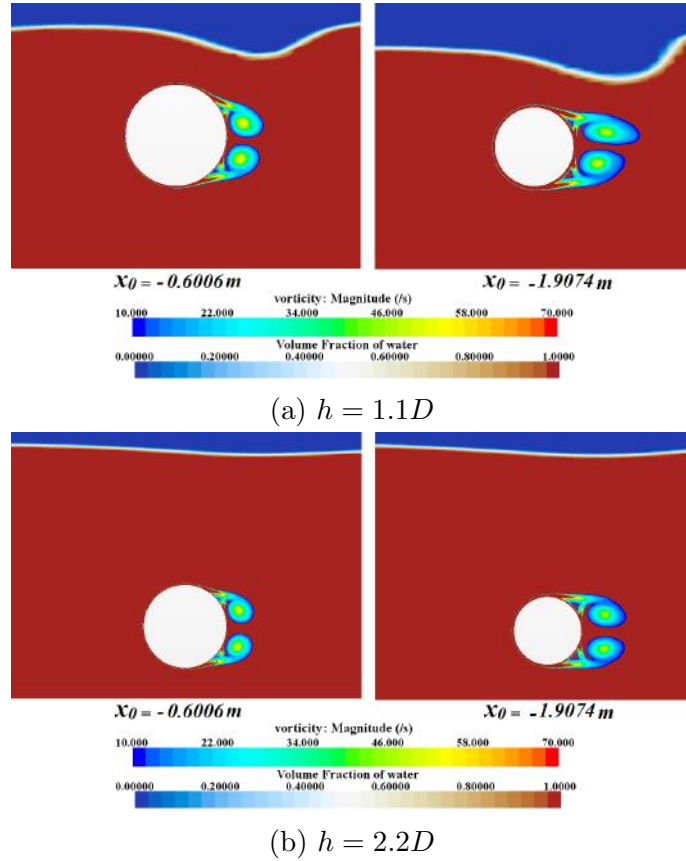
Figure 4.11: Free surface profile and vorticity magnitude at $v' = -0.31$ over two axial locations $x_0 = -0.6006\ m$ and $x_0 = -1.9074\ m$ and two submergence depths $h = 1.1D$ and $h = 2.2D$

In this regard, the growth of the leeward vortical flow structure with respect to the lateral velocity v ([25], [54] and [55]) gives rise to a more reduction in the dynamic pressure in the leeward side, which accordingly results in a more depression of the free surface. The more depression of the free surface signifies an increase in the X-force due to an increase in the wave-making resistance component. However, based on Figures 4.9, and 4.11, at large submergence depths, the influence of the vortical structure on the free surface elevation diminishes drastically.

Origin of the behavior of the Y-force and N-moment with respect to the lateral velocity v

The Y-force arising from the lateral velocity component can be interpreted as the resistance force exerted on the UV hull in y_0 direction. This force component emanates from the asymmetric dynamic pressure distribution around the UV developed from the windward side toward the leeward side at a drift angle. In addition, the N-moment is the moment generated by the Y-force about z_0-axis of the UV.

As can be seen in Figure 4.1 (c), in the totally submerged case, an increase in the lateral velocity component results in an increase in the Y-force component. As is well known, the increase in the Y-force component with respect to v is attributed to a growing pressure differential between the windward and leeward sides. In this regard, Figure 4.12 shows the dynamic pressure distribution around the totally submerged SUBOFF UV at the axial location of $x_0 = -1.0362\,m$ for lateral velocities ranging from $v' = 0$ to $v' = -0.31$. As can be inferred from this figure, a growing pressure differential is developed from the windward side toward the leeward side with respect to the lateral velocity, which has to do with the crossflow separation getting stronger. In this vein, the core of the leeward vortical flow structure can be clearly identified for $|v'| > 0.17$, which is the circles of negative pressure formed at the leeward side.
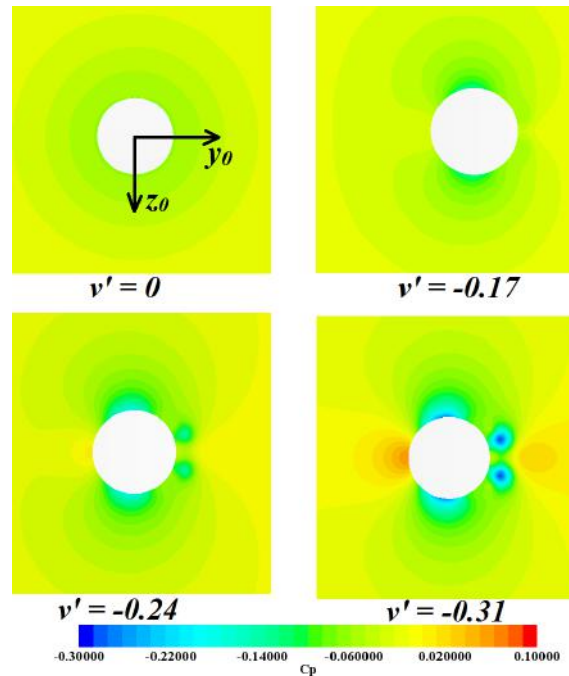

Figure 4.12: Dynamic pressure distribution around the totally submerged SUBOFF UV at the axial location of $x_0 = -1.0362\,m$ for lateral velocities ranging from $v' = 0$ to $v' = -0.31$

Additionally, with a decrease in submergence depth the Y-force increases remark-

ably, which is attributed to the advent of the wave-making resistance component. To investigate more closely the behavior of the Y-force over various submergence depths, Figure 4.13 shows the distribution of this force component along the SUBOFF length at $v' = -0.31$ over various submergence depths.
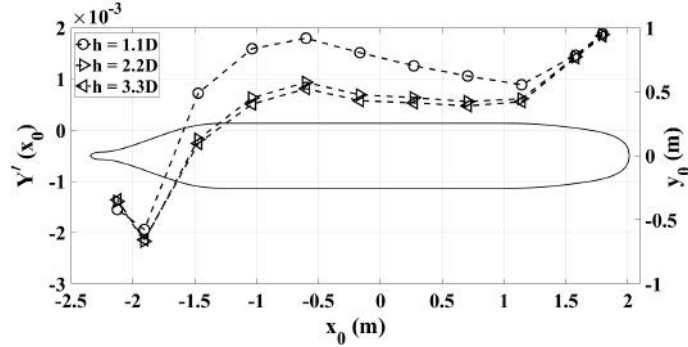
Figure 4.13: Distribution of the Y-force resulting from the lateral velocity v along the SUBOFF length at $v' = -0.31$ over various submergence depths

As the SUBOFF has a negative lateral velocity $v' = -0.31$, it is expected that all the stations along the UV length generate a positive lateral force. However, it is seen that a negative lateral force is generated at the stern region of the SUBOFF over the entire range of submergence depths. To investigate the reason for this behavior, Figure 4.14 shows the dynamic pressure distribution in $x_0 s y_0$ plane around the SUBOFF at $v' = -0.31$ for various submergence depths.
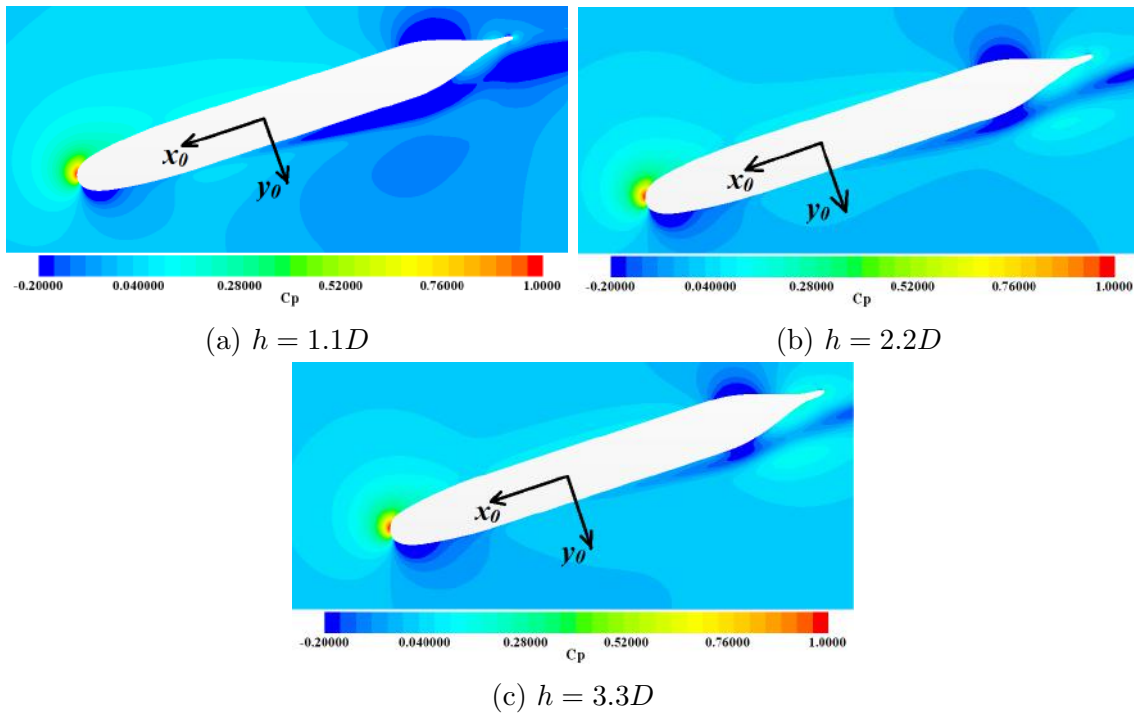

(a) $h = 1.1D$

(b) $h = 2.2D$

(c) $h = 3.3D$

Figure 4.14: Dynamic pressure distribution in $x_0 s y_0$ plane around the SUBOFF at $v' = -0.31$ for various submergence depths

94

From the pressure distributions presented in Figure 4.14, five common things over the whole range of submergence depths stand out. First is the shift of the bow stagnation point toward the windward side due to the lateral velocity component. Secondly, this shift causes both an increase in the dynamic pressure at the windward forward shoulder and a decrease in the dynamic pressure at the leeward bow region. Third is the drop in the dynamic pressure at the windward aft shoulder, which is attributed to an increase in the velocity of the fluid flowing at this region. Fourth is the leeward shift of the aft stagnation region, which is caused by the drop in the dynamic pressure at the windward aft shoulder. Finally, fifth is the drop in the dynamic pressure at the leeward aft region caused by the leeward vortical flow structure. However, noteworthy is the departure of the low-pressure region associated with the leeward vortical flow structure from the body surface at the stern, which indicates that this low-pressure region does not remain attached to the UV surface downstream the aft shoulder. This is due mainly to the shape of the stern of the SUBOFF, which is rapidly tapered at this region. Accordingly, as a result of this tapering at the stern, the leeward low-pressure vortical flow structure, which remains parallel to the UV centerline (PHILLIPS *et al.* [54]), departs from the body surface at the stern region.

Therefore, as can be seen in Figure 4.14, the decrease in the pressure at the windward aft shoulder region, together with the leeward shift of the aft stagnation region is responsible for the windward suction Y-force exerted over the stern region of the SUBOFF.

Another worthy to note consideration in Figure 4.14 is the concurrent decrease in the dynamic pressure both at the leeward aft region and the stern region as the UV approaches the free surface. This is attributed to the depression of the free surface above these regions, as shown in Figure 4.10 (b), which consequently reduces the dynamic pressure at these regions.

Aside from the stern region, based on Figure 4.13, the rest of the SUBOFF UV hull experiences a positive lateral force. At large submergence depths, the largest magnitude of the Y-force is generated by the bow region, where the stagnation pressure is located. However, at the shallowest submergence depth, significant increase is observed in the lateral force values, especially at the region between the fore and aft shoulders. The increase in the Y-force in this region with a decrease in submergence depth can be associated with an increase in the dynamic pressure difference between the windward and leeward sides as the UV approaches the free surface. This increase in the pressure differential can be clearly observed in Figure 4.14. To further establish a relationship between the pressure distribution and the behavior of the Y-force, Figure 4.15 presents the dynamic pressure distribution around the SUBOFF at $v' = -0.31$ over axial locations and submergence depths ranging from

$x_0 = 1.5774\ m$ to $x_0 = -1.9074\ m$ and from $h = 1.1D$ to $h = 3.3D$, respectively.

(a) $h = 1.1D$ (b) $h = 2.2D$

(c) $h = 3.3D$
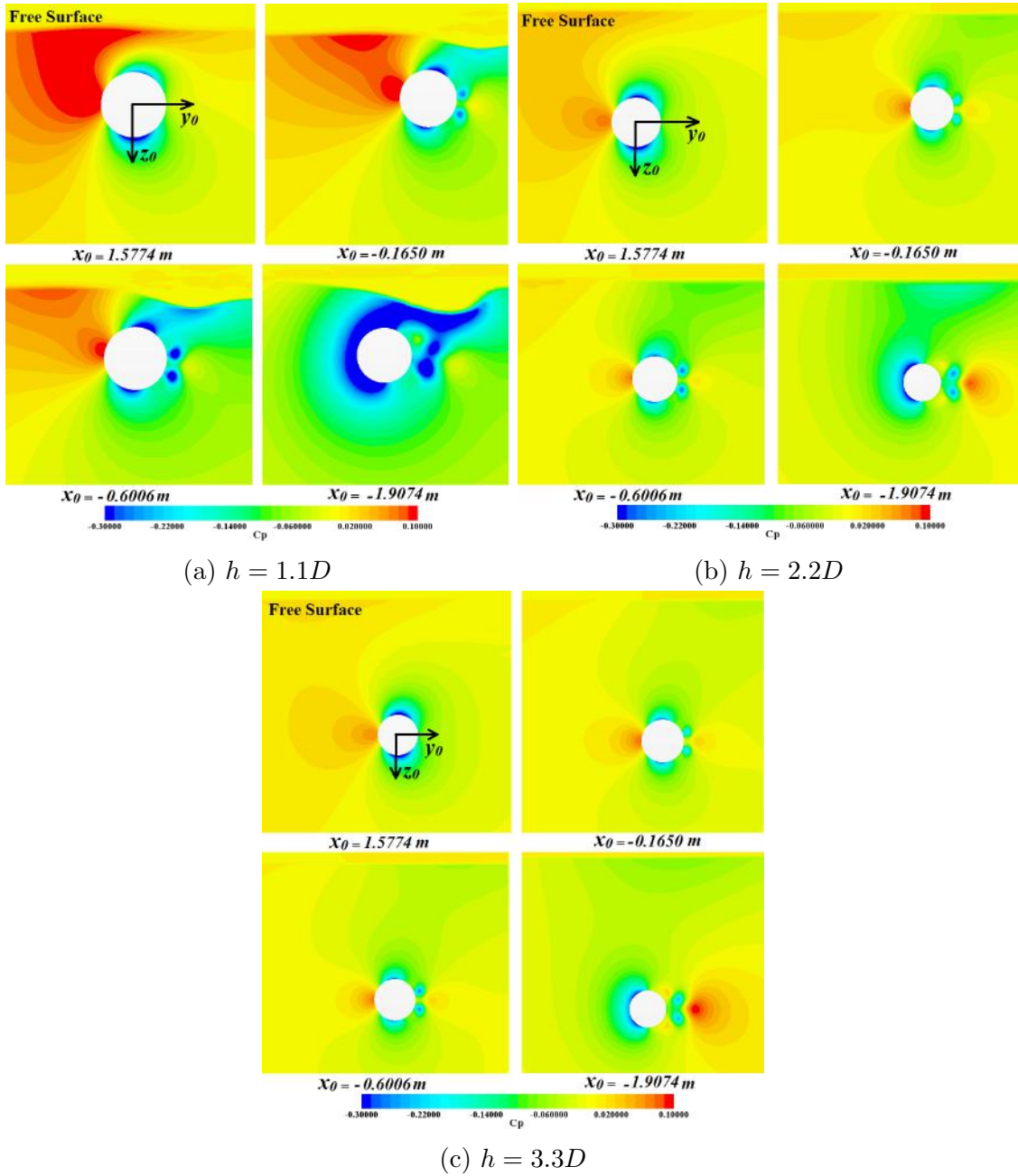
Figure 4.15: Dynamic pressure distribution around the SUBOFF at $v' = -0.31$ over axial locations and submergence depths ranging from $x_0 = 1.5774\ m$ to $x_0 = -1.9074$ m and from $h = 1.1D$ to $h = 3.3D$, respectively

As can be inferred from Figures 4.14 and 4.15, the rising of the free surface above the windward stagnation point together with the depression of the free surface above the leeward vortical flow structure causes more increase and decrease in the local dynamic pressure values at the windward and leeward sides, respectively. This, consequently, leads to an increase in the dynamic pressure difference between the windward and leeward sides and, as a result, increases the Y-force. In other words,

the less the submergence depth, the more will be the free surface deformations and this, accordingly, gives rise to a more increase in the Y-force.

Note that, based on Figure 4.15, the pressure distribution at $x_0 = -1.9074 \ m$ over various submergence depths sheds more light on the explanation given earlier for the negative lateral force acting on the stern region.

On the other hand, the N-moment resulting from the lateral velocity component is the only variable that reduces with a decrease in submergence depth. In order to have a good understanding of the behavior of the N-moment, the distribution of this variable along the length of the SUBOFF UV can provide useful information. In this regard, Figure 4.16 shows the distribution of the N-moment along the length of the SUBOFF at $v' = -0.31$ over various submergence depths. Noteworthy is the largest magnitude of the N-moment along the SUBOFF length, which is generated by the negative Y-force at the stern. Significant contribution is also observed from the bow region where the stagnation pressure is located.
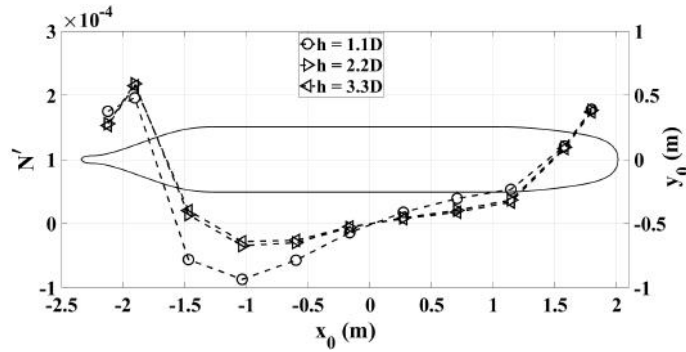
Figure 4.16: Distribution of the N-moment generated by the lateral velocity v along the SUBOFF length at $v' = -0.31$ over various submergence depths

As can be inferred from Figure 4.16, the decrease in the N-moment as the UV approaches the free surface is due mainly to an increase in the positive Y-force acting on the aft region, which produces a negative N-moment. This, consequently, gives rise to a decrease in the total N-moment, which is positive, as the submergence depth is decreased.

The results presented in this section demonstrate the crucial effect of the stern region on the Y-force and N-moment arising from the sway velocity v acting on the SUBOFF over various submergence depths. It is observed that for the entire range of submergence depths an unexpected Y-force in the opposite direction of the total Y-force is generated over the stern of the SUBOFF, which gives rise to an increase in the total N-moment acting on the UV.

The results further show that approaching the free surface has negligible effect on the Y-force and N-moment generated by the stern and bow regions. In this regard, with a decrease in submergence depth, the region between the UV midlength and

the aft shoulder is mainly responsible for the concurrent increase in the Y-force and decrease in the N-moment. This is attributed to a growing pressure difference between the windward and leeward sides as the UV approaches the free surface. Accordingly, in the region between the midlength and the aft shoulder, the rising of the free surface above the windward stagnation point, together with the depression of the free surface above the leeward low-pressure region created by the crossflow gives rise to more increase and decrease in the local dynamic pressure values at the windward and leeward sides, respectively. This, consequently, gives rise to an increase in the pressure difference between the windward and leeward sides, which results in an increase in the Y-force while a decrease in the N-moment as the UV approaches the free surface. Since the region between the UV midlength and the aft shoulder generates a Y-force in the same direction of the total Y-force while it induces an N-moment in the opposite direction of the total N-moment.

The obtained results also show a significant interaction between the low-pressure region created by the leeward vortical flow structure and the free surface. As a result of this interaction, the leeward vortical flow structure affects remarkably the forces and moments exerted on a shallowly submerged UV at moderate drift angles. Several crucial effects of the leeward vortical flow structure can be summarized as follows:

- At the shallowest submergence depth, the growth of the leeward vortical flow structure with an increase in the lateral velocity causes more depression in the free surface, which consequently increases the X-force component due to an increase in the wave-making resistance component.

- At the shallowest submergence depth, the depression of the free surface above the leeward vortical flow structure causes a more decrease in the local dynamic pressure value at the leeward side, which is partially responsible for the increase in the Y-force. Additionally, as the increase in the Y-force occurs mainly in the aft region, where the leeward vortical structure is formed, the N-moment exerted on the hull undergoes a reduction with a decrease in submergence depth.

4.2.3 Free surface effect on the hydrodynamics of the SUB-OFF UV undergoing a steady turning motion

In this section, the origin of the behavior of the forces and moment arising from the yaw angular velocity component acting on the shallowly submerged SUBOFF over various submergence depths is investigated. It is worthy to mention that this investigation is restricted to the Y-force and N-moment, as the behavior of the X-force with respect to r and h can be explained in the same manner as that used to explain the behavior of the X-force with respect to the lateral velocity v and h.

Origin of the behavior of the Y-force and N-moment with respect to the yaw angular velocity component r

As mentioned in section 2.2.2, when an angular yaw velocity r is imposed over the SUBOFF UV, a linear distribution of lateral velocity v is developed along the body length. As a result, every point along the length of the SUBOFF experiences a specific drift angle with the largest local drift angle occurring at the extreme end of the stern. In this regard, considering the maximum rotational velocity used in the current study, the maximum local drift angle at the extreme end of the stern is obtained at $r' = -0.4$, which is $-12.14°$ degrees. Accordingly, Figure 4.17 shows the formation of a quite weak crossflow separation only at the stern of the totally submerged SUBOFF for this rotational yaw velocity.
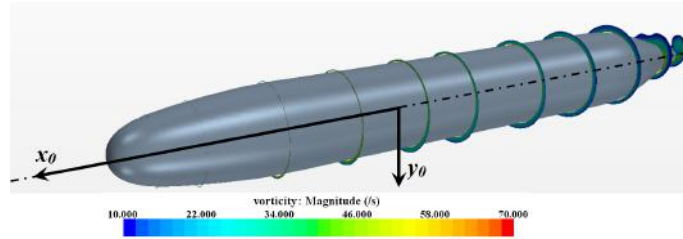
Figure 4.17: Formation of a quite weak crossflow separation over the stern of the totally submerged SUBOFF undergoing a steady turning motion with an angular velocity $r' = -0.4$ about the z_0 axis

Based on Figure 4.1 (f), in the totally submerged case, an increase in the yaw angular velocity results in an increase in the Y-force component, which is attributed to a growing pressure differential between the windward and leeward sides. Additionally, the increase in the Y-force with a decrease in submergence depth can be associated with the advent of the wave-making resistance component [21].

To investigate more closely the behavior of the Y-force generated by the yaw angular velocity r for various submergence depths, the distribution of this force component along the length of the SUBOFF is used. In this regard, Figure 4.18 shows the distribution of the Y-force arising from the yaw rate $r' = -0.4$ about z_0 axis over various submergence depths.

Figure 4.18: Distribution of the Y-force generated by the angular yaw velocity r along the SUBOFF length at $r' = -0.4$ over various submergence depths

Over the whole range of submergence depths, the largest magnitude of the Y-force is produced by the bow region where the stagnation pressure is located. Note that, based on the lateral velocity distrib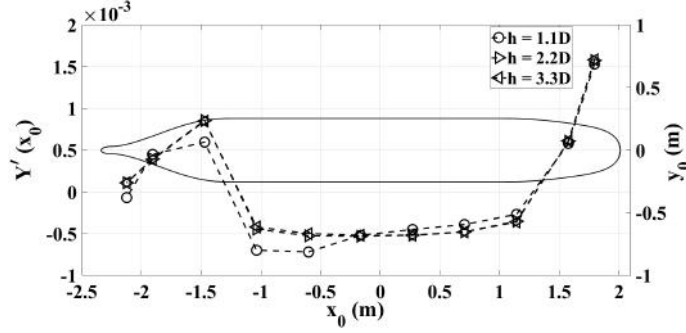ution along the SUBOFF length shown in Figure 2.13, it is expected that a positive Y-force is induced on the fore half part of the UV while a negative Y-force is produced by the aft half part. However, only a small region close to the bow in the fore half part generates a positive Y-force and surprisingly over a considerable region in the fore half part a negative Y-force is induced. Similarly, the stern region, in spite of a positive lateral velocity over the aft half part, also produces a positive Y-force. Thus, both the bow and stern regions generate a positive Y-force, which is in the opposite direction of the total Y-force exerted on the UV. Accordingly, the main contribution to the Y-force is from the region between the fore and aft shoulders. In this region, a negative Y-force is induced on the UV hull, which is in the same direction of the total Y-force acting on the UV hull.

To establish a relationship between the dynamic pressure distribution and the distribution of the Y-force along the UV, Figure 4.19 shows the dynamic pressure distribution around the SUBOFF at $x_0 s y_0$ plane and $r' = -0.4$ over various submergence depths. From Figure 4.19 several common important fluid flow characteristics over the whole range of submergence depths can be highlighted.

First is the shift of the bow stagnation point toward the windward side due to the negative lateral velocity. This shift gives rise to a decrease in the dynamic pressure at the leeward bow region. Second, which is the most crucial feature and is responsible for the total negative lateral force exerted on the SUBOFF, is the drop in the dynamic pressure in the region between the windward fore shoulder and leeward aft shoulder. Although the windward fore shoulder is expected to experience an increase in the pressure, this value decreases, which is due mainly to the dominant role of the axial velocity compared to the small negative lateral velocity at this region (see Figure 2.13). Furthermore, the drop in the dynamic pressure at the region between the midlength and the leeward aft shoulder is due to the crossflow

direction in this region, which is in the opposite direction of y_0. Third is the drop in the dynamic pressure at the windward aft shoulder, which is attributed to an increase in the fluid flow velocity at this region. Finally, fourth is the leeward shift of the aft stagnation region, which is due to the drop in the dynamic pressure at the windward aft shoulder.

Note that the third and fourth features mentioned above are largely responsible for the positive Y-force exerted at the stern region of the SUBOFF UV over the whole range of submergence depths.

(a) $h = 1.1D$

(b) $h = 2.2D$

(c) $h = 3.3D$
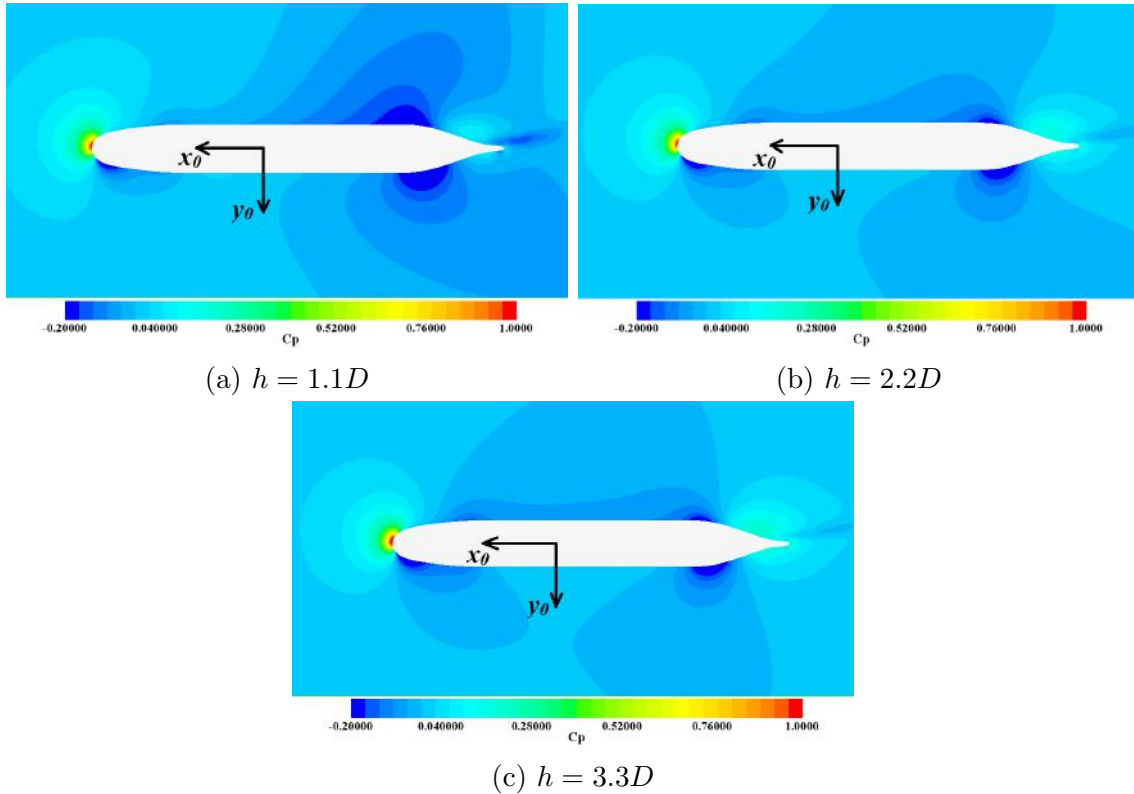
Figure 4.19: Dynamic pressure distribution around the SUBOFF at x_0sy_0 plane and $r' = -0.4$ over various submergence depths

Additionally, as can be inferred from Figure 4.18, the increase in the total Y-force exerted on the SUBOFF with a decrease in submergence depth is due to both an increase in the negative Y-force exerted over the region between the UV midlength and the aft shoulder and a decrease in the positive Y-force experienced by the aft shoulder region. To explain further, consider Figure 4.20, which shows the SUBOFF-generated wave system during a steady turning motion for a yaw angular velocity $r' = -0.4$ over submergence depth $h = 1.1D$. Based on this figure, the reason for the concurrent increase in the negative Y-force exerted over the region between the UV midlength and the aft shoulder and decrease in the positive Y-force experienced by the aft shoulder region is the depression of the free surface above the aft leeward low-pressure region created by the crossflow at this region. Accordingly,

the depression of the free surface above the aft leeward low-pressure region created by the crossflow is responsible for a more decrease in the dynamic pressure acting on the aft leeward side. The decrease in the dynamic pressure at the aft of the SUBOFF, especially at the aft leeward side, as the UV approaches the free surface can be clearly seen in Figure 4.19.
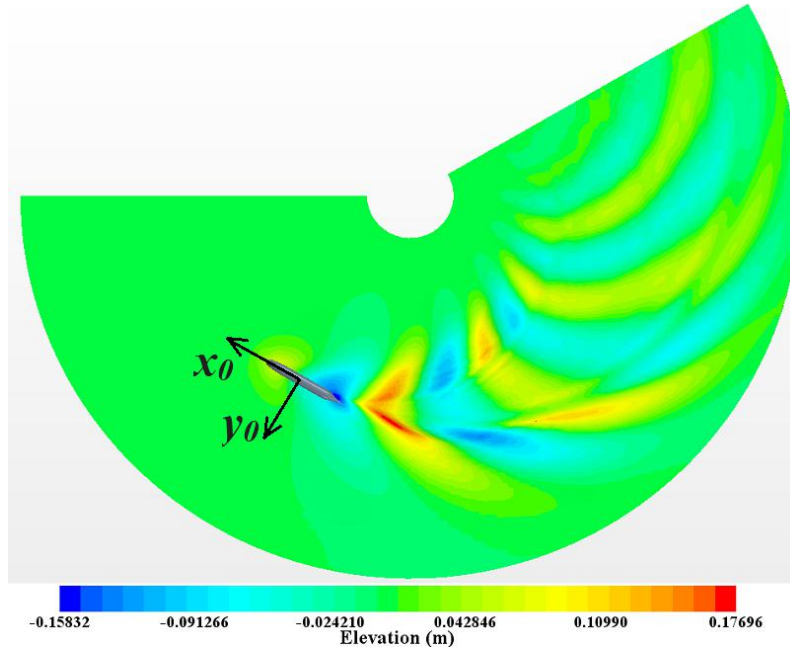
Figure 4.20: SUBOFF-generated wave system during a steady turning motion at a yaw angular velocity $r' = -0.4$ over submergence depth $h = 1.1D$

To shed more light on the explanation given for the decrease in the dynamic pressure at the aft leeward side, consider Figure 4.21, which shows the dynamic pressure distribution at two axial locations $x_0 = -1.0362\ m$ (, which is in the region between the UV midlength and the aft shoulder,) and $x_0 = -1.4718\ m$ (,which is in the aft shoulder region,) for various submergence depths. This figure clearly shows that with a decrease in submergence depth the free surface is depressed above the aft leeward low-pressure region created by the crossflow. Accordingly, the depression of the free surface above the aft leeward low-pressure region results in a more decrease in the dynamic pressure at this region, which is largely responsible for both the increase in the negative Y-force exerted over the region between the UV midlength and the aft shoulder and the decrease in the positive Y-force experienced by the aft shoulder region.

(a) $h = 1.1D$

(b) $h = 2.2D$

(c) $h = 3.3D$
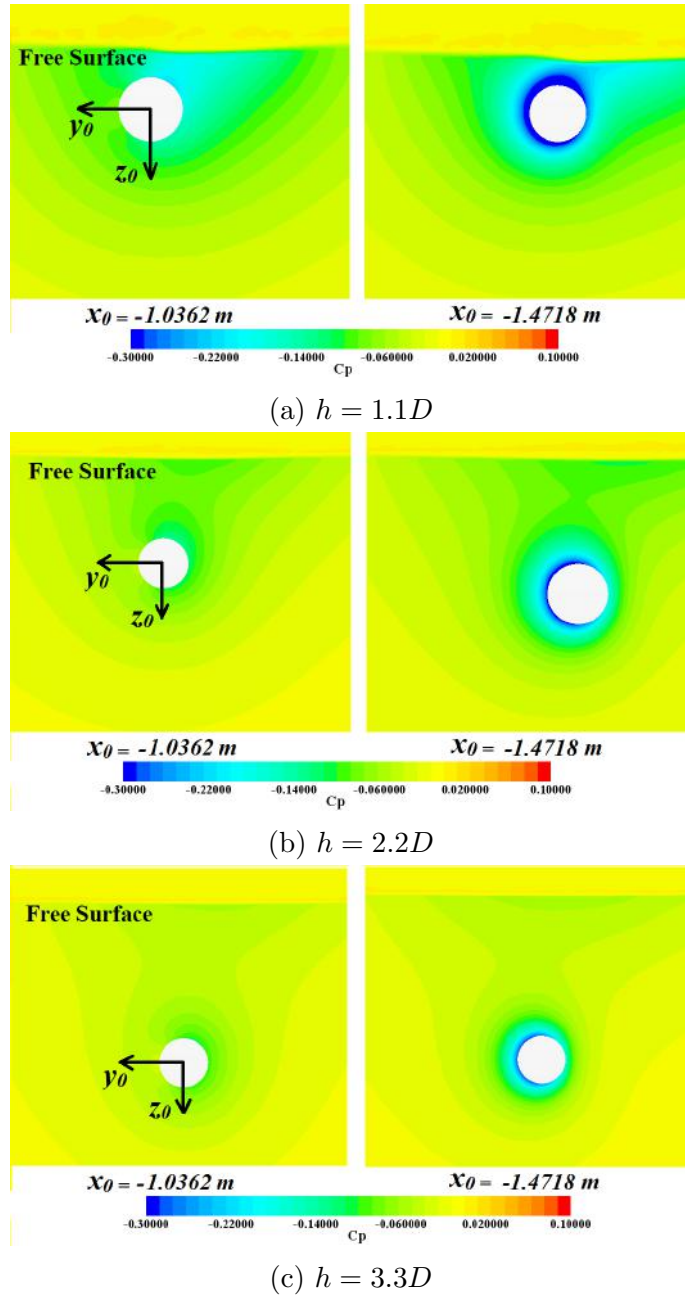
Figure 4.21: Dynamic pressure distribution around the SUBOFF at two axial locations $x_0 = -1.0362\ m$ and $x_0 = -1.4718\ m$ for various submergence depths

Moreover, Figure 4.22 presents the distribution of the N-moment arising from the yaw angular velocity r along the length of the SUBOFF at $r' = -0.4$ for various submergence depths. Based on this figure, the increase in the total N-moment, which is positive, with a decrease in submergence depth can be associated with two reasons. First is the increase in the negative Y-force exerted over the region between the UV midlength and the aft shoulder, which produces a positive N-moment. Second is the decrease in the positive Y-force experienced by the aft shoulder region, which produces a negative N-moment.
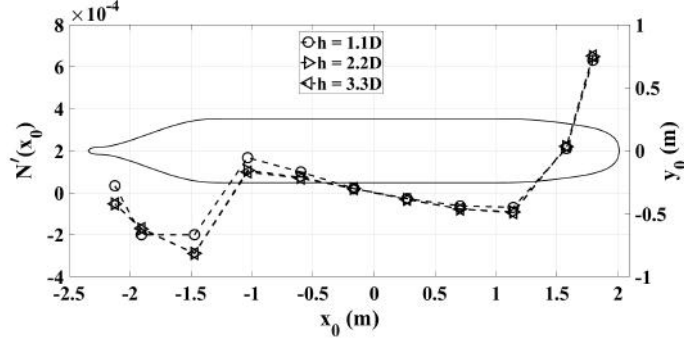
Figure 4.22: Distribution of the N-moment generated by the angular yaw velocity r along the SUBOFF length for $r' = -0.4$ over various submergence depths

Noteworthy in the results presented in this section is again the surprising effect of the stern region on the Y-force and N-moment produced by the yaw angular velocity on the SUBOFF for various submergence depths. In this regard, it is observed that the stern region generates an unexpected Y-force in the opposite direction of the total Y-force, which gives rise to a decrease in the total N-moment acting on the SUBOFF.

The obtained results further demonstrate that the Y-force and N-moment generated by the bow and stern regions are remotely affected by a decrease in submergence depth. In this regard, as the UV approaches the free surface, the region between the UV midlength and the aft shoulder is largely responsible for an increase in both the Y-force and the N-moment. This is attributed mainly to the depression of the free surface above the aft leeward low-pressure region created by the crossflow. Accordingly, the depression of the free surface above the aft leeward low-pressure region created by the crossflow results in a more decrease in the dynamic pressure in this region. This is largely responsible for both an increase in the Y-force exerted over the region between the UV midlength and the aft shoulder, which acts in the same direction of the total Y-force, and a decrease in the Y-force experienced by the aft shoulder region, which acts in the opposite direction of the total Y-force. Additionally, note that the Y-force exerted over the region between the UV midlength and the aft shoulder generates an N-moment in the same direction of the total N-moment while the Y-force acting on the aft shoulder region induces an N-moment in the opposite direction of the total N-moment. This, accordingly, largely explains the reason for the concurrent increase in both the Y-force and N-moment with a decrease in submergence depth.

4.3 Hydrodynamic coefficients in the horizontal plane for various submergence depths

This section presents the hydrodynamic coefficients used to express the external forces and moments in the maneuvering equations without and with the presence of the free surface (Equations 2.5-2.7).

Accordingly, the hydrodynamic coefficients due to velocity components are obtained by fitting the polynomial functions given in Equations 2.11-2.13 and 2.22-2.27 to the hydrodynamic forces and moments represented in Figure 4.1 via the linear least-squares method. Figure 4.1 presents the fitted polynomial functions to the hydrodynamic forces and moments resulting from the UV velocity components. Additionally, the hydrodynamic acceleration coefficients are estimated by using Equations 2.29-2.33. Furthermore, to calculate the hydrodynamic coefficients related to the rudder, Equations 2.42-2.44 are used.

Table 4.1 presents the predicted hydrodynamic coefficients for various submergence depths. Additionally, Figure 4.23 shows the behavior of the sway and yaw hydrodynamic coefficients with respect to submergence depth. In this figure, $h = 5.5D$ corresponds to $h = \infty$, since for $\frac{h}{D} > 5$ the free surface effect completely vanishes [10]. As can be inferred from Table 4.1 and Figure 4.23, a decrease in submergence depth generally causes a nonlinear increase in the hydrodynamic coefficients, except for N'_v, $Y'_{r|r|}$ and $N'_{r|r|}$ which reduce as the UV approaches the free surface. It is further observed in Figure 4.23 that with an increase in submergence depth the hydrodynamic coefficients appear to approach asymptotically their equivalent totally submerged values.

Table 4.1: The hydrodynamic coefficients (h.c.) for various submergence depths

| h.c.	$h = 1.1D$	$h = 2.2D$	$h = 3.3D$	$h = \infty$
$X'_{\dot{u}}$	-0.00037	-0.00037	-0.00037	-0.00037
$X'_{u\|u\|}$	-	-	-	-0.00094
X'_{vv}	0.00436	-0.00129	-0.00239	-0.00265
X'_{rr}	0.00028	-0.00008	-0.00006	-0.00005
$X'_{\delta r \delta r}$	-0.00207	-0.00207	-0.00207	0.00207
$Y'_{\dot{v}}$	-0.01353	-0.01353	-0.01353	-0.01353
$Y'_{\dot{r}}$	0	0	0	0
Y'_{v}	-0.01380	-0.00209	-0.00107	-0.00105
$Y'_{v\|v\|}$	-0.07056	-0.06759	-0.06591	-0.06318
Y'_{r}	0.00206	0.00079	0.00067	0.00064
$Y'_{r\|r\|}$	0.00073	0.00094	0.00102	0.00101
$Y'_{\delta r}$	0.00658	0.00658	0.00658	0.00658
$N'_{\dot{v}}$	0	0	0	0
$N'_{\dot{r}}$	-0.00062	-0.00062	-0.00062	-0.00062
N'_{v}	-0.01281	-0.01334	-0.01324	-0.01332
$N'_{v\|v\|}$	0.01441	0.01198	0.01156	0.01176
N'_{r}	-0.00130	-0.00093	-0.00086	-0.00084
$N'_{r\|r\|}$	-0.00033	-0.00038	-0.00043	-0.00042
$N'_{\delta r}$	-0.00260	-0.00260	-0.00260	-0.00260
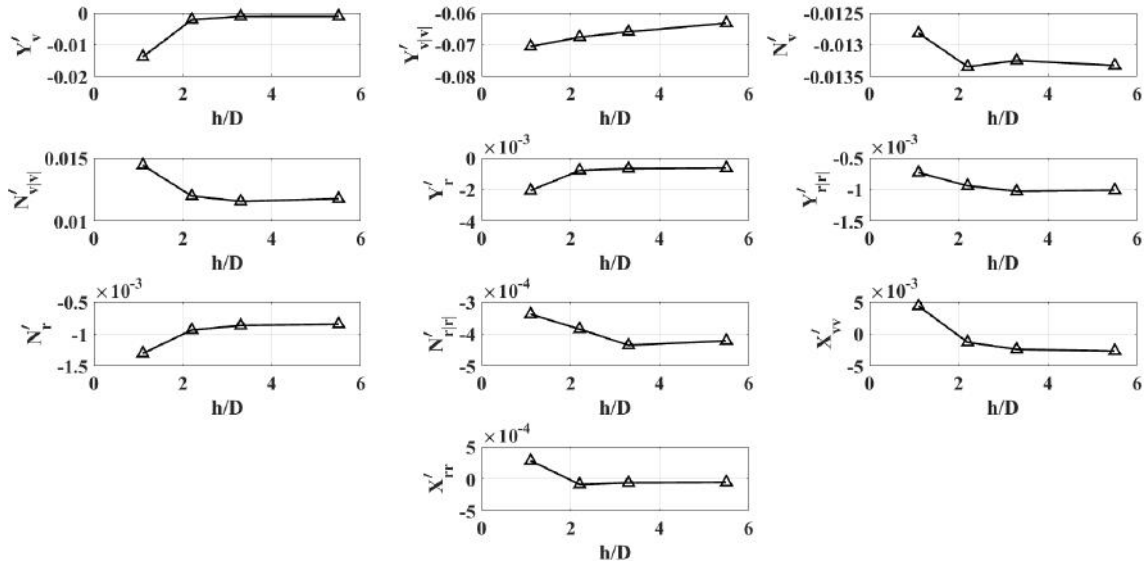
Figure 4.23: Sway and yaw hydrodynamic coefficients over various submergence depths

4.4 Dynamic stability analysis of the SUBOFF UV for various submergence depths

In the present section, the dynamic stability of the SUBOFF UV is examined over various submergence depths by using Equation 2.52. Furthermore, to analyze the contribution of the size of the rudder to the dynamic stability, the rudder span b_v is changed from zero to $2.378b_{v0}$, where b_{v0} is the initial rudder span.

In this regard, Figure 4.24 shows the stability criterion (SC) over various submergence depths and rudder spans. It can be inferred from this figure that without the presence of the rudder ($\frac{b_v}{b_{v0}} = 0$) the SUBOFF UV is inherently unstable for the entire range of submergence depths. However, at this condition, with a decrease in submergence depth the stability increases remarkably. This is due mainly to a decrease in the N-moment produced by the lateral velocity v and an increase in the Y-force generated by the same velocity component, which results in a decrease in the lever of the hydrodynamic moment generated by the lateral velocity l_v. In this regard, Figure 4.25 shows the values of l_v and l_r as defined in Equation 2.49 over various submergence depths. In this figure, $h = 5.5D$ corresponds to $h = \infty$, since for $\frac{h}{D} > 5$ the free surface effect completely vanishes [10]. As can be inferred from Figure 4.25, while l_r slightly increases with a decrease in submergence depth, l_v undergoes a significant decrease as submergence depth is decreased. This largely explains the increase in the dynamic stability as the UV approaches the free surface. Further details about the dynamic stability of the bare hull axisymmetric SUBOFF UV are presented in the next section.

Additionally, by adding the rudder ($\frac{b_v}{b_{v0}} = 1$) the dynamic stability of the SUBOFF UV is predicted to increase for all the submergence depths. However, despite the inclusion of the rudder, the SUBOFF UV is still predicted to have a negative SC. Based on Figure 4.24, fortunately it is observed that an increase in the rudder span gives rise to an almost linear increase in SC values at the entire range of submergence depths. Noteworthy in Figure 4.24 is the marginal difference between the values of SC at various submerence depths for $\frac{b_v}{b_{v0}} > 1$, which indicates the dominance of the rudder in the dynamic stability of the UV.

The stability is achieved for $\frac{b_v}{b_{v0}} > 1.5$ over the entire range of submergence depths. Based on HUMPHREYS e WATKINSON [74], a value of SC close to 1.0 means that the UV is overly stable and, thus, has a poor maneuverability. As recommended by HUMPHREYS e WATKINSON [74], a value of SC larger than 0.2 and smaller than 0.7 provides the UV with a reasonable level of stability. In this regard, it is observed that a value of $1.79b_{v0}$ for the rudder span provides an SC approximately equal to 0.56, 0.31, 0.29 and 0.28 for $h = 1.1D$, $h = 2.2D$, $h = 3.3D$ and $h = \infty$, respectively. Although the SC values over various submergence depths

appear to be within the range recommended by HUMPHREYS e WATKINSON [74], at large depths the UV possesses a very low level of stability, which during the open-loop maneuvering simulations leads to kinematic variables well outside the ranges of the variables used to obtain the hydrodynamic forces and moments. Therefore, herein, to simulate the maneuvering of the SUBOFF in the horizontal plane, a value of $2.18 b_{v0}$ was chosen for the rudder span, which is predicted to provide an SC approximately equal to 0.78, 0.51, 0.48 and 0.47 for $h = 1.1D$, $h = 2.2D$, $h = 3.3D$ and $h = \infty$, respectively.
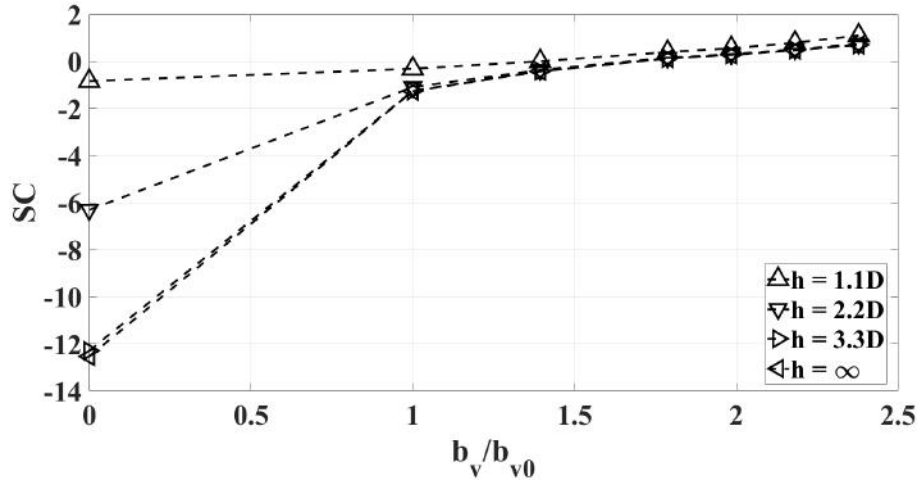
Figure 4.24: Stability criterion (SC) for various submergence depths and rudder spans b_v
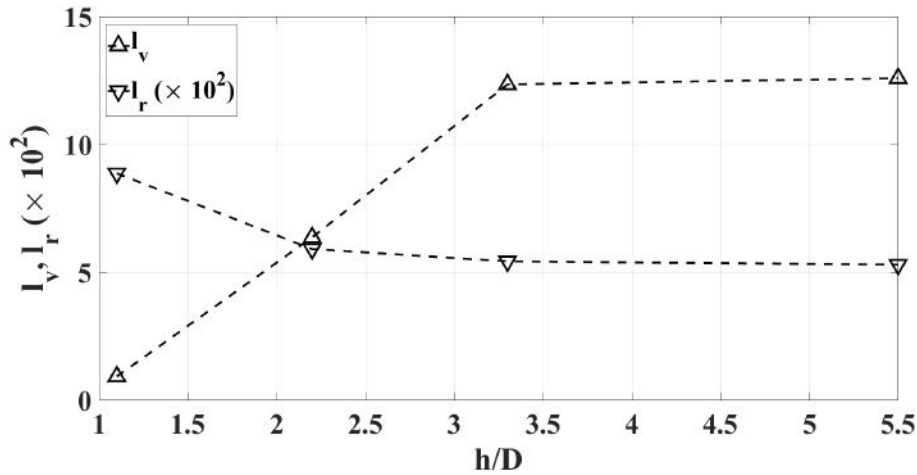

Figure 4.25: l_v and l_r for various submergence depths

4.4.1 A detailed analysis of the dynamic stability of the bare hull SUBOFF UV for various submergence depths

In the previous section, it is observed that for $h = \infty$ the bare hull SUBOFF axisymmetric UV is highly unstable. This high level of instability may be due to

both a small magnitude of the lever of the hydrodynamic moment generated by the yaw rate l_r and a large magnitude of the lever of the hydrodynamic moment produced by the lateral velocity l_v. Herein, it is demonstrated that the stern region of the SUBOFF gives rise to both an increase in the l_v and a decrease in the l_r.

First, the influence of the stern region on the l_v is investigated. The large magnitude of the l_v emanates from either a large value of the N-moment or a small value of the Y-force or even both of which. In this regard, consider Figures 4.13 and 4.16, which show the distributions of the Y-force and N-moment generated by the v velocity along the length of the SUBOFF for various submergence depths. As can be seen in Figure 4.13, the stern region over the whole range of submergence depths generates consistently a large Y-force in the opposite direction of the total Y-force, which results in a reduction in the total Y-force acting on the UV. Furthermore, based on Figure 4.16, it is seen that, over the whole range of submergence depths, the largest magnitude of the N-moment along the SUBOFF length is consistently produced by the stern region. Thus, it is observed that for $h = \infty$ the stern region is predominantly responsible for the comparatively large value of the l_v through increasing the N-moment and reducing the Y-force.

Additionally, as can be inferred from Figures 4.13 and 4.16, approaching the free surface has negligible effect on the Y-force and N-moment generated by the stern and bow regions. In this regard, the reason for the reduction of the l_v with a decrease in submergence depth (see Figure 4.25), is mainly attributed to the region located between the UV midlength and the aft shoulder. In this region, as mentioned in section 4.2.2, the rising of the free surface above the windward stagnation point together with the depression of the free surface above the leeward low-pressure region created by the crossflow gives rise to a more increase and decrease in the local dynamic pressure values at the windward and leeward sides, respectively. This, consequently, gives rise to an increase in the Y-force, while a decrease in the N-moment as the UV approaches the free surface, which is largely responsible for the decrease in the l_v.

Secondly, the influence of the stern region on the l_r is evaluated. The small magnitude of the l_r over the whole range of submergence depths may be due to either a small value of the N-moment or a large value of the Y-force or even both of which. To shed more light on this, consider Figures 4.18 and 4.22, which show the distributions of the Y-force and N-moment generated by the r velocity along the length of the SUBOFF for various submergence depths. It is seen in Figure 4.18 that for the entire range of submergence depths the stern generates a Y-force in the opposite direction of the total Y-force, which results in an increase in the l_r. On the other hand, as can be inferred from Figure 4.22, the N-moment generated by the stern region at all the submergence depths acts in the opposite direction of

the total N-moment, which consequently reduces this moment component. Thus, it is seen that, for the whole range of submergence depths, although the stern region causes an increase in the Y-force, it gives rise to a reduction in the N-moment. Accordingly, the stern region is partially responsible for the relatively small value of the l_r through decreasing the N-moment.

In this case again, based on Figures 4.18 and 4.22, approaching the free surface has negligible effect on the Y-force and N-moment generated by the yaw rate on the stern and bow regions. Accordingly, as can be inferred from Figures 4.18 and 4.22, the increase in both the total Y-force and N-moment exerted on the SUBOFF with a decrease in submergence depth is due mainly to both an increase in the Y-force exerted over the region between the UV midlength and the aft shoulder, which acts in the same direction of the total Y-force, and a decrease in the Y-force experienced by the aft shoulder region, which acts in the opposite direction of the total Y-force. As explained in section 4.2.2, this is attributed to the depression of the free surface above the aft leeward low-pressure region created by the crossflow. Accordingly, the depression of the free surface above the aft leeward low-pressure region results in a more decrease in the dynamic pressure in this region, which is largely responsible for both an increase in the Y-force exerted over the region between the UV midlength and the aft shoulder and a decrease in the Y-force experienced by the aft shoulder region.

However, based on Figures 4.18 and 4.22, as a decrease in submergence depth causes a concurrent increase in both the N-moment and Y-force generated by the yaw rate, the l_r undergoes merely a small increase as the UV approaches the free surface.

Thus, the discussion given above demonstrates that the stern region plays a decisive role in the dynamic stability of an axisymmetric UV in the horizontal plane. Additionally, it is observed that the behavior of the Y-force and N-moment generated by the lateral and yaw velocities on the region located between the midlength and the aft shoulder of the SUBOFF is largely responsible for the concurrent increase in the l_r and decrease in the l_v as the UV approaches the free surface, which gives rise to an increase in the UV dynamic stability.

4.5 Maneuverability analysis of the SUBOFF UV for various submergence depths

In the present section, to evaluate the free surface effect on the maneuverability of the SUBOFF UV in the horizontal plane, the turning and zigzag standard maneuvers are performed for various submergence depths, as explained in section 2.1.6.

This evaluation is carried out by integrating numerically the Equations 2.5-2.7 for maneuvering simulations for the totally submerged and shallowly submerged UVs, as explained in section 2.1.5. The numerical integration is performed using the second-order improved Euler method with a time-step size equal to 0.01 s. The numerical computations demonstrate that this time-step size is small enough to give sufficiently precise responses for the maneuvering analysis. The simulations rely on the hydrodynamic coefficients presented in Table 4.1 for various submergence depths. Additionally, as mentioned in section 2.1.2, in the maneuvering simulations with the presence of the free surface, a cubic interpolation is used to express the axial hydrodynamic force $X_{f(u,h)}$ in the equations of motion, as this force component is stored in a one-dimensional tabular form at various submergence depths. Furthermore, to model the thrust force, Equations 2.45 and 2.48 are used. However, as no data of free-running maneuvering tests are available, merely qualitative conclusions are drawn.

4.5.1 Turning Maneuver

The turning maneuvers are performed with a rudder deflection of $\delta_{r0} = -10°$ at an approach velocity of $U_0 = 3.344 \frac{m}{s}$, which is the underlying reference velocity used to calculate the hydrodynamic forces and moments arising from the UV velocity components. In this regard, the rudder was executed with a deflection rate equal to $10° \frac{1}{s}$ after the UV attains the steady approach velocity.

Figure 4.26 shows the trajectories of the SUBOFF UV over various submergence depths. This figure reveals that advance, transfer, tactical diameter and turning diameter all undergo an increase with a decrease in submergence depth. The increase in these quantities with a decrease in submergence depth can be further observed in Figure 4.27, which shows the advance, transfer, tactical diameter and turning diameter of the SUBOFF in the turning maneuver for various submergence depths. The increase in these quantities is attributed to an increase in the UV damping characteristics, which is reflected in the behavior of the hydrodynamic forces and moments generated by the UV velocity components as shown in Figure 4.1. Accordingly, the increased damping characteristics of the UV with a decrease in submergence depth in return decreases the maneuverability of the UV.

Figure 4.27 also represents the steady drift angle of the SUBOFF at various submergence depths. As can be seen, the drift angle reduces with a decrease in submergence depth. To explain the reason for the decrease in drift angle consider Figure 4.28, which shows schematically the SUBOFF UV in the steady phase of a turning maneuver at the rudder deflection of $-\delta_{r0}$. As can be seen in this figure, during a turning maneuver the N-moment generated by the lateral velocity v tends

to increase the drift angle, while the N-moment produced by the yaw rate r tends to decrease this angle. Accordingly, based on Figure 4.1, as with a decrease in submergence depth the N-moment generated by the v undergoes a reduction while the N-moment induced by the r goes up, the drift angle decreases.

Additionally, Figure 4.29 presents the time histories of the rudder deflection angle, drift angle, yaw rate and the UV speed. The increase in the N-moment generated by the yaw rate r with a decrease in submergence depth is apparent in the evolution of the yaw rate, which reduces with a decrease in submergence depth, as shown in Figure 4.29 (c). Moreover, as mentioned earlier, both the decrease in the N-moment produced by the lateral velocity v and the increase in the N-moment generated by the yaw rate r are responsible for the decrease in drift angle (Figure 4.29 (b)). Furthermore, the evolution of the UV speed U with respect to the steady approach speed U_0, as shown in Figure 4.29 (d), demonstrates that as the UV approaches the free surface the speed loss reduces, which is associated with a decrease in the drift angle (see Figure 4.29 (b)).
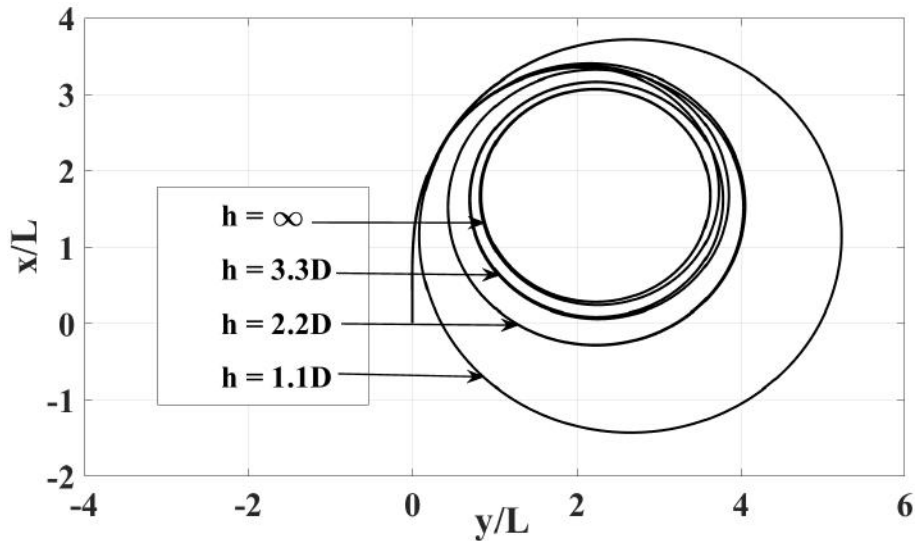

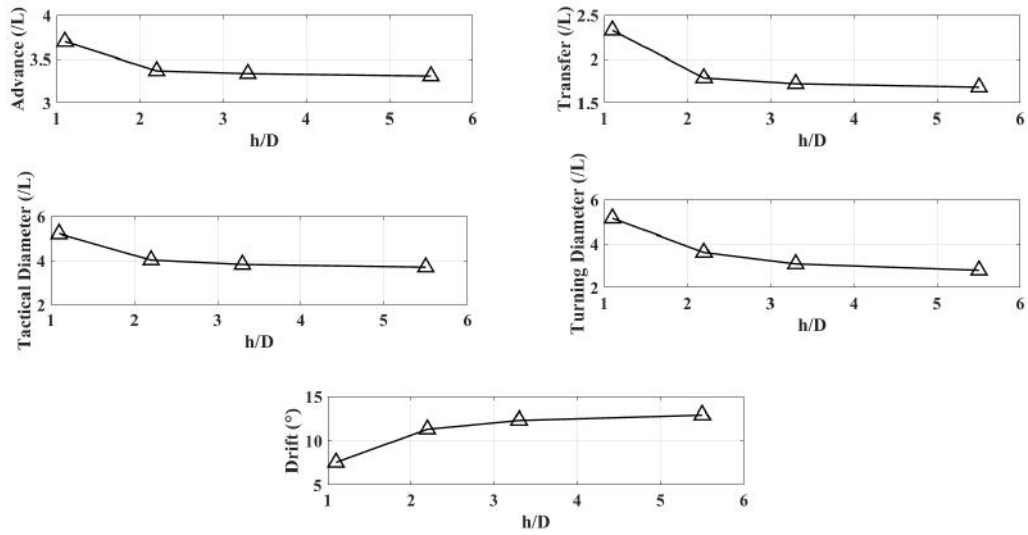Figure 4.26: Trajectory of the SUBOFF UV in the turning maneuver over various submergence depths

Figure 4.27: Advance, transfer, tactical diameter, turning diameter and drift angle of the SUBOFF in the turning maneuver over various submergence depths
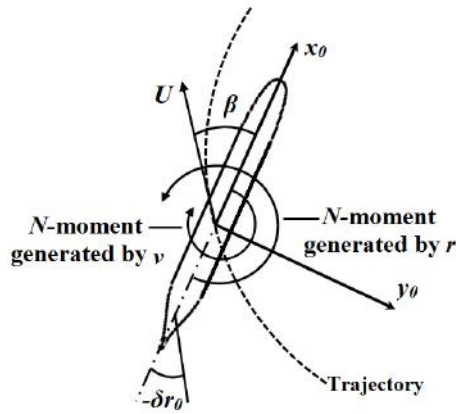

Figure 4.28: The SUBOFF UV undergoing a turning maneuver at a rudder deflection of $-\delta_{r0}$
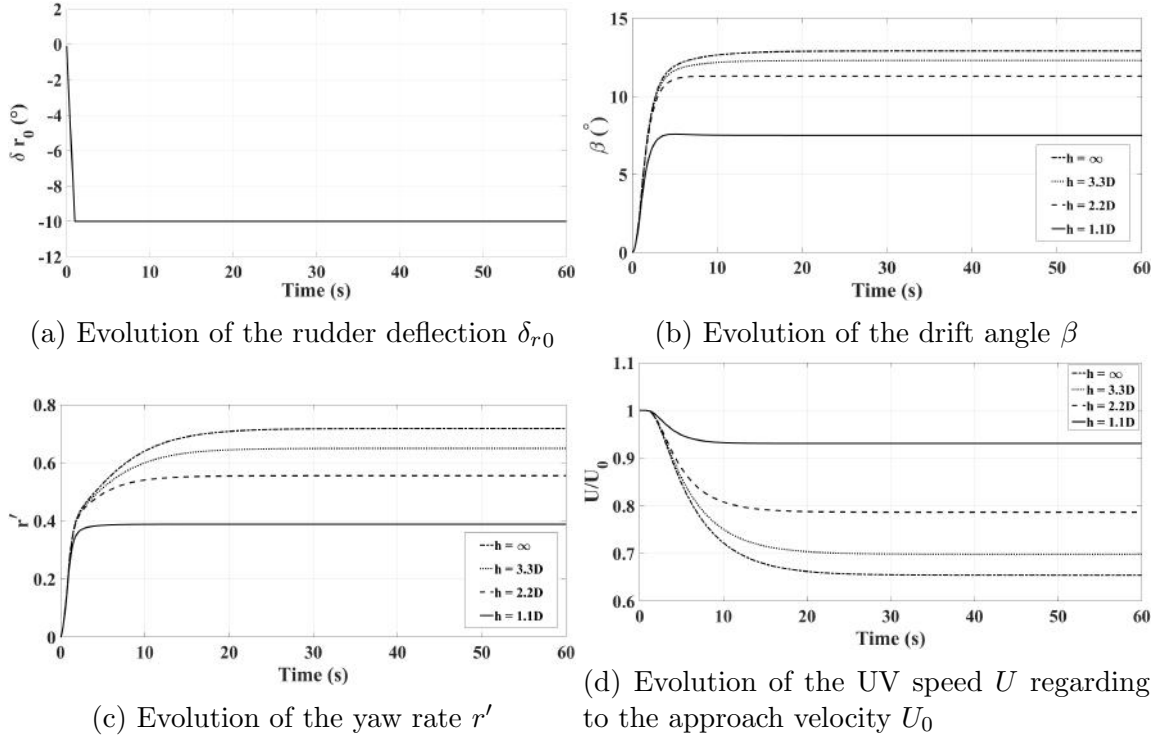
(a) Evolution of the rudder deflection δ_{r0}

(b) Evolution of the drift angle β

(c) Evolution of the yaw rate r'

(d) Evolution of the UV speed U regarding to the approach velocity U_0

Figure 4.29: Time histories of the variables in turning maneuver over various submergence depths

4.5.2 Zigzag Maneuver

In this section, a 10/10 zigzag maneuver is performed at an approach velocity of $U_0 = 3.344 \ \frac{m}{s}$, which is the underlying reference velocity used to calculate the hydrodynamic forces and moments arising from the UV velocity components. In this regard, the rudder was executed with a deflection rate equal to $10° \ \frac{1}{s}$ after the UV attains the steady approach velocity.

Figure 4.30 shows the evolution of the rudder deflection angle δ_{r0} and the yaw angle ψ of the SUBOFF UV during the zigzag maneuver over various submergence depths. This figure clearly emphasizes the overriding role of the increased damping characteristics of the UV with a decrease in submergence depth. As can be seen in this figure, the overshoot angles diminish with a decrease in submergence depth, which is due to the improved course stability as the UV approaches the free surface.

The decrease in the first and second overshoot angles, along with the times to execute the rudder for the third and fourth times can be inferred from Figure 4.31, which shows these quantities during the zigzag maneuver over various submergence depths. The decrease in these quantities is attributed to an increase in the damping characteristics of the UV, which is reflected in the plots of the hydrodynamic forces and moments in terms of the UV velocity components shown in Figure 4.1. This, in return, increases the course stability of the SUBOFF with a decrease in submergence

depth.

Additionally, Figure 4.32 presents the time histories of the drift angle, yaw rate and UV speed. As mentioned earlier, both the decrease in the N-moment produced by the lateral velocity v and the increase in the N-moment induced by the yaw rate r with a decrease in submergence depth are responsible for the reduction in drift angle shown in Figure 4.32 (a). In this case again, the increase in the N-moment generated by the yaw rate r with a decrease in submergence depth is apparent in the evolution of the yaw rate, which undergoes a reduction, as shown in Figure 4.32 (b). Furthermore, the evolution of the UV speed U with respect to the steady approach speed U_0, as shown in Figure 4.32 (c), demonstrates a reduction in speed loss as the UV approaches the free surface, which is attributed to a decrease in the drift angle.

Moreover, Figure 4.33 shows the SUBOFF trajectory during the 10/10 zigzag maneuver for various submergence depths. As can be expected, the increase in the damping characteristics of the UV and consequently in the course stability of the UV with a decrease in submergence depth gives rise to a decrease in the distance traveled by the UV.
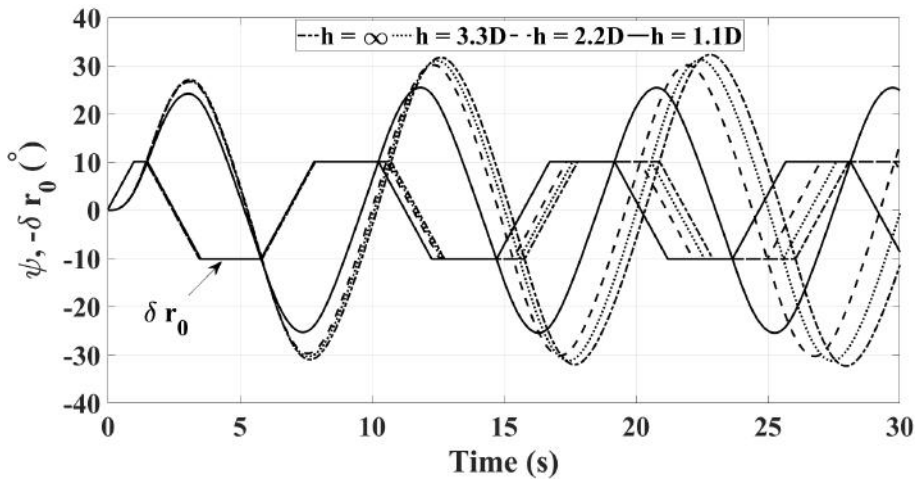
Figure 4.30: Evolution of the rudder deflection angle δ_{r0} together with the yaw angle ψ of the SUBOFF UV during the zigzag maneuver over various submergence depths
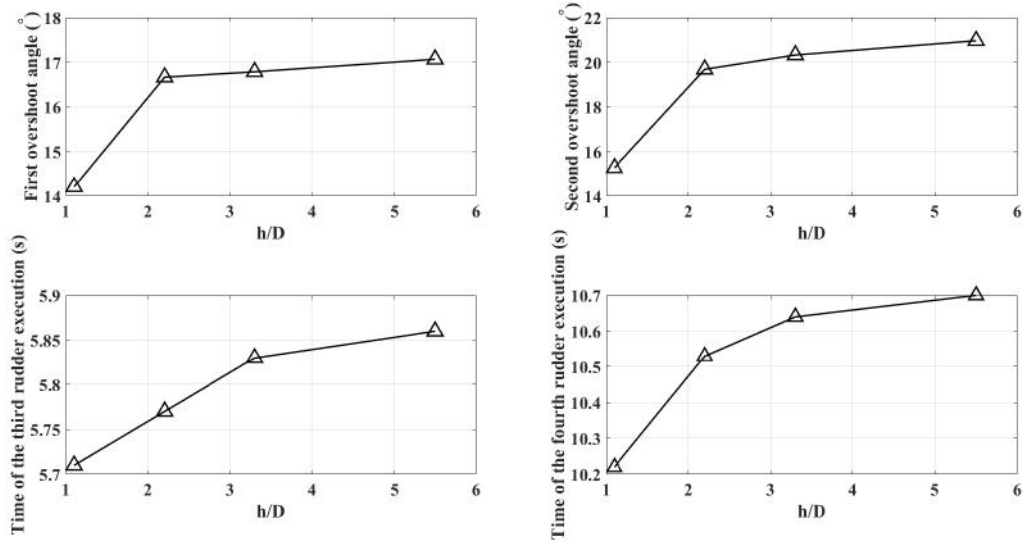
Figure 4.31: First overshoot angle, second overshoot angle, the time to execute the rudder for the third time and for the fourth time during the zigzag maneuver over various submergence depths

(a) Evolution of the drift angle β

(b) Evolution of the yaw rate r'

(c) Evolution of the UV speed U regarding to the approach velocity U_0

Figure 4.32: Time histories of the variables in zigzag maneuver over various submergence depths
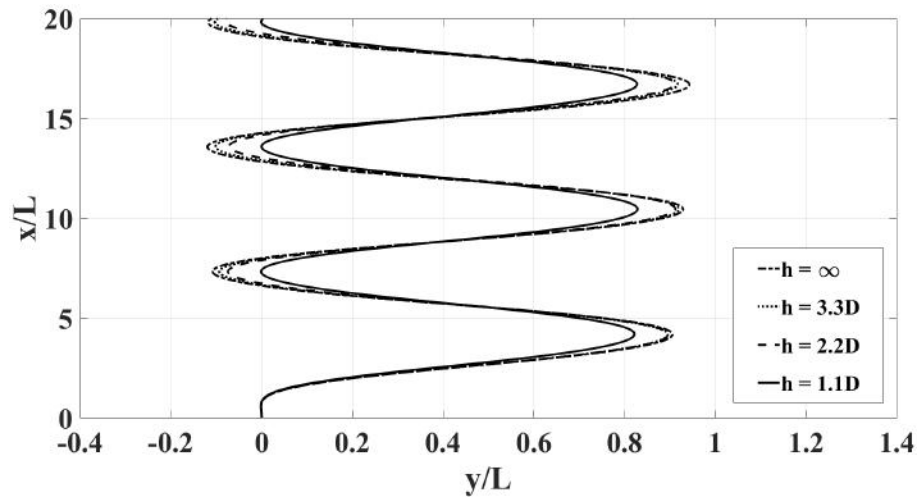
Figure 4.33: Trajectory of the SUBOFF UV in the zigzag maneuver over various submergence depths

Chapter 5

Conclusions

The present thesis seeks to evaluate the free surface effect on the hydrodynamics and dynamics of the shallowly submerged SUBOFF axisymmetric UV traveling close to the free surface in the horizontal plane. In this regard, the hydrodynamic captive tests, including the straight-ahead resistance tests, drift tests and rotating arm tests, are performed on the bare hull SUBOFF UV model by using numerical simulations based on URANS equations coupled with a Reynolds stress turbulence model. These captive tests are carried out for various submergence depths and proper ranges of UV axial, lateral and yaw velocity components. The numerical simulations are conducted in the commercial code STARCCM+, which solves the integral forms of the URANS and continuity equations over unstructured grids by using the finite volume method.
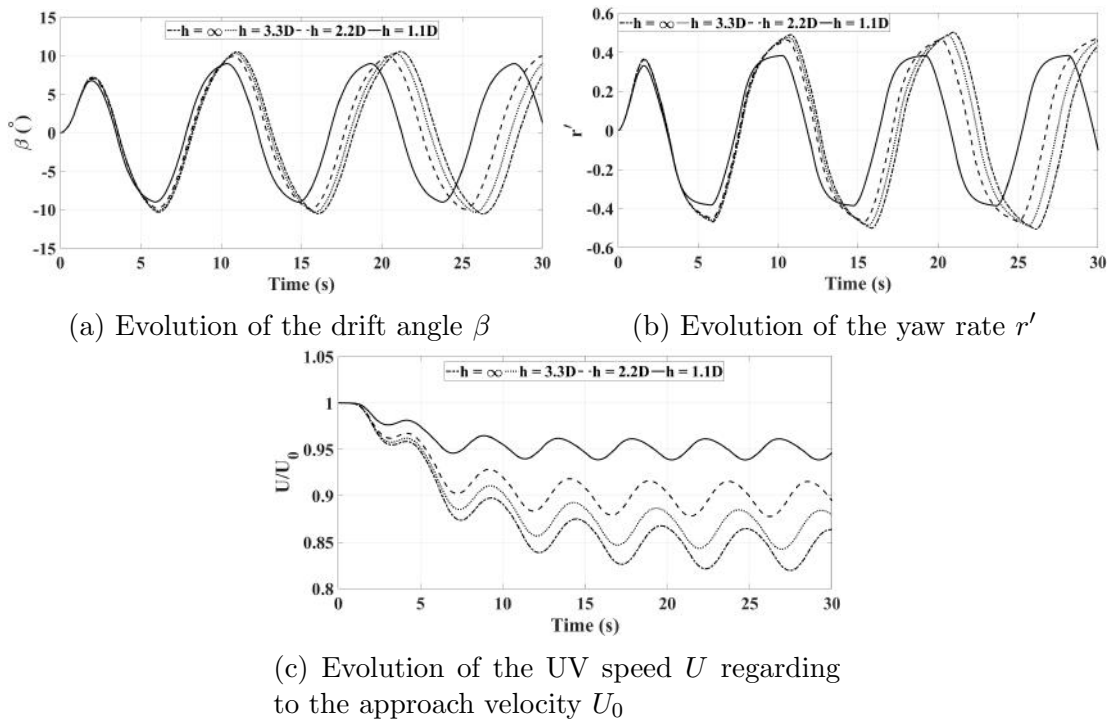
Herein, to verify the solutions obtained from the numerical simulations, a systematic grid convergence study is performed over three grids. This study is carried out on the forces and moments acting on the SUBOFF hull obtained from each hydrodynamic test at two computational conditions: without and with the presence of the free surface. Generally, relatively small values for grid uncertainties are obtained from this study, which demonstrate the negligible sensitivity of the solutions to the grid resolution. Furthermore, the validation of the numerical simulations for each hydrodynamic test is performed by comparing the calculated forces and moments against the available experimental measured ones. Accordingly, the comparison against the experimental data for the straight-ahead resistance simulations is performed for both totally submerged and shallowly submerged cases, while for the drift and rotating arm tests is performed merely for totally submerged cases. This comparison shows that in most cases the calculated forces and moments are within their validation uncertainties.

After the verification and validation process, the forces and moments acting on the SUBOFF UV in both the vertical and horizontal planes obtained from the captive tests are presented with respect to both submergence depth and UV velocity

components. Generally, a decrease in submergence depth gives rise to an increase in almost all the forces and moments except for the N-moment arising from the lateral velocity, which unlike the other forces and moments undergoes a reduction. Additionally, it is observed that the free surface effect on the hydrodynamic forces and moments diminishes drastically with an increase in submergence depth.

Subsequently, to investigate how the free surface affects the hydrodynamics of a UV performing steady motions in the horizontal plane, the behavior of the forces and moments acting on the UV hull are closely analyzed for various submergence depths and UV velocity components. Several important results obtained from this analysis can be summarized as follows:

- In case of the shallowly submerged UVs, the humps and hollows in the curve of the X-force arising from the axial velocity component (resistance force) are a consequence of the interference effects between the bow and aft shoulder waves, rather than between the bow and stern waves, which is usually considered in naval architecture. This is due mainly to the closer proximity of the aft shoulder to the free surface, which consequently contributes more to the UV-generated wave system, compared to the stern.

- The stern region of the SUBOFF UV has a crucial effect on the Y-force and N-moment arising from the lateral and angular yaw velocity components for various submergence depths. Accordingly, it is observed that at the entire range of submergence depths over this region an unexpected Y-force in the opposite direction of the total Y-force is induced by both the lateral and angular yaw velocities, which gives rise to an increase in the total N-moment arising from the lateral velocity while results in a decrease in the total N-moment produced by the yaw rate.

- Approaching the free surface has a negligible effect on the Y-force and N-moment generated by both the lateral and angular yaw velocity components on the stern and bow regions. In this regard, with a decrease in submergence depth, the region between the UV midlength and the aft shoulder is mainly responsible for the increase or decrease in the total Y-force and N-moment. With a decrease in submergence depth, the effect of this region on the Y-force and N-moment generated by each velocity component is as follows:

  – As the UV approaches the free surface, the increase in the Y-force and decrease in the N-moment both arising from the lateral velocity are mainly attributed to a growing pressure difference between the windward and leeward sides located in the region between the UV midlength and the aft shoulder. Accordingly, in this region, the rising of the free surface

above the windward stagnation point, together with the depression of the free surface above the leeward low-pressure region created by the crossflow, gives rise to a more increase and decrease in the local dynamic pressure values at the windward and leeward sides, respectively. This, consequently, causes an increase in the pressure difference between the windward and leeward sides, which results in an increase in the Y-force while a decrease in the N-moment as the UV approaches the free surface. Since the Y-force generated by the region between the UV midlength and the aft shoulder acts in the same direction of the total Y-force while it generates an N-moment in the opposite direction of the total N-moment.

– With a decrease in submergence depth, the concurrent increase in the Y-force and the N-moment both arising from the yaw rate is primarily attributed to the depression of the free surface above the aft leeward low-pressure region created by the crossflow. Accordingly, the depression of the free surface above the aft leeward low-pressure region results in a more decrease in the dynamic pressure in this region. This is largely responsible for both an increase in the Y-force exerted over the region between the UV midlength and the aft shoulder, which acts in the same direction of the total Y-force, and a decrease in the Y-force experienced by the aft shoulder region, which acts in the opposite direction of the total Y-force. This, accordingly, gives rise to an increase in both the total Y-force and the total N-moment; since the Y-force exerted over the region between the UV midlength and the aft shoulder generates an N-moment in the same direction of the total N-moment while the Y-force exerted over the aft shoulder region generates an N-moment in the opposite direction of the total N-moment.

• Significant interaction is observed between the free surface and the low-pressure region created by the vortical flow structure developed on the leeward side of the SUBOFF UV at moderate drift angles. As a result of this interaction, the leeward vortical flow structure affects remarkably the forces and moments exerted on the shallowly submerged SUBOFF. Several crucial effects of the leeward vortical flow structure are as follows:

– At the shallowest submergence depth, the growth of the leeward vortical flow structure with an increase in the lateral velocity causes more depression in the free surface, which consequently increases the X-force component, due to an increase in the wave-making resistance component.

– At the shallowest submergence depth, the depression of the free surface above the leeward vortical flow structure causes a more decrease in the

120

local dynamic pressure value at the leeward side, which is partially responsible for the increase in the Y-force. Additionally, as the increase in the Y-force occurs mainly in the aft region, where the leeward vortical structure is formed, the N-moment exerted on the hull undergoes a reduction with a decrease in submergence depth.

After a detailed assessment of the free surface effect on the SUBOFF hydrodynamics, the dynamic stability of the UV in the horizontal plane over various submergence depths is evaluated. It is seen that the totally submerged bare hull SUBOFF axisymmetric UV is highly unstable. This high level of instability is attributed to the stern region. In this regard, as mentioned earlier, an unexpected Y-force in the opposite direction of the total Y-force is induced by both the lateral and yaw velocities over the stern region. This, consequently, gives rise to an increase in the total N-moment arising from the lateral velocity while results in a decrease in the total N-moment produced by the yaw rate. This, accordingly, leads to an increase in the l_v while a decrease in the l_r, which consequently results in an extremely low level of dynamic stability for the SUBOFF UV.

Additionally, with a decrease in submergence depth the dynamic stability increases remarkably. In this regard, as mentioned earlier, a decrease in submergence depth has negligible effect on the Y-force and N-moment generated by both the lateral and angular yaw velocity components on the stern and bow regions. Accordingly, the increase in the dynamic stability as the UV approaches the free surface is mainly associated with the behavior of the Y-force and N-moment generated by the lateral and yaw velocities on the region located between the UV midlength and the aft shoulder of the SUBOFF. As mentioned earlier, the behavior of the Y-force and N-moment in this region gives rise to an increase in the Y-force while a decrease in the N-moment both arising from the lateral velocity. Additionally, the behavior of the Y-force and N-moment in this region causes an increase in both the Y-force and the N-moment induced by the yaw rate. Thus, the behavior of the Y-force and N-moment generated by the lateral and yaw velocities on the region located between the UV midlength and the aft shoulder is largely responsible for the concurrent increase in the l_r and decrease in the l_v as the UV approaches the free surface, which gives rise to an increase in the UV dynamic stability.

Finally, in the present research, to evaluate the free surface effect on the maneuverability of the SUBOFF UV in the horizontal plane, the turning and zigzag standard maneuvers are performed for various submergence depths. The maneuverability evaluation for various submergence depths is performed by using the standard equations of motion proposed for the maneuvering simulations of totally submerged UVs. For this purpose, the forces and moments obtained from the simulations of

the straight-ahead resistance, drift and rotating arm tests over various submergence depths are implemented in this model. In this regard, as the hydrodynamic axial force acting on a shallowly submerged UV close to the free surface obtained from the straight-ahead resistance tests has a periodic behavior with respect to the axial velocity component, this force component is stored in a one-dimensional tabular form over various submergence depths, and a cubic interpolation is used to express this component in the maneuvering equations. Apart from the axial force generated by the axial velocity component on the shallowly submerged UV, the rest of the hydrodynamic forces and moments obtained from the captive tests are implemented in the maneuvering equations by fitting them to odd/even quadratic polynomial functions in terms of the UV velocity components. Additionally, analytical equations are used to calculate the forces and moments due to the UV accelerations, thrust and rudder, which all are assumed to remain constant with respect to the submergence depth.

During the turning maneuver advance, transfer, tactical diameter and turning diameter all undergo an increase with a decrease in submergence depth. This is due to an increase in the damping characteristics of the UV, which in return decreases the maneuverability with a decrease in submergence depth.

Additionally, in zigzag maneuver, the overshoot angles undergo a reduction with a decrease in submergence depth, which is attributed to the improved course stability as the UV approaches the free surface.

Furthermore, the decrease in the N-moment produced by the lateral velocity and the increase in the N-moment generated by the yaw rate with a decrease in submergence depth lead to a decrease in the UV drift angle during the maneuvers, which consequently causes a decrease in the UV speed loss. Besides, the increase in the N-moment generated by the yaw rate with a decrease in submergence depth gives rise to a reduction in the yaw rate during the SUBOFF maneuvers.

The present work can be extended by performing the dynamic PMM tests, along with the rudder tests and open water propeller tests to evaluate and analyze the free surface effect on the forces and moments resulting from the UV accelerations, rudder and propeller, and consequently on the UV maneuverability. Furthermore, by calculating the external forces and moments in the vertical plane degrees of freedom, the UV maneuverability with the presence of the free surface can also be assessed by performing maneuvering simulations in six degrees of freedom. In this regard, to express the hydrodynamic forces and moments as a function of both the submergence depth and the velocity/acceleration components, they can be stored in a two-dimensional tabular form and a triangle-based cubic interpolation, which has C^2 continuity, can be used for the implementation of the forces and moments in the equations of motion.

Another extension to the present work can be the evaluation of the underly-

ing quasi-steady assumption of the equations of motion. This evaluation can be performed by conducting the unsteady drift and straight-ahead tests over various submergence depths. The analysis of the local and global variables acting on the UV during these tests can be usefully employed for better understanding of the free surface effect on the forces and moments arising from the unsteady and memory effects. Furthermore, these forces and moment generated by the unsteady and memory effects can be included in the equations of motion to evaluate the role they play in the UV maneuverability over various submergence depths.

Eventually, the same methodology used in this thesis can also be employed to evaluate the hydrodynamics and maneuverability of another axisymmetric UV model, such as the REMUS. The main difference between the REMUS and SUB-OFF UVs is the shape of the stern region, which the SUBOFF has a rapidly tapered stern, while the REMUS has a gradually tapered one. It is believed that this comparison can provide a valuable understanding of the influence of the different stern shapes on the hydrodynamics and maneuverability of UVs.

Bibliography

[1] GERTLER, M., HAGEN, G. R. *Standard equations of motion for submarine simulation*. Relatório técnico, DAVID W TAYLOR NAVAL SHIP RESEARCH AND DEVELOPMENT CENTER BETHESDA MD, 1967.

[2] FELDMAN, J. P. *Method of Performing Captive-Model Experiments to predict the Stability and Control Characteristics of Submarines*. Relatório técnico, NAVAL SURFACE WARFARE CENTER CARDEROCK DIV BETHESDA MD HYDROMECHANICS DIRECT ORATE, 1995.

[3] LEWIS, E. V. "Principles of naval architecture second revision, 1988." 1988.

[4] FELDMAN, J. *Dtnsrdc revised standarrd submarine equations of motion*. Relatório técnico, DAVID W TAYLOR NAVAL SHIP RESEARCH AND DEVELOPMENT CENTER BETHESDA MD SHIP PERFORMANCE DEPT, 1979.

[5] SMITH, N., CRANE, J., SUMMEY, D. "SDV simulator hydrodynamic coefficients", *NCSC Rep. TM-231-78, Naval Coastal Systems Center, Panama City, FL, June*, 1978.

[6] POLIS, C., RANMUTHUGALA, D., DUFFY, J., et al. "Enabling the prediction of manoeuvring characteristics of a submarine operating near the free surface". In: *Pacific 2013 International Maritime Conference: The commercial maritime and naval defence showcase for the Asia Pacific*, p. 281. Engineers Australia, 2013.

[7] GRIFFIN, M. J. *Numerical prediction of the maneuvering characteristics of submarines operating near the free surface*. Tese de Doutorado, Massachusetts Institute of Technology, 2002.

[8] SAOUT, O., ANANTHAKRISHNAN, P. "Hydrodynamic and dynamic analysis to determine the directional stability of an underwater vehicle near a free surface", *Applied Ocean Research*, v. 33, n. 2, pp. 158–167, 2011.

[9] FIELD, A. I. *Simulation, modelling, and control of a near-surface underwater vehicle*. Tese de Doutorado, University of British Columbia, 2000.

[10] DAWSON, E. *An investigation into the effects of submergence depth, speed and hull length-to-diameter ratio on the near surface operation of conventional submarines*. Tese de Doutorado, University of Tasmania, 2014.

[11] JAGADEESH, P., MURALI, K. "RANS predictions of free surface effects on axisymmetric underwater body", *Engineering Applications of Computational Fluid Mechanics*, v. 4, n. 2, pp. 301–313, 2010.

[12] MANSOORZADEH, S., JAVANMARD, E. "An investigation of free surface effects on drag and lift coefficients of an autonomous underwater vehicle (AUV) using computational and experimental fluid dynamics methods", *Journal of Fluids and Structures*, v. 51, pp. 161–171, 2014.

[13] NEMATOLLAHI, A., DADVAND, A., DAWOODIAN, M. "An axisymmetric underwater vehicle-free surface interaction: A numerical study", *Ocean Engineering*, v. 96, pp. 205–214, 2015.

[14] SALARI, M., RAVA, A. "Numerical investigation of hydrodynamic flow over an AUV moving in the water-surface vicinity considering the laminar-turbulent transition AUV ", *Journal of Marine Science and Application*, v. 16, n. 3, pp. 298–304, 2017.

[15] BROGLIA, R., DI MASCIO, A., MUSCARI, R., et al. "Numerical study of confined water effects on a self-propelled submarine in steady manoeuvres". In: *The Sixteenth International Offshore and Polar Engineering Conference*. International Society of Offshore and Polar Engineers, 2006.

[16] CARRICA, P., KERKVLIET, M., QUADVLIEG, F., et al. "CFD Simulations and Experiments of a Maneuvering Generic Submarine and Prognosis for Simulation of Near Surface Operation". In: *Proceedings of the 31st Symposium on Naval Hydrodynamics, Monterey, CA, USA*, 2016.

[17] DUBBIOSO, G., BROGLIA, R., ZAGHI, S. "CFD analysis of turning abilities of a submarine model", *Ocean Engineering*, v. 129, pp. 459–479, 2017.

[18] SHARIATI, S. K., MOUSAVIZADEGAN, S. H. "The effect of appendages on the hydrodynamic characteristics of an underwater vehicle near the free surface", *Applied Ocean Research*, v. 67, pp. 31–43, 2017.

[19] MAALI AMIRI, M., ESPERANÇA, P. T., VITOLA, M. A., et al. "How does the free surface affect the hydrodynamics of a shallowly submerged submarine?" *Applied Ocean Research*, v. 76, pp. 34–50, 2018.

[20] NOBLESSE, F., HE, J., ZHU, Y., et al. "Why can ship wakes appear narrower than Kelvins angle?" *European Journal of Mechanics-B/Fluids*, v. 46, pp. 164–171, 2014.

[21] NEWMAN, J. "MARINE HYDRODYNAMICS, 1977, The MIT Press." 1977.

[22] MACKAY, M. *A Review of Sting Support Interference and Some Related Issues for the Marine Dynamic Test Facility (MDTF)*. Relatório técnico, DEFENCE RESEARCH ESTABLISHMENT ATLANTIC DARTMOUTH (NOVA SCOTIA), 1993.

[23] AHN, S. *An experimental study of flow over a 6 to 1 prolate spheroid at incidence*. Tese de Doutorado, Virginia Tech, 1992.

[24] WETZEL, T. G., SIMPSON, R. L., CHESNAKAS, C. J. "Measurement of three-dimensional crossflow separation", *AIAA journal*, v. 36, n. 4, pp. 557–564, 1998.

[25] CHESNAKAS, C., SIMPSON, R. "A detailed investigation of the 3-D separation about a 6: 1 prolate spheroid at angle of attack". In: *34th Aerospace Sciences Meeting and Exhibit*, p. 320, 1997.

[26] HAVELOCK, T. H. "Some cases of wave motion due to a submerged obstacle", *Proc. R. Soc. Lond. A*, v. 93, n. 654, pp. 520–532, 1917.

[27] HAVELOCK, T. H. "The wave resistance of a spheroid", *Proc. R. Soc. Lond. A*, v. 131, n. 817, pp. 275–285, 1931.

[28] HAVELOCK, T. H. "The wave resistance of an ellipsoid", *Proc. R. Soc. Lond. A*, v. 132, n. 820, pp. 480–486, 1931.

[29] WIGLEY, W. "Water forces on submerged bodies in motion", *Transactions of the Institution of Naval Architects*, pp. 268–279, 1953.

[30] DOCTORS, L., BECK, R. "Convergence properties of the Neumann-Kelvin problem for a submerged body", *Journal of Ship Research*, v. 31, n. 4, 1987.

[31] CROOK, T. P. *An initial assessment of free surface effects on submerged bodies*. Tese de Doutorado, Monterey, California. Naval Postgraduate School, 1994.

[32] BELIBASSAKIS, K., GEROSTATHIS, T. P., POLITIS, C., et al. "A novel BEM-isogeometric method with application to the wavemaking resistance problem of bodies at constant speed". In: *Intern. Maritime Association Mediterranean Conference, IMAM*, 2009.

[33] GOURLAY, T., DAWSON, E. "A havelock source panel method for near-surface submarines", *Journal of Marine Science and Application*, v. 14, n. 3, pp. 215–224, 2015.

[34] ARZHANNIKOV, A. V., KOTELNIKOV, I. A. "Excitation of ship waves by a submerged object: New solution to the classical problem", *Physical Review E*, v. 94, n. 2, pp. 023103, 2016.

[35] WILSON-HAFFENDEN, S., RENILSON, M., RANMUTHUGALA, D., et al. "An Investigation into the Wave Making Resistance of a Submarine Travelling Below the Free Surface". In: *International Maritime Conference 2010: Maritime Industry-Challenges, Opportunities and Imperatives, 27-29 January 2010, Sydney, Australia*, p. 495. Engineers Australia, 2010.

[36] SUTULO, S., GUEDES SOARES, C. "Mathematical models for simulation of manoeuvring performance of ships", *Marine Technology and Engineering, G. Soares, C. Garbatov, Y. Fonseca, and AP Teixeira, eds., Taylor & Francis Group, London*, pp. 661–698, 2011.

[37] STARCCM+, V. "9.04. 009 User Guide", *CD-adapco Inc., New York, NY, USA*, 2014.

[38] VERSTEEG, H. K., MALALASEKERA, W. *An introduction to computational fluid dynamics: the finite volume method*. Pearson Education, 2007.

[39] HIRT, C. W., NICHOLS, B. D. "Volume of fluid (VOF) method for the dynamics of free boundaries", *Journal of computational physics*, v. 39, n. 1, pp. 201–225, 1981.

[40] GROVES, N. C., HUANG, T. T., CHANG, M. S. *Geometric Characteristics of DARPA (Defense Advanced Research Projects Agency) SUBOFF Models (DTRC Model Numbers 5470 and 5471)*. Relatório técnico, DAVID TAYLOR RESEARCH CENTER BETHESDA MD SHIP HYDROMECHANICS DEPT, 1989.

[41] ETEBARI, A., ATSAVAPRANEE, P., CARNEAL, J., et al. "Experimental measurements on a SUBOFF model in a turning maneuver". In: *27th symposium on naval hydrodynamics. Seoul, Korea*, 2008.

[42] LIU, H.-L., HUANG, T. T. *Summary of DARPA SUBOFF experimental program data*. Relatório técnico, NAVAL SURFACE WARFARE CENTER CARDEROCK DIV BETHESDA MD HYDROMECHANICS DIRECTORATE, 1998.

[43] RODDY, R. F. *Investigation of the stability and control characteristics of several configurations of the DARPA SUBOFF model (DTRC Model 5470) from captive-model experiments*. Relatório técnico, DAVID TAYLOR RESEARCH CENTER BETHESDA MD SHIP HYDROMECHANICS DEPT, 1990.

[44] HUANG, T., LIU, H. "Measurements of flows over an axisymmetric body with various appendages in a wind tunnel: the DARPA SUBOFF experimental program", 1994.

[45] FOSSEN, T. I. *Guidance and control of ocean vehicles*. John Wiley & Sons Inc, 1994.

[46] FOSSEN, T. I. *Marine control systems: guidance, navigation and control of ships, rigs and underwater vehicles*. Marine Cybernetics, 2002.

[47] SNAME, S. H. "Nomenclature for Treating the Motion of a Submerged Body through a Fluid". In: *American Towing Tank Conference*, 1950.

[48] GAO, T., WANG, Y., PANG, Y., et al. "A time-efficient CFD approach for hydrodynamic coefficient determination and model simplification of submarine", *Ocean Engineering*, v. 154, pp. 16–26, 2018.

[49] MOLLAND, A. F., TURNOCK, S. R., HUDSON, D. A. *Ship resistance and propulsion*. Cambridge university press, 2017.

[50] HUMPHREYS, D., WATKINSON, K. *Prediction of acceleration hydrodynamic coefficients for underwater vehicles from geometric parameters*. Relatório técnico, NAVAL COASTAL SYSTEMS LAB PANAMA CITY FL, 1978.

[51] DE BARROS, E., PASCOAL, A., DE SA, E. "Investigation of a method for predicting AUV derivatives", *Ocean Engineering*, v. 35, n. 16, pp. 1627–1636, 2008.

[52] SEZEN, S., DOGRUL, A., DELEN, C., et al. "Investigation of self-propulsion of DARPA Suboff by RANS method", *Ocean Engineering*, v. 150, pp. 258–271, 2018.

[53] TRIANTAFYLLOU, M. S., HOVER, F. S. *Maneuvering and control of marine vehicles*. Massachusetts of Institute of Technology, 2003.

[54] PHILLIPS, A. B., TURNOCK, S. R., FURLONG, M. "Influence of turbulence closure models on the vortical flow field around a submarine body undergoing steady drift", *Journal of marine science and technology*, v. 15, n. 3, pp. 201–217, 2010.

[55] KIM, S.-E., RHEE, S., COKLJAT, D. "Application of modern turbulence models to vortical flow around a prolate spheroid". In: *41st Aerospace Sciences Meeting and Exhibit*, p. 429, 2003.

[56] ZHANG, J., MAXWELL, J. A., GERBER, A. G., et al. "Simulation of the flow over axisymmetric submarine hulls in steady turning", *Ocean engineering*, v. 57, pp. 180–196, 2013.

[57] FERZIGER, J. H., PERIC, M. *Computational methods for fluid dynamics*. Springer Science & Business Media, 2012.

[58] HOLLOWAY, A., JEANS, T., WATT, G. "Flow separation from submarine shaped bodies of revolution in steady turning", *Ocean Engineering*, v. 108, pp. 426–438, 2015.

[59] SPEZIALE, C. G., SARKAR, S., GATSKI, T. B. "Modelling the pressure–strain correlation of turbulence: an invariant dynamical systems approach", *Journal of fluid mechanics*, v. 227, pp. 245–272, 1991.

[60] EÇA, L., SARAIVA, G., VAZ, G., et al. "The Pros and Cons of Wall Functions". In: *ASME 2015 34th International Conference on Ocean, Offshore and Arctic Engineering*, pp. V002T08A012–V002T08A012. American Society of Mechanical Engineers, 2015.

[61] FALTINSEN, O. *Sea loads on ships and offshore structures*, v. 1. Cambridge university press, 1993.

[62] BERTRAM, V. *Practical ship hydrodynamics*. Elsevier, 2011.

[63] MUZAFERIJA, S. "A two-fluid Navier-Stokes solver to simulate water entry". In: *Proceedings of 22nd symposium on naval architecture, 1999*, pp. 638–651. National Academy Press, 1999.

[64] LEONARD, B. "The ULTIMATE conservative difference scheme applied to unsteady one-dimensional advection", *Computer methods in applied mechanics and engineering*, v. 88, n. 1, pp. 17–74, 1991.

[65] SPENCE, S. *Numerical Investigation of Free Surface Flows*. Tese de Mestrado, Institutt for marin teknikk, 2014.

[66] RHIE, C., CHOW, W. L. "Numerical study of the turbulent flow past an airfoil with trailing edge separation", *AIAA journal*, v. 21, n. 11, pp. 1525–1532, 1983.

[67] PERIĆ, R., ABDEL-MAKSOUD, M. "Reliable damping of free-surface waves in numerical simulations", *Ship Technology Research*, v. 63, n. 1, pp. 1–13, 2016.

[68] TOXOPEUS, S., ATSAVAPRANEE, P., WOLF, E., et al. "Collaborative CFD exercise for a submarine in a steady turn". In: *ASME 2012 31st International Conference on Ocean, Offshore and Arctic Engineering*, pp. 761–772. American Society of Mechanical Engineers, 2012.

[69] RICHARDS, S. A. "Completed Richardson extrapolation in space and time", *Communications in numerical methods in engineering*, v. 13, n. 7, pp. 573–582, 1997.

[70] STERN, F., WILSON, R., SHAO, J. "Quantitative V&V of CFD simulations and certification of CFD codes", *International journal for numerical methods in fluids*, v. 50, n. 11, pp. 1335–1355, 2006.

[71] RICHARDSON, L. F. "IX. The approximate arithmetical solution by finite differences of physical problems involving differential equations, with an application to the stresses in a masonry dam", *Phil. Trans. R. Soc. Lond. A*, v. 210, n. 459-470, pp. 307–357, 1911.

[72] MCHALE, M., FRIEDMAN, J. "Standard for Verification and Validation in Computational Fluid Dynamics and Heat Transfer", *The American Society of Mechanical Engineers, ASME V&V*, pp. 20–2009, 2009.

[73] EÇA, L., HOEKSTRA, M. "Evaluation of numerical error estimation based on grid refinement studies with the method of the manufactured solutions", *Computers & Fluids*, v. 38, n. 8, pp. 1580–1591, 2009.

[74] HUMPHREYS, D., WATKINSON, K. "The impact of open-loop vehicle stability on closed-loop control system performance: an analysis of four AUV concepts". In: *OCEANS'92. Mastering the Oceans Through Technology. Proceedings.*, v. 2, pp. 533–538. IEEE, 1992.

[75] WHITE, F. M. "Viscous fluid flow 3rd ed". 2006.

Appendix A

Procedure of grid generation

The most important aspect of the process of simulation configuration is undoubtedly the mesh generation process, which requires remarkable attention in order to obtain acceptable results. Generally, in areas of large gradients of variables, a mesh should have a large number of cells. As mentioned in section 2.6, to capture properly the wave system generated by the UV together with the pressure drop in the wake region and leeward side of the SUBOFF at drift, appropriate local mesh refinements are utilized. Herein, the general mesh setups used in captive tests are presented. These setups include the mesh refinements used to capture the turbulent boundary layer, the pressure drop in both the wake region and the leeward side of the UV at drift and the UV-generated wave system.

A.1   Mesh setups used to capture the boundary layer

As mentioned in section 2.6, for the region near the UV the prism layer mesh is employed to capture the fluid flow characteristics in the boundary layer. The prism layer mesh is comprised as a sequence of layers whose thicknesses increase based on a geometric progression. The expansion factor is set 1.1. To specify the boundary layer thickness δ by assuming a flat plate, the following equation is used, WHITE [75]:

$$\frac{\delta}{L} = 1.5 \times \frac{0.16}{Re_L^{\frac{1}{7}}} \tag{A.1}$$

where Re_L is the Reynolds number defined based on the UV overall length. Additionally, the first layer thickness is estimated in such a manner that gives a Y^+ value in the range from 30 to 100. Thus, having calculated both the first layer thickness and the boundary layer thickness, one can determine the number of prism layers by

using the formula to calculate the sum of the n terms (in this case n signifies the number of prism layers) of a geometric series.

A.2 Mesh setups in domain boundaries, wake region and leeward side of the UV at drift

To capture the pressure drop in the wake region, a finer mesh is generated in a block form region expanded from the fore of the UV to nearly one body-length downstream. In this block form region a minimum cell size equal to $4\% \times$ BS is generated. This region is also used to capture the pressure drop in the leeward side of the UV at drift. The utilization of this block form region can be clearly identified in Figures 2.22, 2.23, 2.24 and 2.25. Additionally, according to the initial simulations conducted by the present author, it is also decided to use even a finer mesh in a region close to the UV in the form of the body itself but with dimensions of 1.2 times of that of the original one. In this region, a minimum cell size equal to $0.833\% \times$ BS, which is the same size used for cells on the hull surface, is employed. Figure A.1 shows these regions along with their dimensions used in straight-ahead resistance and drift tests. Moreover, the minimum cell size on the boundaries surrounding the UV is considered as $100 \times$ BS.
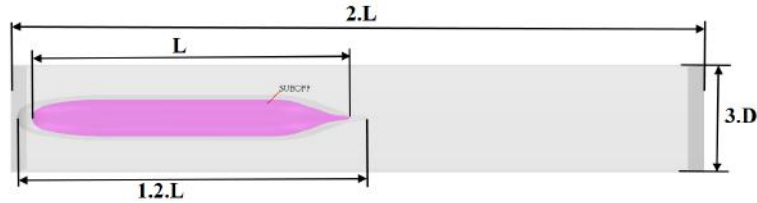
(a) The regions around the UV where the mesh is refined in straight-ahead tests

(b) The regions around the UV where the mesh is refined in drift tests for $\beta = 18.11°$

Figure A.1: Block form region and the region in the form of the UV itself used to refine the grid around the UV

In the tests with the presence of the free surface, to simulate correctly the free surface-UV interaction, the block form region is extended upward to cover the free surface. The upward extension of the block form region can be clearly identified in Figure A.2, which shows the grid generated at $x_0 s z_0$ plane in straight ahead resistance tests for $F_n = 0.512$ and $h = 3.3D$.
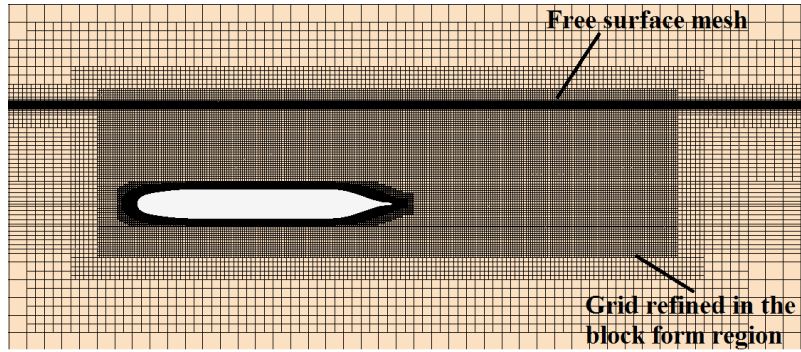
Figure A.2: The grid generated in x_0sz_0 plane in straight ahead resistance tests for $F_n = 0.512$ and $h = 3.3D$

A.3   Mesh setups in the free surface region

An important point in the tests with the presence of the free surface is to generate a mesh of good quality to capture the free surface deformations resulting from the free surface-UV interaction. In this regard, as mentioned in section 2.6, we follow the recommendations provided by SPENCE [65]. Accordingly, the refinement normal to the undisturbed free surface, which is applied in the entire computational domain, is made by discretizing the free surface in this direction using nearly 30 to 50 cells per wave height. The reason to use a constant refinement normal to the free surface over the entire domain is to avoid any adverse effect resulting from a jump in the refinement normal to the free surface. Additionally, as can be observed in Figures 2.22, 2.23, 2.24 and 2.25, to guarantee a smooth transition between the fine region on the free surface and the coarse far field region in the normal direction to the free surface, the mesh resolution is reduced to one-eighth inside a block form region surrounding the free surface, which stretches one wave height to the top of the deformed free surface and goes all the way down to the bottom of the UV and at the same time extends throughout the entire domain in the direction parallel to the free surface.

Moreover, the refinement parallel to the undisturbed free surface is applied by discretizing the free surface in this direction using nearly 100 to 160 cells per wavelength inside the block form region shown in Figure A.3, which is located right above the UV. On the other hand, to decrease the number of cells in the computational domain the resolution of the grid in the direction parallel to the undisturbed free surface is reduced to half for the rest of the free surface region outside this block. Figure A.4 shows the grid generated in xoy plane on the free surface in straight-ahead tests for $F_n = 0.462$ and $h = 1.1D$. In this case again, to guarantee a smooth transition between the fine region on the free surface to the coarse far field region in the normal direction to the free surface, the mesh resolution is reduced to one-eighth

inside the block form region mentioned earlier, which stretches one wave height to the top of the deformed free surface and goes all the way down to the bottom of the UV and at the same time extends throughout the entire domain in the direction parallel to the free surface.
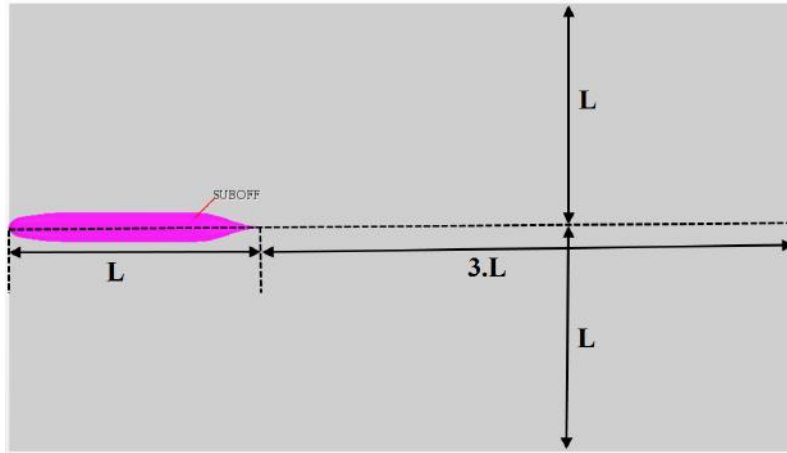
(a) Top view of the block form region on the free surface, where the grid is refined for $F_n = 0.462$ and $h = 1.1D$

(b) Side view of the block form region on the free surface, where the grid is refined for $F_n = 0.462$ and $h = 1.1D$

Figure A.3: Block form region used to refine the grid in the direction parallel to the undisturbed free surface
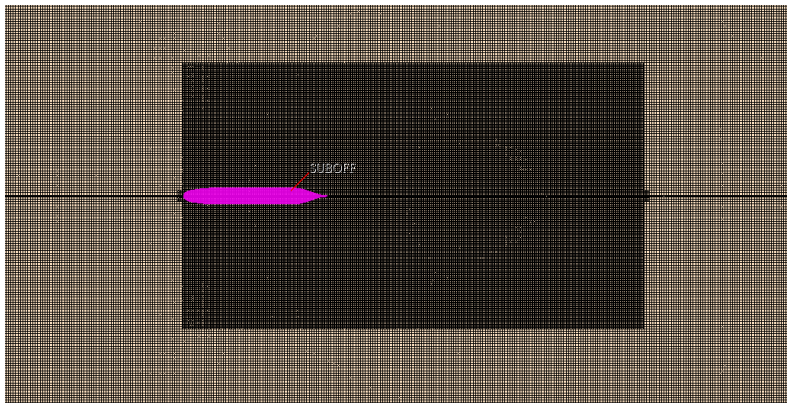

Figure A.4: The grid generated in xoy plane on the free surface in straight-ahead resistance tests for $F_n = 0.462$ and $h = 1.1D$

To determine the characteristics of the wave system, including the wavelength and wave period, Equation 2.21 is used for $\Theta = 0$. Thus, to approach the unknown free surface pattern, the transverse wavelength is used to determine the basic wave characteristics.

Appendix B

Turbulence anisotropy

As mentioned earlier, in the eddy viscosity turbulence models the Reynolds stresses are considered aligned with the strain rate of the flow, CHESNAKAS e SIMPSON [25]. To evaluate the applicability of the eddy viscosity models to the present simulations, the quantity $|\gamma_g - \gamma_\tau|$ (Equations 2.66 and 2.66) is plotted for the SUBOFF in straight-ahead resistance tests for $F_n = 0.462$ and $h = 1.1D$ at two normalized axial locations $\frac{x_0}{L} = -0.038, -0.338$, in the boundary layer region (Figure B.1).

It can be inferred from Figure B.1 that the turbulent shear stress angle (γ_τ) and the flow gradient angle (γ_g) cannot be assumed aligned over the whole region of the boundary layer. On the contrary, they are remarkably misaligned over a considerable portion of this region, which implies that using the eddy viscosity models can lead to erroneous results.
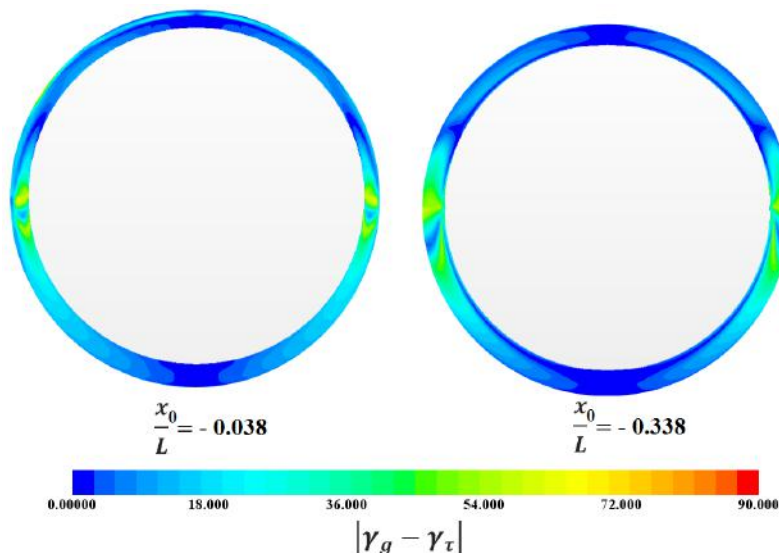

Figure B.1: $|\gamma_g - \gamma_\tau|$ over the SUBOFF at two normalized axial locations $\frac{x_0}{L} = -0.038, -0.338$ from the nose and $F_n = 0.462$ and $h = 1.1D$. The figure clearly shows that the turbulent shear stress angle (γ_τ) and the flow gradient angle (γ_g) are remarkably misaligned over a considerable portion of the boundary layer region, which implies that using the eddy viscosity models may lead to erroneous results.

Appendix C

Turbulent boundary conditions

Herein, the boundary conditions for Reynolds stress terms (R) that are employed in the simulations of the current study are presented.

C.0.1 Wall boundary

The gradients of Reynolds stress terms normal to the wall is considered zero as follows:

$$\frac{\partial R}{\partial n} = 0 \tag{C.1}$$

C.0.2 Velocity inlet

In this boundary, the Reynolds stress terms along with the turbulent dissipation rate are derived from the specified turbulence intensity (TI), which is defined as the ratio of the root-mean-square of the velocity fluctuations to the mean velocity, and turbulent viscosity ratio (μ_t/μ) using the following equations:

$$R = (TI|\overrightarrow{\mathbf{V}}|)^2 \mathbf{I} \tag{C.2}$$

$$\varepsilon = \frac{C_\mu \left[\frac{1}{2}tr(R)\right]^2}{(\mu_t/\mu)\mu} \tag{C.3}$$

where $|\overrightarrow{\mathbf{V}}|$ is the local velocity magnitude and $\mathbf{I}$ is the identity matrix. In this study, the default values of $TI = 0.01$ and $\mu_t/\mu = 10$ are used.

Appendix D

Accepted/Submitted publications

Accepted Publications

1. Amiri M.M., Esperança P.T., Vitola M.A., Sphaier S.H., How does the free surface affect the hydrodynamics of a shallowly submerged submarine?, Applied Ocean Research, 2018 Jul 31;76:34-50.

2. Amiri M.M., Vitola M.A., Sphaier S.H., Esperança P.T., RANS feasibility study of using roughness to mimic transition strip effect on the crossflow separation over a 6:1 prolate-spheroid, Journal of Hydrodynamics, 2018 Oct.

Submitted Publications

1. Amiri M.M., Sphaier S.H., Vitola M.A., Esperança P.T., Investigation into the wave system of a generic submarine moving along a straight path beneath the free surface, European Journal of Mechanics - B/Fluids, 2018

2. Amiri M.M., Sphaier S.H., Vitola M.A., Esperança P.T., URANS investigation of the interaction between the free surface and a shallowly submerged underwater vehicle at steady drift, Applied Ocean Research, 2018

How does the free surface affect the hydrodynamics of a shallowly submerged submarine?

Mojtaba Maali Amiri, Paulo T. Esperança, Marcelo A. Vitola, Sergio H. Sphaier

Abstract

It has long been recognized that a shallowly submerged submarine traveling beneath the free surface experiences a larger resistance force in conjunction with a lift force and a pitch moment, which all vary periodically with respect to Froude number. As is well known, the periodic behavior of the forces and moment mainly has to do with the interference effects between the dominant wave systems inside the submarine wake, which predominantly originate from the bow, stern and shoulders. In naval architecture, the principal type of interference is typically considered between the bow and stern waves, where the geometry undergoes abrupt changes. However, as the aft shoulder of a shallowly submerged submarine operates in a closer proximity to the free surface compared to the stern, it is surmised that interference between the bow and aft shoulder waves may have a more significant effect on the behavior of the forces and moments. Accordingly, the main purpose of the present study is to investigate whether the interaction between the bow and aft shoulder waves or the interaction between the bow and stern waves has a more dominant effect on the hydrodynamic behavior of a shallowly submerged submarine. In this regard, the straight-ahead simulations of a generic submarine with constant forward velocities are performed in commercial code STARCCM+ using URANS equations with a Reynolds stress turbulence model at submergence depths and Froude numbers ranging from $h = 1.1D$ to $h = \infty$ (D : submarine diameter) and from $Fn = 0.205$ to $Fn = 0.512$, respectively. The numerical model is partially validated against the existing experimental resistance force data. The analysis of the obtained results demonstrates that in case of the shallowly submerged submarines, the interaction between the bow and aft shoulder waves has a dominant effect on the behavior of the resistance force, lift force and pitch moment.

RANS feasibility study of using roughness to mimic transition strip effect on the crossflow separation over a 6:1 prolate-spheroid

Mojtaba Maali Amiri, Marcelo A. Vitola, Sergio H. Sphaier, Paulo T. Esperança

Abstract

An axisymmetric body at incidence experiences the three-dimensional crossflow separation. This separation is attributed to the adverse circumferential pressure gradient. However, the separation pattern is also dependent upon the structure of the boundary layer. In this regard, utilization of transition strip devices in experiments on axisymmetric bodies may modify this structure, and consequently the crossflow separation pattern. The main objective of the present research is to mimic numerically the transition strip effect on the crossflow separation over a 6:1 prolate-spheroid up to $\alpha = 30°$ incidence and $Re_L = 4.2 \times 10^6$. However, to avoid direct modeling of the strip, which would increase the computational cost, an attempt was made to add roughness over the body surface. To estimate the roughness that simulates closely the transition strip effect, three different roughness values were considered. The numerical model is based on RANS and a Reynolds stress turbulence model implemented in STARCCM+. The simulations have been evaluated based on the local and global variables and validated against the available experimental data. The results demonstrate the effectiveness of using a proper roughness value to mimic the transition strip effect. They also show the importance of modeling the transition strip effect, which is normally not considered, to capture the crossflow separation pattern.

Investigation into the wave system of a generic submarine moving along a straight path beneath the free surface

Mojtaba Maali Amiri, Sergio H. Sphaier, Marcelo A. Vitola, Paulo T. Esperança

Abstract

In a recent paper published by the present authors, it is shown that, in case of the submarines traveling close to the free surface, the interaction between the bow and aft shoulder waves has a more dominant effect on the hydrodynamics of the submarines compared to the interaction between the bow and stern waves, which is usually considered in naval architecture. This result is obtained through a detailed assessment of the pressure distribution along a generic submarine together with a detailed evaluation of the behavior of the global variables acting on the body over various submergence depths and Froude numbers. Accordingly, herein, a detailed investigation into the characteristics of the wave system generated by the same submarine traveling along a straight path close to the free surface is performed to figure out the role of the interaction between the bow and aft shoulder waves in the submarine-generated wave system. Accordingly, the numerical simulations are performed by using unsteady Reynolds-averaged Navier-Stokes equations with a Reynolds stress turbulence model implemented in commercial code STARCCM+ over submergence depths and body length Froude numbers ranging from $h = 1.1 \times D$ to $h = 3.3 \times D$ (D : submarine diameter) and from $F_n = 0.205$ to $F_n = 0.512$, respectively. The validation is performed using the existing experimental resistance force data. In this study, the analysis of the obtained results including the maximum wave height, wake angle and the centerline free surface profiles at hump and hollow Froude numbers shows that the interaction between the bow and aft shoulder waves indeed has a dominant effect on the submarine-generated wave system.

URANS investigation of the interaction between the free surface and a shallowly submerged underwater vehicle at steady drift

Mojtaba Maali Amiri, Sergio H. Sphaier, Marcelo A. Vitola, Paulo T. Esperança

Abstract

An axisymmetric underwater vehicle (UV) at a steady drift angle experiences the complex three-dimensional crossflow separation. This separation arises from the unfavorable circumferential pressure gradient developed from the windward side toward the leeward side. As is well known, the separated flow in the leeward side gives rise to the formation of a pair of vortices, which affects considerably the forces and moments acting on the UV. In this regard, the main purpose of the present study is to evaluate the role of the leeward vortical flow structure in the hydrodynamic behavior of a shallowly submerged UV at a moderate drift angle traveling beneath the free surface. Accordingly, the static drift tests are performed on the SUBOFF UV model using URANS equations coupled with a Reynolds stress turbulence model. The simulations are carried out in the commercial code STARCCM+ at a constant advance velocity based on Froude number equal to $F_n = 0.512$ over submergence depths and drift angles ranging from $h = 1.1D$ to $h = \infty$ and from $\beta = 0$ to $\beta = 18.11°$, respectively. The validation of the numerical model is partially conducted by using the existing experimental data of the forces and moment acting on the totally submerged bare hull model. Significant interaction between the low-pressure region created by the leeward vortical flow structure and the free surface is observed. As a result of this interaction, the leeward vortical flow structure appears to be largely responsible for the behavior of the forces and moments exerted on a shallowly submerged UV at steady drift.